Time-resolved rheology on complex fluids

Dissertation zur Erlangung des Doktorgrades

an der Fakultät für Mathematik, Informatik und
Naturwissenschaften
Fachbereich Physik der Universität Hamburg

vorgelegt von

Verena I. Markmann

April 23, 2021

Supervisor: Prof. Dr. G. Grübel
Prof. Dr. A. Pearson

Vorsitzender Fach-Promotionsausschusses PHYSIK: Prof. Dr. Günter Hans Walter Sigl

Leiter des Fachbereichs PHYSIK: Prof. Dr. Wolfgang Hansen

Dekan der Fakultät MIN: Prof. Dr. Heinrich Graener

Abstract

The aim of this work was to explore the potential of a combined rheology and X-ray scattering approach on complex fluids. Shear rates between $0.9 \cdot 10^5\,\mathrm{s}^{-1}$ and $5.6 \cdot 10^5\,\mathrm{s}^{-1}$, which are magnitudes higher than found in classical rheometry studies, were applied to a suspension of colloidal silica nanoparticles by a microfluidic jet device. Characteristic structure formation was studied along and across the flow direction with small angle X-ray scattering. The anisotropy of the diffraction patterns was evaluated by X-ray cross-correlation analysis. Furthermore, the decay of the shear-induced ordering after the cessation of the shear was quantified.
With particle sizes of $r = 15\,\mathrm{nm}$-$76.5\,\mathrm{nm}$ Péclet numbers of 1 to 1162 were investigated, a dynamic regime where diffusive motion is dominated by shear-dominated dynamics. For different Rayleigh nozzle sizes and geometries characteristic decay times between $25\,\mu\mathrm{s}$ and $495\,\mu\mathrm{s}$ were measured and correlated with the Péclet number of the system.
The influence of electro-static forces was investigated by adding salt to the colloidal suspension, which reduced the overall ordering. The impact of the particle charge on the effective screening of the particles and the ionic strength of the suspension were explored.
By modeling string-like particle distributions and comparison with the corresponding diffraction patterns and the measured shape asymmetry, it was possible to determine a variation of the volume fraction over the azimuthal angle of $\approx \pm 5\%$ for the maximum ordered state in the jet. This interpretation was in good agreement with rescaled mean spherical approximation modeling.

Zusammenfassung

Ziel dieser Studie war die Untersuchung komplexer Flüssigkeiten mit kombinierten Rheologie- und Röntgen-Streuexperimenten. Anders als mit klassischen Rheometern wurden hier Scherraten von $0.9 \cdot 10^5\,\mathrm{s}^{-1}$ bis $5.6 \cdot 10^5\,\mathrm{s}^{-1}$ mit Hilfe von mikrofluidischen Jetsystemen auf die Proben ausgeübt. An verschiedenen kolloidalen Silicapartikeln in Wasser wurde eine richtungsabhängige Strukturbildung entlang der Flussrichtung und quer über das Jetprofil hinweg mit Röntgen-Kleinwinkelstreuung beobachtet. Analysiert wurden die gemessenen anisotropischen Streubilder anschließend mit Hilfe von Kreuzkorrelationen. Mit dieser Technik wurde das Abklingen der scherinduzierten Partikelanordung im Jet quantifiziert.

Ein Zusammenhang konnte zwischen dem Verschwinden von Ordnung mit wachsendem Abstand zur Düse und der Péclet Zahl des Systems festgestellt werden. Mit Partikelgrößen $r =$ 15 nm-76.5 nm wurden Péclet Zahlen von 1 bis 1162 untersucht, was einem Bereich entspricht, in dem diffusiver Transport von scherinduzierter Dynamik dominiert wird. Rayleigh Düsen unterschiedlicher Größen und Geometrien zeigten charakteristische Abklingzeiten zwischen $25\,\mu$s und $495\,\mu$s.

Der Einfluss elektrostatischer Kräfte auf das System wurden unter der Zugabe von Salz zu den kolloidalen Suspensionen studiert. Im Allgemeinen wurde eine Verringerung des Ausmaßes an Ordnung im System beobachtet, wobei die Auswirkung der Ladung pro Partikel auf die effektive Abschirmung sowie unterschiedliche Ionenstärken der Lösungen untersucht wurden.

Am Ende wurden schnurartige Partikelanordungen mit ihren dazugehörigen Streubildern modeliert, welche mit den experimentellen Daten vergleichbar waren. Dadurch wurden Variationen des Volumenanteils über den Azimuthalwinkel der Streubilder um $\approx \pm 5\%$ für Positionen maximaler Ordung im Jet festgestellt. Bestätigt werden konnte dieses Ergebnis mit Resultaten die mittels der Rescaled-Mean-Spherical Approximation (RMSA) erzielt wurden.

Index of abbreviations

SAXS	small-angle X-ray scattering
XCCA	X-ray cross-correlation analysis
DLVO theory	Derjaguin, Landau, Verwey and Overbeek (1940) theory
RMSA	rescaled mean spherical approximation
q	wave vector transfer
I(q)	scattered intensity
F(q)	form factor
S(q)	structure factor
ε(d,h)	intensity asymmetry
var(q_0)(d,h)	shape asymmetry
$\xi_\varepsilon(t)$	decay of the intensity asymmetry
τ_ε	characteristic decay time of the intensity asymmetry
φ	azimuthal angle
$\dot{\gamma}$	shear rate
τ	shear stress
μ	viscosity
D_0	diffusion coefficient
Pe	Péclet number
c	volume fraction
d	axis perpendicular to the jet
h	axis along the jet
v_{jet}	jet velocity
d_{jet}	jet diameter

Contents

Chapter 1

Introduction

A combination of rheological studies with time-resolved light scattering techniques provides the opportunity to study shear-induced distortion of microstructures in liquids. Complex fluids such as colloidal suspensions are of peculiar interest, as foams, gels or dispersions became part of the every day life. This thesis focuses on the microscopic particles ordering in liquids under strong shear forces, which were deployed by liquid micro-jets, and the effects of shear on colloidal system after the cessation of the shear forces.

The control of complex fluid sample systems by microfluidic jet devices has become of increasing scientific and technological interest in the last decades, especially at Free Electron Laser facilities (FEL)[1–5]. The applications include the production of supercooled liquids by evaporative cooling of μm-sized droplets[6–8] and sample delivery schemes for materials sensitive to radiation damage[9–11]. Free flowing jets as sample environment have the advantage of a self-refreshing sample and lack of solid boundaries, but small sample volumes often dictate low flow rates and therefore μm-thin jets.

The shear rates observed in microfluidic environments are in the regime of $\dot{\gamma} \approx 10^5\,\mathrm{s}^{-1}$ and thus several orders of magnitude higher than in conventional rheometer geometries[12,13]. However, studies of the influence of shear within the nozzles or the gas environment of the jet are rare[14]. Higher shear typically leads to more pronounced structure development[15,16] and therefore has to be taken into consideration for time-dependent and complex samples such as biological molecules that are measured in the flow of a liquid jet. Also in spectroscopy the onset of structure formation may influence the measured signal[17]. In ultra-thin liquid sheets or flat-jets infrared and soft X-ray spectroscopy becomes possible despite the strong absorption in this regime[18], but the small number of molecules in thin jets are especially susceptible to shear-induced alterations in the concentration distribution.

In many liquid jet applications the influence of shear on the studied particles or molecules is typically disregarded. In order to show the effects of shear, different designs of Rayleigh jet devices[19] were studied in this work. Unlike Gas Dynamic Virtual Nozzles[20,21], where a gas flow envelops a liquid jet and compresses it, in Rayleigh jets the shear is due to the flow profile inside the nozzle. Rayleigh jets are formed upon the rapid exit of a fluid from a nozzle, followed by the subsequent break-up into droplets. In order to obtain a more detailed understanding of time- and space-resolved rheology of colloidal dispersions in a Rayleigh jet, small angle X-ray scattering (SAXS) was applied. A μm-sized beam scanned along a several micrometer thick liquid jet and shear-induced ordering of colloidal particles into co-flowing strings could be observed. In general, the formation of co-flowing layers and hydroclusters is due to imbalances between hydrodynamic and thermodynamic forces, which are associated with shear thinning and thickening processes[22–24]. However, the influence of jet geometries and the magnitude of shear rates on structure formation remains an open question.

This thesis is organized as follows: A general overview of rheometers, complex fluids and flow dynamics is given in chapter 2. Chapter 3 introduces X-ray scattering techniques and analysis tools such as cross-correlation techniques. In chapter 4 the setup and sample systems used for two different experimental campaigns are described and experimental results are presented in chapter 5. Influences on the electro-static potential of the colloidal system are discussed in chapter 6. Chapter 7 contains a simulation approach for string-like particle arrangements in a jet and all conclusions and an outlook are summarized in chapter 8.

Chapter 2

Rheology in jetting systems

Rheology, the greek translation for the ’science of flow’, describes the deformation of liquid and solid materials. First significant studies extending beyond irrigation and other hydrostatic systems were performed by Robert Hooke and Isaac Newton in the 17th century.

Hooke observed the linear relationship between applied force and the corresponding deformation for elastic materials[25]. The proportionality constant between those two properties is a material specific parameter known as viscosity. In accordance with Hooke’s work, Newton’s three laws of motion allow for mathematical descriptions of the relation between applied stress and material deformation[26]. The term rheology[27] appeared over 200 years later, when the chemist Eugene Bingham and the engineer Markus Reiner started an interdisciplinary cooperation to study different types of deformation and flow mechanics in 1920.

Today rheology has become a standard technique in soft matter physics. Rheometry studies are employed for a wide range of industrial applications, e.g. jet printing[28–30], drug delivery and food processing[31,32] or engineered materials[33–35].

2.1 Rheometer advancements

A requirement for the deformation of materials is the existence of stress, which can have mechanical or thermal causes. Pressure applied perpendicular to the cross-section of the material stretches or compresses the material. If the stress is applied parallel to the cross-section, the material is sheared. In Newton’s first experiments (Fig. 2.1) a fluid was trapped between two plates, where the upper plate is moveable. Shear stress τ is then defined as the ratio between applied tangential force F and the area of the cross-section A between material and force. With a constant viscosity μ, in other words a temperature and stress independent resistance against deformation, the velocity profile is linear between the plates and one obtains

$$\tau = \frac{F}{A} = \mu \cdot \frac{du}{dy} = \mu \cdot \dot{\gamma}. \tag{2.1}$$

Equation 2.1 yields $[\mu] = \frac{\text{kg}}{\text{m}\cdot\text{s}}$ as unit for viscosity[*]. More frequently used is $\text{mPa}\cdot\text{s}$, which sets the viscosity of water (at room temperature) to $1\,\text{mPa}\cdot\text{s}$, making it easy to compare to for example ethanol ($\mu = 1.19\,\text{mPa}\cdot\text{s}$), engine oil ($\mu \approx 100\,\text{mPa}\cdot\text{s}$) or honey ($\mu \approx 10^4\,\text{mPa}\cdot\text{s}$). The derivative of the velocity perpendicular to the direction of movement from the plate is called shear rate with[36] $[\dot{\gamma}] = \text{s}^{-1}$. Multiple concepts have been developed since Newton's experiment to measure shear force and viscosity in order to understand inner friction and the cohesive attraction of molecules that influence deformation and flow behavior. In general, there are three viscometer types to be distinguished: capillary, extensional and rotational viscometers. Usually these devices are equipped for temperature control and further flow conditioning, thus they are called rheometers.

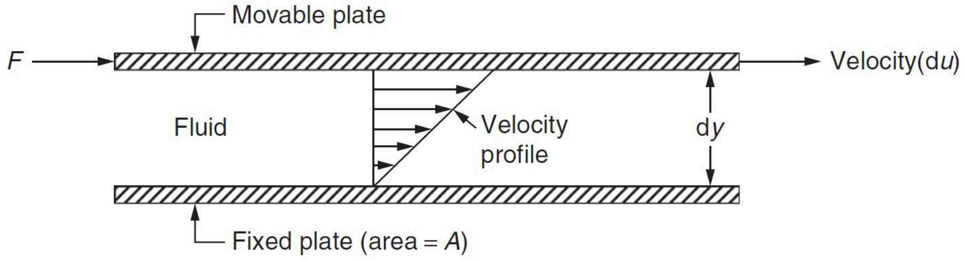

Figure 2.1: Two parallel plates with a fluid between them[37] illustrate the definition of shear stress τ and shear rate $\dot{\gamma}$.

2.1.1 Capillary rheometer

In a capillary rheometer pressure is applied on a fluid in a reservoir. On the bottom of the reservoir a capillary of length l and radius r is connected. For fluids of constant viscosity μ and laminar flows (no turbulences), also called Newtonian fluids, the pressure drop ΔP in capillaries is describes by the Hagen-Poiseuille equation:

$$\Delta P = \frac{8\mu l Q}{\pi r^4}. \tag{2.2}$$

By measuring the flow rate Q corresponding to the applied pressure difference ΔP, μ of highly viscous fluids can be determined. However, as shear stress is a derivative of the fluids velocity, the velocity profile in the capillary does not develop spontaneously. Therefore, the capillary has to be sufficiently long and narrow. To reach the equilibrium condition for a laminar flow, the applied pressure has to be balanced with the shear forces on the inner walls of the capillary[38]:

$$\frac{dP}{dx} \cdot \Delta x \pi R^2 = 2\pi\tau R \Delta x, \tag{2.3}$$

with $0 \leq R \leq r$ and x the axis of the capillary. The shear stress profile as shown in Fig. 2.2 is then given by

---

[*] The term 'viscous' was derived from the slow flowing juice of mistletoe berries (lat. viscum).

$$\tau = \frac{R}{2}\frac{dP}{dx}. \tag{2.4}$$

The velocity profile is calculated by integration of the differential equation

$$\mu \frac{du}{dy} = \frac{R}{2}\frac{dP}{dx}. \tag{2.5}$$

Under the condition of $u = 0$ at $r = R$ the integration constant can be determined and the solution for the velocity profile[39] is parabolic:

$$u(R) = \frac{1}{4\mu}\frac{dP}{dx} r^2 \left[1 - \left(\frac{R}{r}\right)^2\right]. \tag{2.6}$$

As a consequence, the shear rate $\dot{\gamma}$ is given by

$$\dot{\gamma} = \frac{\Delta P r}{2\mu l} = \frac{4Q}{\pi r^3}. \tag{2.7}$$

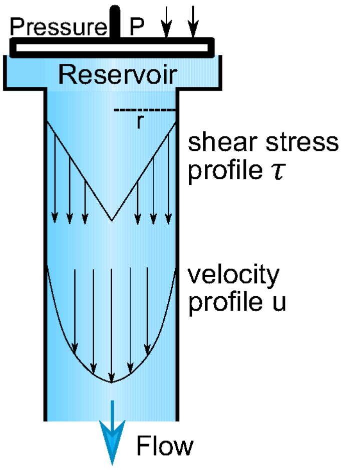

Figure 2.2: Velocity profile u and shear profile τ in a capillary.

2.1.2 Extensional and rotational rheometers

If a fluid has a very high viscosity, the pressure needed to force the fluid through a capillary increases proportionally (equation 2.2). As the application of very high pressures becomes technically unfeasible, different methods of flow characterization have been developed over the last decades. Long-chained polymers such as polyethylene or even solids like rubber or metals can be investigated by elongation in extensional rheometers.

First experiments[40] in the 1960s used a thin film of the test sample floating on a liquid surface. At opposite ends two rotary clamps stretched the test sample. One of the later enhancements for semiviscous to viscous liquids include filament stretching rheometers[41,42], where shear effects on the floating liquid/sample surface are avoided. Here a fluid is placed between two parallel plates. By measuring the tensile force F_t that is needed to pull the two plates apart, as well as the minimum filament radius R_f of the fluid between the plates, a stretching viscosity μ_s can be determined as[43,44]

$$\mu_s = \frac{F_t}{\pi R_f^2 \dot{\varepsilon}_0} - \frac{\sigma}{R_f \dot{\varepsilon}_0}. \tag{2.8}$$

The second term reflects the contribution of surface tension σ. The velocity gradient throughout the filament is a constant equalling the stretching rate $\dot{\varepsilon}_0$, which denotes an equal distribution of the stress in the fluid filament. For Newtonian fluids the ratio between stretching viscosity μ_s and shear viscosity μ, generally known as Trouton number[44], becomes $\mu_s/\mu = 3$. [†].

A third option for flow mechanic measurements are rotational rheometers. As shown in Fig. 2.3 a typical setup consists of two molds with the sample in between. One of the molds rotates at a given velocity and thereby applies a torque to the sample. Viscosities are determined by controlling sample volume and rotation velocity. Shear rates in a very wide range from $\dot{\gamma} \approx 10^{-4}\,\mathrm{s}^{-1}$ (sedimentation) to $\dot{\gamma} \approx 10^{3}\,\mathrm{s}^{-1}$ can be reached with different molds.

Low viscosity liquids require larger surface area and smaller gap size between molds than highly viscous fluids in order to apply shear forces and avoid turbulences. Most common are plate-plate, plate-cone and couette (cup-bob) geometries. One advantage of the plate-cone over the plate-plate geometry is the homogenous shear velocity throughout the sample, while the couette geometry applies shear perpendicular to gravitation and is therefore more suitable for sedimenting samples. Additionally to steady one-directional rotation sinusoidal oscillatory deformation of the sample can also be performed in order to obtain the stored energy of the system as well as energy expended for heat generation[46].

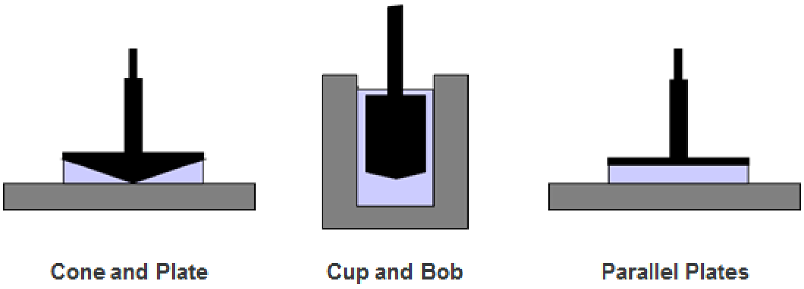

Figure 2.3: Plate-plate, plate-cone and couette geometry for rotational rheometers.[47]

[†] Further influences of gravity on the stress generated by the deformation of the liquid, the velocity field or the orientation of polymer chains has been part of the Extensional Rheology Experiment (ERE) of the NASA in 2000[45].

2.2 Complex fluids

Both Hooke's and Newton's studies on solids and liquids described idealistic responses to stress. So-called Newtonian fluids show a linear relation between shear stress and shear rate. Furthermore, no shear stress is observed at shear rate $\dot{\gamma} = 0$. However, a large number of materials show a behavior different from these predictions. Hence those liquids showing temperature or stress dependent deformation are called non-Newtonian liquids. These phenomena are often observed in colloidal suspensions such as corn starch in water, ketchup, yogurt, blood or toothpaste, where particles of any phase are suspended in another medium[22].

2.2.1 Non-Newtonian fluids

Classical deviations from Newtonian fluid behavior are shear-thickening fluids (dilatant), shear-thinning fluids (pseudo-plastic), time dependent viscosity fluids and Bingham fluids. Shear-thickening materials follow a power law and show increasing viscosity with rising shear rate (see Fig. 2.4). The opposite phenomena of shear-thinning is the decrease of viscosity with rising shear rates.

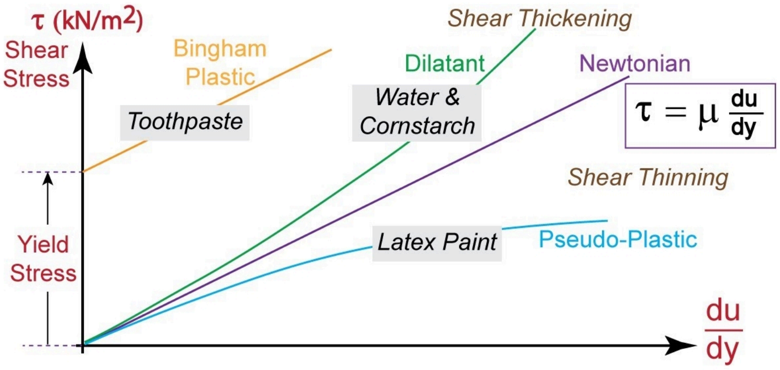

Figure 2.4: Plotted is the shear stress τ over the shear rate (adapted from reference [48]). In violet the linear behavior of Newtonian fluids is shown. For comparison, the power law behavior for shear-thickening (green) and shear-thinning fluids (blue) is plotted together with the offset linear behavior of Bingham plastics (yellow).

For shear-thickening and shear-thinning equation 2.1 is modified to

$$\tau = \mu \cdot \left(\frac{du}{dy}\right)^n \tag{2.9}$$

with $n > 1$ for shear-thickening and $n < 1$ for shear-thinning fluids. The change in flow dynamics originates from intermolecular interaction. Within the scope of this thesis colloidal suspensions were studied with special attention to the influence of particle sizes, shapes, size distributions and volume fractions on these interactions.

On the molecular level one of the driving forces for repulsion and attraction between particles was first described by J. Van der Waals. Van-der-Waals forces[49] describe the attraction between two particles due to the induced dipoles. These dipoles are not permanent but temporally fluctuations of the electron density close to the particles. The potential V decreases fast with increasing distance r:

$$V_{vdW} \propto -\frac{1}{r^6}. \tag{2.10}$$

The concept was extended to macroscopic objects in the Hamaker theory[50] by adding up all forces between the molecules of two macroscopic objects, assuming that the interactions may be treated independently. As a consequence the dependence on the distance r in the van-der-Waals potential is reduced to r^{-2} for colloidal systems.

In order to counteract van-der-Waals forces that drive agglomeration and subsequent sedimentation, colloidal suspensions need to be stabilized. The most frequent mechanisms are steric or electro-statical stabilization. In steric stabilization ligands on the surfaces of the particles act as a compressible spacer leading to repulsive interactions at close particle distances. For instance, thin polymer layers are often used to prevent the particles from sticking together and the volume fraction of a dispersion may determine the state of the phase diagram[51] of hard sphere particles.

For hard spheres, ionisable groups on the surface or polar solvents, electro-static forces prohibit the overlap of particles at distance r smaller than the particle radius R. The potential for charged particles is given by the Yukawa[52] (screened-Coulomb) potential

$$V_{es} \propto \begin{cases} \infty & , r \leq 2R \\ -\frac{\exp - \kappa_D r}{4\pi\varepsilon_0 E_r r} & , r > 2R. \end{cases} \tag{2.11}$$

with κ_D the Debye parameter, which defines the screening length with κ_D^{-1}. $\varepsilon_0 E_r$ denotes an effective permittivity of the electrolyte solution from both solvent molecules and ion contributions[53]. The range of the Yukawa potential is longer than the van-der-Waals potential, and therefore dominates long-distance particle-particle interactions. The resulting potential from both van-der-Waals forces and electro-static stabilization is described in the Derjaguin-Landau-Verwey-Overbeek theory (DLVO)[54]. The total potential for colloidal systems as shown in Fig. 2.5 is composed of the attractive van-der-Waals potential and the repulsive electro-static potential. Additionally, a restriction of overlap for hard sphere particles and a repulsion at small distances r due to a double-layer of counter-ions on the surface of each particle is considered in the Born potential. The resulting V_{total} features two minima with an energy barrier in between. Once a particle has passed through the barrier it will fall into the primary minimum at small r and the particles will agglomerate.

Experimental verification of the theory and measurements of average particle-particle distances

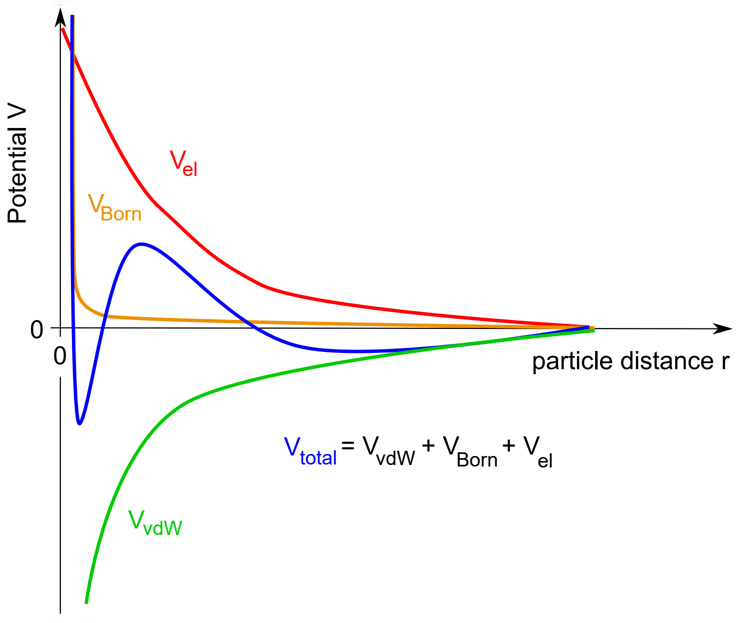

Figure 2.5: The DLVO theory considers attractive and repulsive interaction between particles into a resulting potential V_{total}[55].

became accessible with the development of light scattering techniques. First light scattering experiments on shear-thickening and shear-thinning materials were performed in the 1970s, showing that particle-particle interactions are an insufficient explanation for non-Newtonian fluid dynamics[56]. The particles of a colloidal system not only interact with each other, but also with the medium they are dispersed in. Therefore, the movement of randomly fluctuating particles (Brownian motion) in an incompressible liquid affects the local flow field around each particle, resulting in long range hydrodynamic interaction[57]. The interaction is described in the Stokes equation, a variation of the Navier-Stokes equation[58] for viscous liquids without inertia. For single particles in an incompressible liquid their motion fluctuates randomly dependent on the thermal energy of the system. The diffusion coefficient D_0 is defined by the thermal energy k_BT, the liquid's viscosity μ and the particle's hydrodynamic radius R_H:

$$D_0 = \frac{k_BT}{6\pi\mu R_H}. \tag{2.12}$$

Therein the timescale for particle displacement in Brownian motion is given by R_H^2/D_0 to move in the range of the particle's radius. In rheological studies[15] the relation between diffusion and shear rate is given by the Péclet number Pe:

$$Pe = \frac{\dot{\gamma}R_H^2}{D_0}. \tag{2.13}$$

This dimensionless number is used to assess the impact of shear stress on a colloidal suspension with respect to Brownian motion. Systems with small Péclet numbers $Pe \ll 1$ are dominated by diffusive dispersion. At $Pe \geq 1$ thermal fluctuations cannot overcome the stress-induced particle ordering anymore, so shear-thickening and shear-thinning may occur when the equilibrium between attractive van-der-Waals forces and repulsive stabilization forces is changed from diffusion to advection by applied stress.

Shear-thinning fluids undergo a phase separation, forming layers that have less interparticle interaction leading to a reduced viscosity under shear stress. For long polymer chains also disentanglement may cause less interaction through ordering of the chains in the flow[23,59].

In case of shear-thickening hydrodynamic forces become dominant under stress and the particles suspended in the solvent begin to flocculate, they form flakes called hydroclusters and behave more solid than liquid[22,60]. A sketch of these mechanisms including corresponding microstructures is shown in Fig. 2.6 for a sample liquid. The change may occur between only two or all three phases, as indicated here from equilibrium to layer formation to cluster formation at rising shear rates.

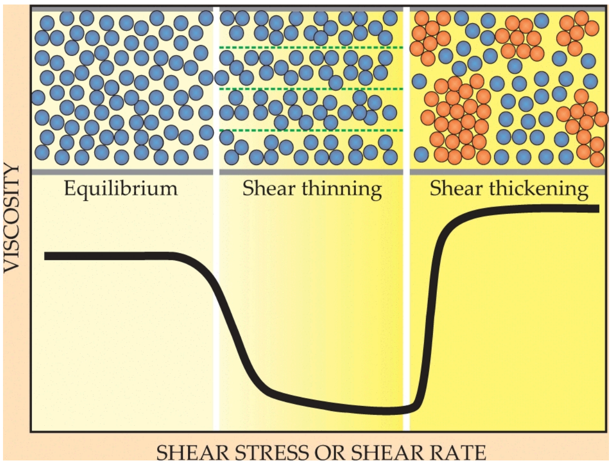

Figure 2.6: Micro structures in colloidal suspensions with shear-thinning and shear-thickening represented by string-like structures and hydroclusters, respectively.[22]

Shear-thinning allows blood to be pumped easily through veins and arteries. In case of injury, the blood pressure lessens and the higher viscosity of blood in equilibrium slows down the blood loss. Next to medical interests, further potential applications in manufactured materials include paints which are easy to spread under the pressure of a brush but do not drip when the brush is lifted. Furthermore, the avoidance of shear-thickening is of great interest for the concrete industry so that congestion in pipes can be reduced[61]. An application for strong shear-thickening effects is found in protective clothing producing companies who research possibilities of a liquid armor hardening fast under powerful impacts[62,63].

2.2.2 Shear of non-Newtonian fluids in a pipe

For Newtonian fluids the shear rate $\dot{\gamma}$ in a pipe is defined only by the flow rate Q and the pipe radius R (see equation 2.7). Non-linear viscosity of non-Newtonian fluids necessitates corrections to the shear rate $\dot{\gamma}_{nN}$ as mathematically described by the Rabinowitch equation[64]:

$$\dot{\gamma}_{nN} = \frac{4Q}{\pi R^3}\left(\frac{3}{4} + \frac{1}{4}\frac{d\ln(Q)}{d\ln(\tau_{wall})}\right) = \dot{\gamma}\left(\frac{3}{4} + \frac{1}{4}\frac{d\ln(Q)}{d\ln(\tau_{wall})}\right). \tag{2.14}$$

For power law fluids as described in equation 2.9 the derivative becomes

$$\frac{d\ln(Q)}{d\ln(\tau_{wall})} = \frac{1}{n}. \tag{2.15}$$

Thus, the Rabinowitch equation 2.14 can be written as

$$\dot{\gamma}_{nN} = \frac{4Q}{\pi R^3}\frac{3n+1}{4n}. \tag{2.16}$$

Beside the shear rate also shear stress τ might differ for non-Newtonian fluids. In short pipes ($L/2R < 100$) the transition from the afflux (Fig. 2.7 a) into the narrow part of the pipe can lead to elastic deformation of the fluid as shown in Fig. 2.7 b. In the Bagley correction (equation 2.17) the pipe length and pressure drop in the system used for equation 2.4 have to include an empirical value e for the additionally entrance pressure:

$$\tau_{wall,nN} = \frac{\Delta P}{2(\frac{L}{R} + e)}. \tag{2.17}$$

Consequently, the viscosity of non-Newtonian liquids is given by

$$\mu_{nN} = \frac{\dot{\gamma}_{nN}}{\tau_{wall,nN}}. \tag{2.18}$$

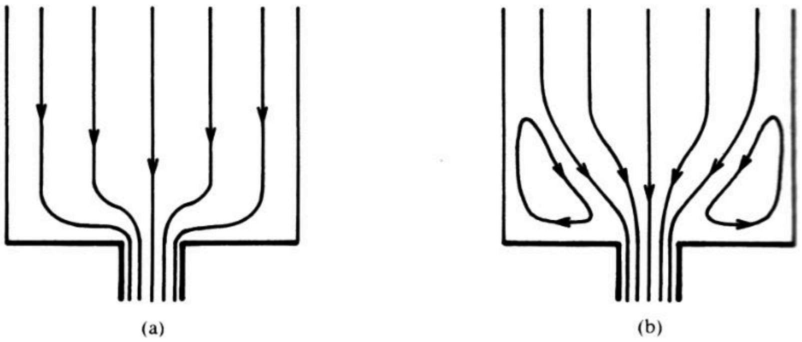

Figure 2.7: a) Afflux from the broad part of the tube into a capillary/microtube. b) Narrowing at the tube entrance can lead to elastic deformation of the fluid in front of the microtube. Consequently, an additional entrance pressure term for the shear stress[64] has to be taken into account.

2.2.3 Bingham plastics and shear history

Another example for a non-Newtonian fluid is the Bingham plastic named after Eugene Bingham[65]. While the viscosity under shear grows linearly, an initial yield stress τ_0 has to be reached before the solid or elastic material becomes a liquid and flows. For such fluids equation 2.1 has to be modified to

$$\dot{\gamma} = \begin{cases} 0 & , \tau < \tau_0 \\ \frac{\tau - \tau_0}{\mu} & , \tau \geq \tau_0. \end{cases} \tag{2.19}$$

Bingham plastic behavior occurs due to the break-up of weak solid phases often present in mud or slurries. The laminar flow for such materials is described in the Buckingham-Reiner equation and plays an important role in drilling engineering[66,67].

Beside the yield stress also the influence of shear history may define a non-Newtonian liquid. Time-dependent viscosity appears in shear-thinning and shear-thickening fluids, named thixotropy and rheopexy, respectively. Unlike the immediate effects of van-der-Waals or electrostatic potentials, other interparticle interactions like chemical bonds do break (or form) only after prolonged stress exposure. The reversal process after removal of the shear stress also takes time to reset into the equilibrium state. The time frame of studied thixotropic and rheopectic materials ranges from seconds to weeks[68]. At such long time scales the terms liquid and solid become transient as they depend on the observation time. For a characterization of the transition between solid and fluid the Deborah number[27] De was implemented. Low numbers $De = \frac{\text{time of relaxation}}{\text{time of observation}}$ imply a more liquid than solid material, but even the very slow creep of granite[69] may be called liquid behavior when observed for a very long time.

2.3 Liquid micro-jets

Liquid jets are, beside from their use as capillary rheometers, common in nature and industry. We encounter them in kitchen taps and medical injections, ink jet printing, fuel injection or high-pressure cleaning systems. Knowledge of the liquid as well as the jetting system allows for precise control, tuning the emitted liquid from sprays to droplets or jets in the range from centimeter to a few micrometers. After the liquid leaves the nozzle tip and enters a free-flowing state, three different regimes are distinguished: The dripping regime, jetting regime and spray. At very low flow rates the liquid will leave the nozzle tip as a continuous stream of droplets. In order to enter the jetting regime characterized by the jet length L_B before the break-up into droplets occurs, the flow has to exceed a minimal velocity v_{min} (see Fig. 2.8). At low jet velocities the jet will flow laminar with increasing jet length. For high v_{jet} more and more pertubations will occur and the flow will become turbulent. In this transition from jetting regime to spray the jet length will first decrease and later increase again together with the emergence of small satellite droplets, which characterizes the atomization of the liquid.

In this work all measurements were performed in the jetting regime at laminar flows.

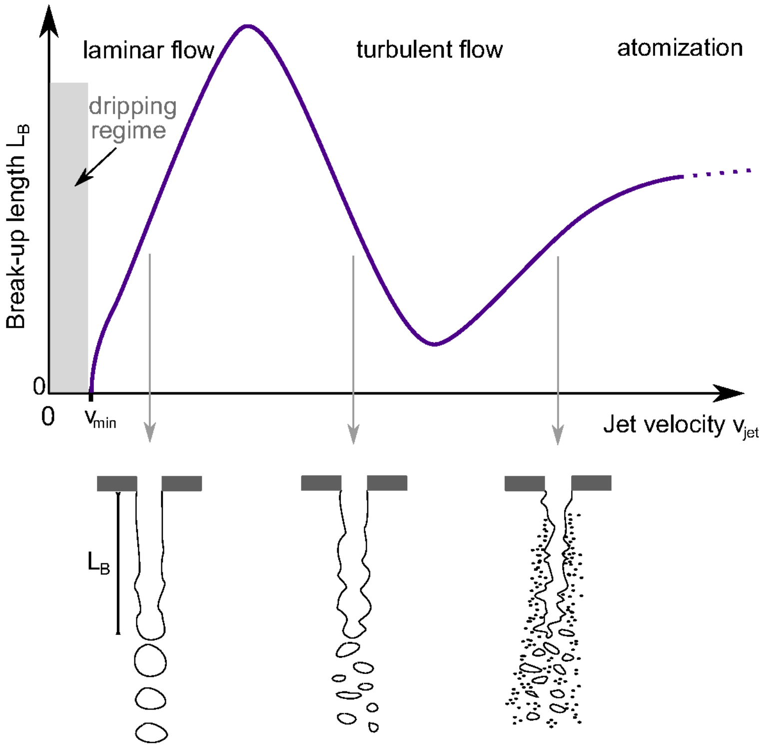

Figure 2.8: Laminar and turbulent jetting regime are distinguished by the break-up length and jet speed (adapted from reference [70]).

2.3.1 Application at synchrotron radiation facilities

Flow might be gravity-induced, drag-induced (Couette flow) or pressure-induced (Poiseuille flow). In small pipes surface tension prevents the liquid from flowing out of the pipe through gravity alone, but if enough pressure is applied, the liquid starts to flow. The process of droplet and jet formation upon exit from a pipe is too fast for the human eye, which is why Rayleigh in 1891 chose this scene as his first example for demonstrating the benefit of ”instantaneous photography”[71].

Jets forming out of pressure-induced flow from a pipe as shown in Fig. 2.9 are today known as Rayleigh jets. As a need for micrometer thin jets arose at X-ray sources over the last decades, more sophisticated schemes of jet mechanics were developed. A setup for an liquid jet experiment at the CXI instrument at the Linac Coherent Light Source (LCLS, California) is shown in Fig. 2.10 a. With this setup serial femtosecond crystallography (SFX) enabled the study of complex protein structures. The nozzle type used for these experiments was developed by Gañán-Calvo[20] in 1998. Gas Dynamic Virtual Nozzles (GDVN) use a focusing scheme as shown in Fig. 2.10 b and Fig. 2.10 c in order to produce very small liquid jets of 1-10 μm thickness. Gañán-Calvo proposed to envelop the pipe providing the liquid with a larger tube perfused by gas, so that the gas uniformly presses on the liquid leaving the pipe orifice, thereby focusing

Figure 2.9: Photography of a liquid jet by Lord Rayleigh. He demonstrated the fast time scales accessible by the newly developed concept of photography by showing droplet break-up, which is too fast for the human eye.[71]

the jet. With different nozzle sizes and gas pressures the jets can be tailored for high velocities[72] of 100 m/s or for small droplets that reach supercooled liquid states down to ≈230 K due to evaporative cooling[6].

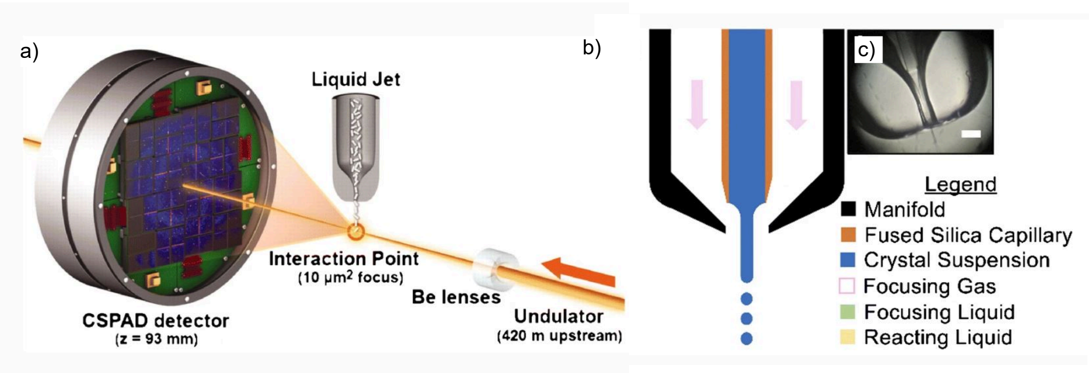

Figure 2.10: a) Application of a liquid jet sample environment for serial femtosecond crystallography (SFX) at an XFEL (CXI instrument, LCLS)[73,74]. b) Schematic for the jet generation from a GDVN and c) photography of an GDNV (adapted from reference [75]).

In view of these properties, jetting systems have become a common feature at free electron laser (FEL) facilities and other synchrotron light sources. Radiation sensitive materials such as biomolecules can only be exposed to the intense X-rays for a short time before damage occurs. The advantage of liquid jets as sample delivery systems is their self-refreshing property, where each light pulse hits a new droplet or fresh jet segment. Structural information of the sample is then contained in the scattered light of a single pulse and destruction of the small affected sample volume due to heating and radiation damage happens after the FEL pulse[1,2,76]. Furthermore, measurements on samples in liquid jets are nearly background-free and emulate natural dynamic environments. However, in order to correctly interpret information from samples carried in a liquid jet, influences on and from the carrier medium like the driving force for droplet formation or liquid-gas interactions after the nozzle exit[14] need to be well understood.

2.3.2 Droplet formation

Precise droplet sizes and droplet emittance frequencies are a requirement for experiments with low sample volumes or for synchronization of droplets and FEL pulses, where each X-ray pulse is matched with one droplet. In order to achieve a controlled system, piezo-electric material is fitted around the nozzles[74]. Voltage signals prompt the expansion and contraction of the material and induce interfering waves in the liquid inside the nozzle, leading to fast droplet emittance from the orifice.

Mechanisms of the jet break-up into droplets and predictions of the jet length L_B for which the jet stays stable were studied since the 19th century[77]. According to Savart, break-up of a jet will occur independent of direction or external forces. It is a spontaneous effect of small pertubations that result in a gain of surface energy. This energy drives the amplitude of the perturbation until the surface curvature is small enough for surface tension to trigger a break-up between the main fluid mass and a droplet. Perturbations or jet instabilities may for example arise from velocity differences between the jet and its surroundings.

The surface tension σ is the result of cohesive forces. Local variation of the electron distribution of the liquid leads to attraction between the molecules. A well known example for this behavior are hydrogen bonds between water molecules[78]. Each H_2O molecule can form up to four hydrogen bonds to neighboring molecules and the strong cohesive force of the bonds ensure the liquid's high surface tension. Molecules at the surface lack a bond partner at one side and therefore are pulled inward. This creates an internal pressure and forces liquid surfaces to contract this area A in order to minimize the surface energy E:

$$\Delta E = \sigma \Delta A. \tag{2.20}$$

The importance of viscous forces in relation to surface tension can be quantified by the dimensionless Ohnesorge number Oh

$$Oh = \frac{\mu}{\sqrt{\rho \sigma L}} = \frac{\sqrt{\mathrm{We}}}{\mathrm{Re}} \sim \frac{\text{viscous forces}}{\sqrt{\text{inertia} \cdot \text{surface tension}}}. \tag{2.21}$$

It entails the liquid density ρ and the typical length scale L (e.g. jet diameter) and may also be expressed through the Weber number We and the Reynolds number Re. Thereby, We is defined as the ratio of kinetic energy of a drop to the surface tension:

$$We = \frac{\rho r_0 u^2}{\sigma}. \tag{2.22}$$

It is a measure of growth of the perturbation in the jet with r_0 the radius of the unperturbed jet and u the mean jet velocity. The Reynolds number Re

$$Re = \frac{\rho r_0 u}{\mu}. \tag{2.23}$$

is a measure for fluid friction at boundary layers which leads to turbulent flows such as eddies and vortices. Laminar flow occurs at low Reynolds numbers, where viscous forces are dominant, while turbulent flow occurs at high Reynolds numbers ($\gg 1000$) and is dominated by inertial forces[79].

While the 'science of flow' has been studied intensively since its beginnings in the 17th century, even today a complete comprehension of the makeup of complex liquids remains missing. High resolution studies on microstructures of for instance colloidal suspensions become only possible with the high performance capabilities of modern X-ray sources and are therefore the aim of this work.

Chapter 3

X-ray scattering

The first work awarded with a Nobel prize in physics in 1901 was the observation and study of X-rays by Wilhelm Conrad Röntgen from 1895. Röntgen observed light emission from charged particles abruptly slowed down by hitting an anode in a partially evacuated tube[80]. The unknown emission was named ”X-rays” and the name remained when later studies characterized it as electromagnetic radiation. Characteristic wavelengths are between 0.1 Å and 100 Å where the radiation is distinguished from gamma rays only through its origin. While gamma rays are a byproduct of radioactive decay, X-rays originate from Bremsstrahlung or electroluminescence. Here, Bremsstrahlung is a continuous spectrum emitted due to the energy loss from scattering a charged particle by an atom or molecule. If during the scattering process an electron is ejected from the inner shell of the atom, electrons from a higher energy level fill the vacancy. The energy difference is then emitted in form of characteristic X-ray radiation in a discrete spectrum.

Already in the late 19th century the practical applications of the newly found X-ray radiation in the medical field were realized. The short-wavelength radiation penetrates material dependent on the atomic number, which enables photographic recordings that distinguish bone or non-biological matter such as metal bullets from soft tissues. The first proof-of-principle photograph showed Röntgen’s wife’s hand with a ring, which initiated a rapid development of X-ray diagnostics.

Today modern 3rd generation storage ring sources and free electron lasers (FELs) produce X-ray pulses with up to multiple keV photon energy[81]. These sources enable the determination of structures at the wavelength of the X-ray, which is several magnitudes smaller than with any other visible light microscopic technique.

3.1 Interaction with matter

The interaction between X-ray photons and atoms or molecules is governed by multiple processes. Depending on the initial energy of the photon, it may scatter or ionize the target material by absorption. The main process relevant for this work is elastic scattering. In a classical non-quantum-mechanic approach this means that atoms or molecules begin to oscillate at the wavelength of the incident light, thereby becoming small dipoles emitting radiation[82]. With the polarization vector $\vec{\varepsilon}$ the incoming electromagnetic wave can be described by

$$\vec{E}(\vec{r},t) = \vec{\varepsilon}E_0 e^{i(\vec{k}\vec{r}-\omega t)}. \tag{3.1}$$

The measurable property of the electric field $\vec{E}$ is the intensity I, which is proportional to the square of the field's amplitude. After a scattering process the initial wave vector $\vec{k_i}$ is changed into the final vector $\vec{k_f}$. Between the initial wave and the final wave a vector transfer $\vec{q}$ is observed as

$$\vec{q} = \vec{k}_f - \vec{k}_i. \tag{3.2}$$

In the scope of this work all scattering experiments were performed in transmission geometry. Thus the refractive index was approximated as $n \approx 1$. With the scattering event observed under the angle 2θ as shown in Fig. 3.1, geometry considerations for $\vec{q}$ are in this instance only dependent on the wavelength λ and yield

$$|\vec{q}| = q = \frac{4\pi}{\lambda}\sin(\theta). \tag{3.3}$$

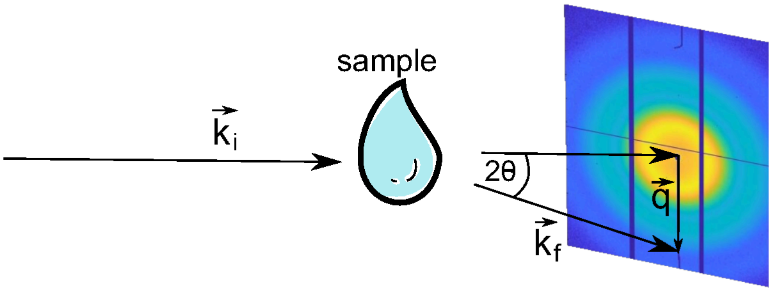

Figure 3.1: Schematic sketch of the geometry of X-ray scattering experiments in transmission geometry.

At low X-ray energies ionization is the prevailing process where bound electrons of the material are ejected from of their shell. The electrons refilling the holes can then emit characteristic, material-specific fluorescence in form of X-ray or lower energy photons. Possible chain reactions of ionization and new X-ray production is a major hazard for living tissue and has to be considered for medical applications. For high energy photons the probability of Compton scattering, and above 1 GeV electron-positron pair production, increases. In Compton scattering the X-ray photon is inelastically scattered at the weakly bound outer shell electrons of the material. The energy lost by the change in direction of the photon leads to an increase of its wavelength.

All absorption processes strongly depend on the wavelength λ of the incident X-ray photons and the material. With Z the atomic number describing the quantity of protons in the nucleus, the decrease of intensity due to absorption is expressed by the Lambert-Beer law

$$I = I_0 \cdot e^{-\mu d_m}, \tag{3.4}$$

with I_0 the initial intensity, d_m the thickness of the material and the absorption coefficient μ proportional to $Z^4\lambda^3$.

3.2 Small-angle X-ray scattering (SAXS)

Small angle X-ray scattering (SAXS) is a technique for characterizing sub-micrometer structures in materials[83]. Due to the typical wavelength of X-rays and the detection under an angle below 5°, structural information in the range of 1-100 nm in size are typically accessible. The technique relies on density differences revealed via elastic scattering in transmission geometry and can be used to identify particle sizes and shapes as well as particle distributions or localized structural order.

3.2.1 Form factor

When light is transmitted through a sample volume, the scattering by atoms and molecules will lead to an intensity distribution I along the wave vector transfer $\vec{q}$. The intensity is defined by the product of the scattered wave amplitude A and its complex conjugate A^*:

$$I(\vec{q}) = A(\vec{q})A^*(\vec{q}). \tag{3.5}$$

For scattering of objects with a density difference $\Delta\rho$ to the surrounding material and an object volume V_p the intensity is given by

$$I(\vec{q}) = \Delta\rho^2 {V_p}^2 \left|F(\vec{q})\right|^2. \tag{3.6}$$

Therein, the form factor $F(\vec{q})$ represents a measure of scattering amplitude. $F(\vec{q})$ consists of a Fourier transformation of the spatial electron density distribution from real space into reciprocal space. The transformation means that broad distributions of the sample in real space produce small distributions and a fast decay of $F(\vec{q})$ in reciprocal space. Assuming single scattering events in Born approximation as well as a far-field approximation, i.e. a sample-detector distance is much larger than the sample size, the scattering from electrons at position $\vec{r}$ is

$$F(\vec{q}) = \int_V \rho(\vec{r}) e^{(i\vec{q}\vec{r})}\, d\vec{r}. \tag{3.7}$$

In the framework of this thesis all scattering objects were colloidal systems of solid particles dispersed in liquids. The form factor projects the morphology of the particles, it is therefore suitable to determine sample sizes and shapes. $F(\vec{q})$ can be calculated analytically only in limited cases, for example for a single spherical particle of radius R, one obtains

$$\begin{aligned} F(\vec{q}) &= \frac{1}{V_p}\int_{V_p} e^{(i\vec{q}\vec{r})}\,dV_p \\ &= \int_0^R \int_0^{2\pi} \int_0^{\pi} e^{iqr\cos(\theta)} r^2 \sin(\theta)\,d\theta\,d\phi\,dr \\ &= \frac{1}{V_p}\int_0^R 4\pi \frac{\sin(qr)}{qr} r^2\,dr \\ &= 3\left[\frac{\sin(qR) - qR\cos(qR)}{q^3R^3}\right]. \end{aligned} \tag{3.8}$$

The isotropic particle shape results in an isotropic $\vec{q}$-dependence, i.e. $F(\vec{q}) = F(q)$. As shown in Fig. 3.2, the function yields $F(q) = 1$ at $q = 0$ and shows an oscillatory decrease to 0 at larger q. The size of the oscillations is defined by the particle size. According to the Porod law the spherical form of the particles is also indicated by the decrease of $\frac{1}{q^4}$ for $F(q)$ at $qR \gg 1$.

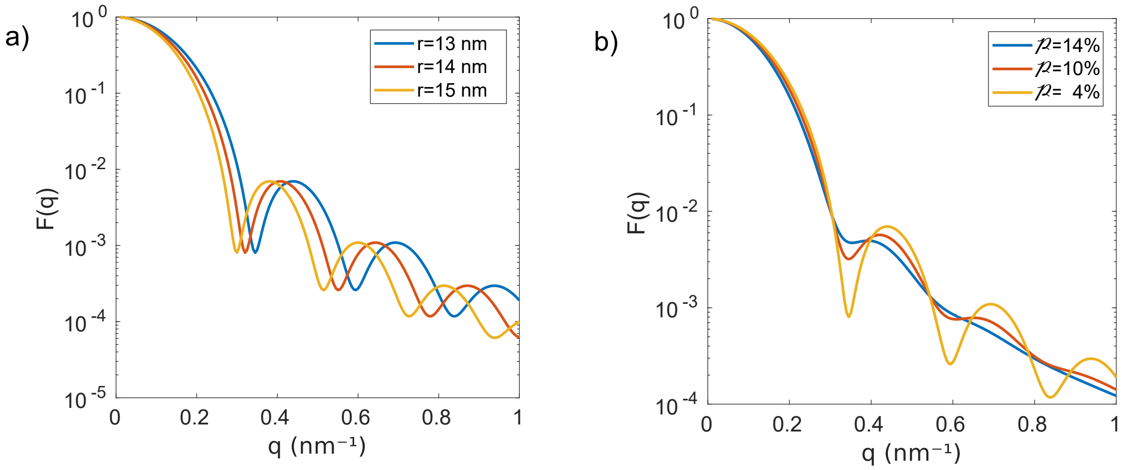

Figure 3.2: Form factor $F(q)$ for a) different particle sizes r at $\wp = 4\%$ and b) high and low dispersities $\wp = \sqrt{\frac{1}{z+1}}$ (cf. equation 3.10) for particles $r = 13\,\mathrm{nm}$.

Beside morphology influences, also the size distribution within the scattering volume changes the scattered intensity. With the particle size distribution function $D(R)$ equation 3.6 becomes

$$I(\vec{q}) = \Delta\rho^2 \int_0^{\infty} D(R) V_p(R)^2 \left|F(\vec{q},R)\right|^2 dR. \tag{3.9}$$

With particle size R, mean particle size $\bar{R}$ and z the spread in particle size the distribution can be described via the Schulz-Zimm distribution[84] as

$$D(R) = \left[\frac{z+1}{\bar{R}}\right]^{z+1} \frac{R^z}{\Gamma(z+1)} \exp^{-(z+1)\frac{R}{\bar{R}}} \quad \text{with} \quad \int_0^\infty D(R)dR = 1. \tag{3.10}$$

High dispersity suppresses the oscillations in the intensity (see Fig. 3.2 b). As all samples have at least a slight distribution in the particle size and therefore a dispersity $\not{p} = \sqrt{\frac{1}{z+1}} \neq 0$, all measured data shows a finite number of oscillations with minima larger than 0.

3.2.2 Structure factor

The formation of short-range order by inter-particle interactions has to be accounted for in highly concentrated sample systems[83]. Therefore, SAXS analysis of the intensity distribution from scattered light gets an additional component for samples with significant particle-particle interaction. In those cases the structure factor $S(\vec{q})$ for spherical particles is not equal to 1 and can be multiplied by the form factor in order to obtain the intensity:

$$I(\vec{q}) \propto |F(\vec{q})|^2 \cdot S(\vec{q}). \tag{3.11}$$

The structure factor as shown in Fig. 3.3 results in a change of the intensity distribution at small $\vec{q}$ and becomes 1 for larger $\vec{q}$. It relates to the probability of finding particles at a specific distance r from each other, which is summarized in the pair distribution function $g(\vec{r})$. Oscillations in $g(\vec{r})$ show a pronounced first maximum which corresponds to a structural mean inter-particle distance. The pair distribution is mainly determined by the potential $V(\vec{r})$ that depicts the interaction between the particles[85]. The relation between $g(\vec{r})$ and $V(\vec{r})$ is given in the Ornstein-Zernike equation[86]. Hitherto the structure factor

$$S(\vec{q}) = 1 + \rho \int (g(\vec{r}) - 1)e^{i\vec{q}\vec{r}} d\vec{r} \tag{3.12}$$

can be calculated for a few well defined potentials. Together with the Percus–Yevick approximation as a closure relation a solution was found for hard spheres for 1-40 vol% with the concentration as the only variable[87]. For electro-statically stabilized systems a solution for $S(\vec{q})$ was found[88] in 1981 using the mean spherical approximation (MSA). Later the approximation was refined into the rescaled mean spherical approximation[89](RMSA) in order to avoid negative contact distances for long-range interaction. The charged particles are described by a screened Coulomb inter-particle potential (see equation 2.11), therefore their structure factor depends not only on the volume fraction, but also on the particle's effective charge, the permittivity of the suspending medium and the ionic strength of the surrounding medium[90]. In Fig. 3.3 three structure factors calculated by RMSA are shown at concentrations 14 vol%, 18 vol% and 22 vol%.

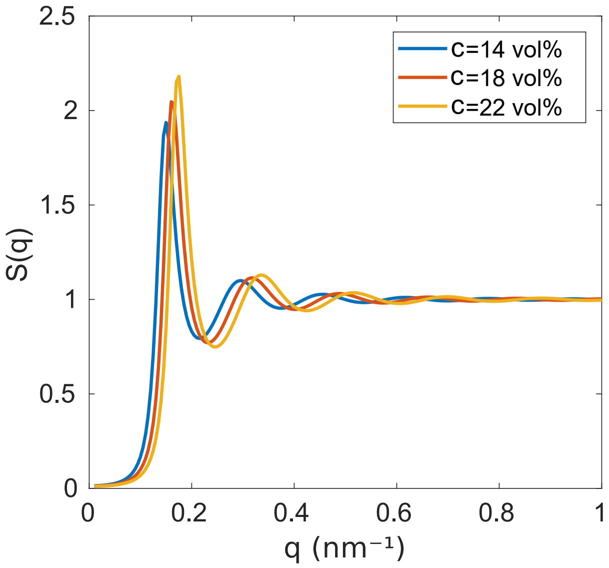

Figure 3.3: Structure factor S calculated with the RMSA for three different particle concentrations. The particle size was set to 15 nm with a charge of 75e$^-$, no salt, room temperature and permittivity $\varepsilon = 73$.

3.3 X-ray cross-correlation analysis (XCCA)

As described in section 3.2.2, the structure factor contains information on the degree of short-range order. However, $S(q)$ only reveals particle-particle correlations as an average over the illuminated sample volume. X-ray cross-correlation analysis (XCCA) has been developed to overcome these limitations and for studying the dominating order in locally formed structures of disordered samples[91]. High coherent flux and short exposure times are necessary to avoid spatial and temporal averaging in the intensity distribution of the scattered light. Under the conditions provided by modern X-ray sources the dynamic evolution of localized symmetries in samples such as fast relaxing liquids can be observed by XCCA. Furthermore, the technique can reveal intermediate steps of crystal growth by analyzing emerging Bragg reflections or determine the degree of anisotropy in a scattering pattern[92,93].

For XCCA the power spectrum of the intensity is calculated over the azimuthal angle φ in order to obtain information on the bond-ordered structures of a sample:

$$\left|\hat{I}_\ell(q)\right|^2 = \left|\int_0^{2\pi} I(q,\varphi)e^{il\varphi}d\varphi\right|^2. \tag{3.13}$$

$\hat{I}_\ell$ denotes the Fourier coefficients of $I(q,\varphi)$, where ℓ denotes the symmetry[94]. The correlation function

$$C(q,\Delta) = \frac{\langle I(q,\varphi)I(q,\varphi+\Delta)\rangle_\varphi - \left\langle I(q,\varphi)^2_\varphi\right\rangle}{\left\langle I(q,\varphi)^2_\varphi\right\rangle} \tag{3.14}$$

compares two intensities at the same q but with an angular difference Δ. Via the Wiener-Khinchin theorem $C(q,\Delta)$ is connected to the Fourier coefficients $\hat{I}_\ell(q)$ of $I(q)$ by the power spectrum

$$\hat{C}_l = \left|\hat{I}_l\right|^2. \tag{3.15}$$

3.4 Rheology experiments at X-ray sources

The combination of rheological studies with scattering techniques has been implemented in the 1990s, when first small-angle neutron scattering (SANS) and SAXS experiments were performed on sheared colloidal liquids[95–97]. Shear-induced ordering and shear distortion of microstructures in liquids were observed on hard sphere dispersions with rotational rheometers at shear rates up to $10^3\,\mathrm{s}^{-1}$. Later on, structures of microgels[98] and colloidal glasses[13] were resolved and linked to their visco-elastic properties by observing nearest-neighbor configurations. Transitions from liquid or gel-like states into crystallization[12] has been studied as well as the anisotropy of directionally dried colloids[99].

In recent years synchrotron radiation facilities like PETRA III or ESRF have implemented setups for combined SAXS and rheology studies[100,101]. Thereby, the facilities enabled standardized experiments on ordering in colloidal crystals, dynamics in shear flows or shear-induced deformation of complex liquids, for instance the alignment of hematite spindles in ferrogels[102]. Possibilities for time-resolved studies, e.g. tracking the mobility of nanoparticles, has been studied at the Advanced Photon Source (APS) at Argonne National Laboratory with X-ray photon correlation spectroscopy (XPCS) in combination with microfluidic devices[103].

All experiments mentioned above have in common their method of applying shear with rotational rheometers. In the frame of this work, SAXS studies on sheared systems in liquid micro-jets[104] are presented. Unlike the oscillatory flows provided by plate-plate or couette geometry in classical rotational rheometers, micro-jets are working with the principle of capillary rheometers[59]. Thereby, jets can reach shear rates of $\geq 10^5\,\mathrm{s}^{-1}$ and are thus suitable for low viscosity liquids like colloids in water ($\mu \approx 1\,\mathrm{mPa}\cdot\mathrm{s}$). Although the application of liquid micro-jets for rheometry offers advantages for many fluid systems, liquid jets are today more commonly found in sample delivery systems, which disregard possible shear-induced effects on the delivered sample.

Chapter 4

Experimental setup

In this chapter all colloidal systems investigated in this study are introduced. Characterization was performed with transmission electron microscopy at the Universität Hamburg and SAXS measurements at PETRA III. Specifics of the beamline P10 are given in section 4.2. The custom-made sample chamber utilized during two experiments at P10 is described in detail in section 4.3, which is followed by the introduction of the experimental procedures.

4.1 Samples

Two types of colloidal silica particles dispersed in water were studied. The first system consisted of charged stabilized Ludox TMA particles (Sigma-Aldrich, 420859). The approximately spherical shape and broad size distribution of the particles is shown in transmission electron microscopy (TEM) image in Fig. 4.1 a. TEM is not ideal for size or distribution measurements, since the particles have to be dried, which may influence their outer shell. Therefore, form factors of particles dispersed in water were measured with SAXS at beamline P10, PETRA III and are shown in Fig. 4.2. The volume fraction of c = 0.2 was diluted 1:50 in order to avoid inter-particle interaction and to measure the pure form factor only. The data were fitted with equation 3.2.1 and yielded a mean radius of r = 15.1 nm and a size dispersity of $\wp = 12.4\%$. Due to probable multiscattering[105] events the fit of the form factor deviates from the measured data at large q, yielding $\wp = 12.4 \pm 1.3\,\%$.

The second system consisted of colloidal silica particles in water produced in-house by applying the Stöber process[106]:

$$\mathrm{Si(OEt)_4} + 2\mathrm{H_2O} \rightarrow \mathrm{SiO_2} + 4\mathrm{EtOH} \tag{4.1}$$

By tuning the amount of added ammonia and tetraethyl orthosilicate (TEOS) the speed of the hydrolysis was regulated and the size of the obtained SiO_2-spheres could be controlled. The three synthesized samples S, M and L were characterized by TEM and SAXS and are shown in Fig. 4.1 b and Fig. 4.3, respectively. Sizes, concentrations and the polydispersity are summa-

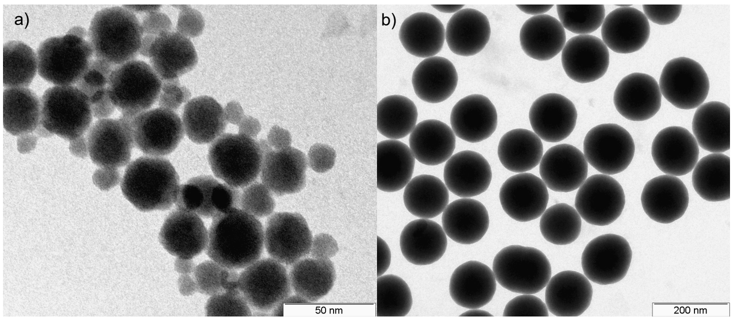

Figure 4.1: a) Ludox TMA measured with transmission electron microscopy (TEM). The approximately spherical form as well as a wide size dispersity ($r \approx$5-15 nm) of the particles is made visible. b) Sample L measured with TEM. The diameter of the SiO_2 particles is $r \approx$70-80 nm.

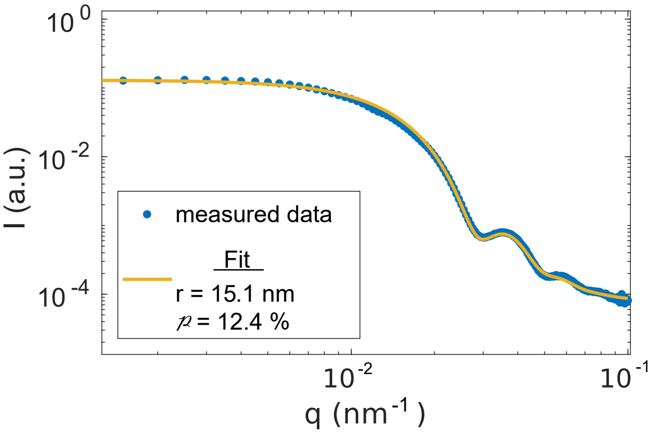

Figure 4.2: Form factor measurement of Ludox TMA at a dilution of $1:50$. The particle size was obtained by a fit as $r = 15.1\,\text{nm}$ with a polydispersity of $\wp = 12.4\%$.

rized in Tab. 4.1. The sample concentrations were determined by measuring the weight fractions. In that process $200\,\mu\text{l}$ sample volume were weighed, then dried and weighed again. The concentration values noted in Tab. 4.1 relate to data taken before the samples were measured with X-rays in the setup described in chapter 4.3. Water residue from the cleaning of pipes in between sample changes lowered the sample concentration by $\approx 1\text{vol}\%$ during experiments.

After the experiments with pure silica particles in water further studies were performed on the system by adding salt. Salt solutions were chosen instead of crystalline salt in order to avoid blockages in the setup by the salt crystals as well as to avoid high salt concentration at localized spots in the sample. Solutions were prepared with the monovalent KCl and the bivalent $MgCl_2$. The concentration in the colloidal silica system was tuned from $50\,\frac{\mu\text{Mol}}{\text{l}}$ up to $4.2\,\frac{\text{mMol}}{\text{l}}$.

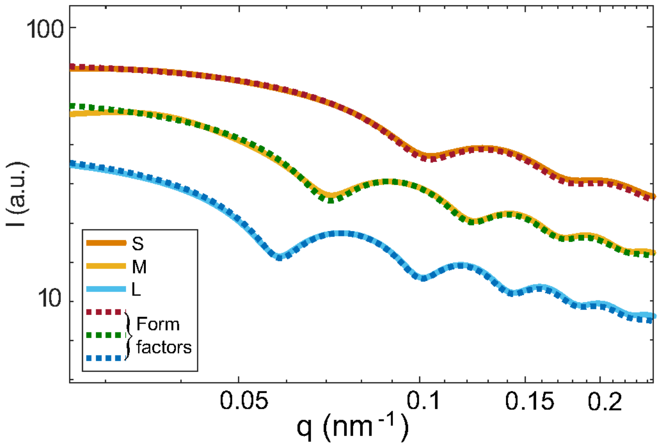

Figure 4.3: SAXS of samples S, M and L with fitted form factors (dashed lines). Particle characteristics are shown in Tab. 4.1.

Sample	radius r (nm)	polydisperity $\wp$ (%)	concentration (vol%)
S	43	10.0	7.9
M	63	7.4	8.1
L	76.5	6.3	12.1
Ludox TMA	15.1	12.4	20.1

Table 4.1: Comparison of size, distribution and maximum concentration between the three samples S, M and L synthesized in-house and Ludox TMA (Sigma-Aldrich).

4.2 Beamline P10 at PETRA III

The experimental data for this work were measured during two scattering experiments performed in SAXS geometry at beamline P10, PETRA III, Hamburg, Germany[107]. A schematic layout of the beamline hutch EH2 is shown in Fig. 4.4. The two-dimensional SAXS patterns were acquired with beamsizes of $1\,\mu\text{m} \times 0.8\,\mu\text{m}$ and $2.5\,\mu\text{m} \times 3.5\,\mu\text{m}$ (vertical×horizontal), which were obtained by compound refractive lenses (CRL)[108] at photon energies of 8.26 keV and 8.06 keV, respectively. The distance between sample and detector was 5 m and an EIGER X-4M detector[109] with 2070×2167 pixels and $75\,\mu$m pixelsize was used. Therefore, the probed range of the wave-vector transfer was $q \cong 0.05\text{-}1\,\text{nm}^{-1}$.

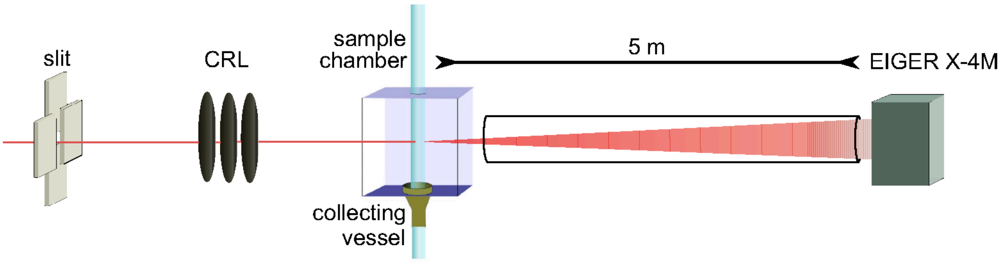

Figure 4.4: Schematic layout of the P10 beamline.

4.3 Jet system

For the generation of Rayleigh jets polyimide coated micro tubes (Polymicro Technologies) with diameters of $75\,\mu$m, $100\,\mu$m and $150\,\mu$m were used as nozzles. Additionally to the cylindrical micro tubes (type TSP) also square micro tubes (type WWP) with $W = 100\,\mu$m edge length were tested. The length of the microtube was less than 15 cm (see Fig. 4.5).

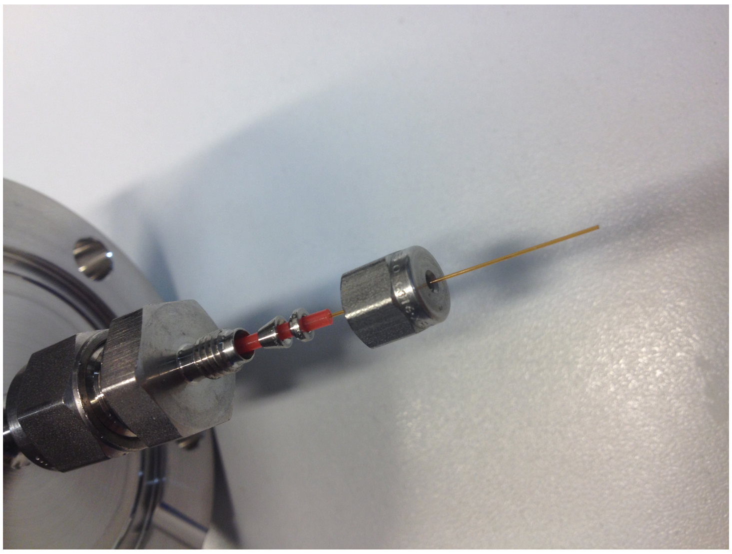

Figure 4.5: Installation of a polyimide coated micro tube. The inner part consists of fused silica, the outer side of both cylindrical and square micro tubes is coated with polyimide to a total diameter of $363\,\mu$m.

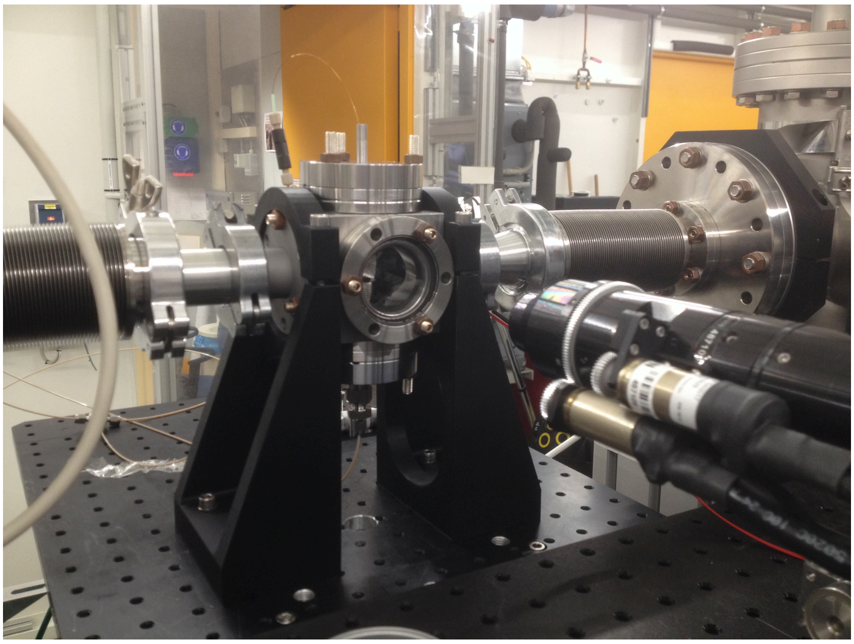

Figure 4.6: Installation of the liquid jet chamber at beamline P10 at PETRA III.

The microtubes entered a custom-made sample chamber modified from previous studies[110] from the top, creating a vertical-flowing liquid jet that was collected ≈ 30 mm further down in a collection device (see Fig. 4.6). The chamber consists of a CF40 cube of 70 mm edge length and flanges containing Kapton windows for the connection to the beamline. Two additional windows on the side of the cube perpendicular to the beam path allowed for observation of the jet during measurements via a microscope. Sufficient back-illumination of the sample was provided by a LED flashing with 1 ms exposure time at 10 Hz, therefore not only the jetting regime but also the transition from jetting to break-up into droplets became observable. For reduction of background scattering the chamber was flushed with a continuous flow of approximately 1 l/h helium during the measurement.

The system for producing continuous flow through the nozzle is shown as a schematic sketch in Fig. 4.7. In total four syringe pumps pressed the liquid sample through the tube system. In the pumping cycle two mid pressure pump modules neMESYS (cetoni) with 5 ml steel syringes provided the flow with up to 100 bar pressure. Both syringes were filled with the sample liquid through a mechanical valve (beige lines) and rejected the liquid (green lines) through a pressure sensor and a second valve. The rejection tubes from both syringes were connected by a T-piece adapter before entering the sample chamber. The switch between both pumps was pressure controlled via the QmixElements software[111]. In the pressure controlled mode one syringe injects liquid into the system while the other refills. The refilling happens faster than the injecting, which gives the system time to already apply and stabilize pressure in the newly refilled syringe. Therefore, uninterrupted flow was ensured.

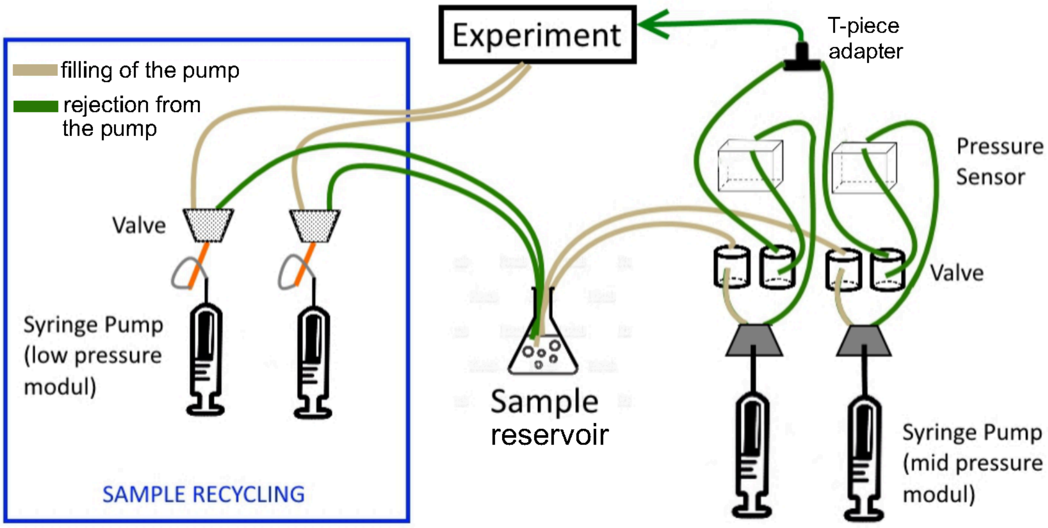

Figure 4.7: Schematic sketch of the four syringe pumps driving the jet system. Two mid pressure modules cycle the sample into the liquid jet chamber in continuous flow mode, while two low pressure modules drive the recycling system.

The collecting vessel at the bottom enabled the installation of two further syringes that recycled the sample. For the recycling two low pressure pump modules neMESYS were fitted with 25 ml glass syringes. In a similar system as in the pumping cycle, the recycling system filled the syringes from the collecting device on after the other. Regulated by electronically switching valves one pump pressed the collected liquid back to the sample reservoir while the second started collecting liquid from the experiment. The installation at the beamline is shown in Fig. 4.8. Measurements were performed at flow rates between 800-3000 $\frac{\mu l}{min}$ with 50 ml total sample volume. The recycling system was driven with a flow rate of 5000 $\frac{\mu l}{min}$, removing about 1.5 times more volume than what was delivered to cover the whole sample volume including bubbles and air. For the smallest microtube of 75 μm diameter with a maximal flow rate of 1400 $\frac{\mu l}{min}$ the sample volume required for a continuous flow could be reduced to 25 ml.

Figure 4.8: Installation of the pumping system driving the jetting at the beamline P10 at PETRA III.

The jet velocities with the parameters mentioned above ranged from 1.7-5.3 $\frac{m}{s}$. Such velocities cover a range of shear rates $\dot{\gamma} = 0.9\text{-}5.6 \cdot 10^5\,s^{-1}$, which for the Ludox TMA sample corresponds to Péclet numbers from 1.4 to 8.8. For the largest sample L experiments were performed with *Pe* ranging from 670 to 1170. With the Hagen-Poiseuille law (equation 2.2) the viscosities of the samples could be estimated to 1.3 mPa·s for samples S, M and L. The Ludox TMA sample yielded 2.4 mPa·s while in flowing conditions, which closely resembles the 2.7 mPa·s indicated by the manufacturer.

4.4 Experimental Procedures

Before the start of the experiments the position of the mounted nozzle had to be determined with absorption measurements by scanning the tubes through the X-ray beam and measuring the transmitted intensity. For the microtubes with a square inner diameter the alignment was adjusted after the diode scan for the X-ray to impinge upon the flat side of the square. After starting the syringe system at least two pump cycle iterations waiting time ensured a minimal amount of air in the pipe system, which caused stable jetting. During the measurements the microscope illuminated by a flashing LED enabled the verification of stability in the jet as well as an approximation of the break-up length. During the experiment the liquid jet was screened horizontally with 1 to 8 μm steps and vertically at intervals of 100-200 μm.

Before changing the sample system all tubes were flushed with pure water for at least 15min. In addition the glass syringes from the recycling system were dismounted and cleaned from residual nanoparticle dispersion. Water from the cleaning was ejected from the system by at least two pumping iterations done with air.

The salt solution was added to the sample reservoir during ongoing operation. An even distribution was achieved by 30 min waiting time at maximum flow rate between the addition of the salt and the first measurement on the jet. In order to avoid dilution of the sample concentration only small volumes of 50 μl to 1 ml of the salt solution were added to the sample liquid. Thus the effective decrease of the volume fraction lies in the range of error from the concentration measurement.

Chapter 5

Experimental results

This chapter reports the experimental results for four colloidal silica systems in water. As the main topic of this work the Ludox sample ($r = 15\,\mathrm{nm}$) was characterized and then compared to samples S ($r = 43\,\mathrm{nm}$), M ($r = 63\,\mathrm{nm}$) and L ($r = 76.5\,\mathrm{nm}$). At shear rates up to $\dot{\gamma} = 10^4\,\mathrm{s}^{-1}$ time-resolved studies were performed on structure formation in round and square Rayleigh nozzles of different sizes. Relaxation from the ordered system back into an equilibrium state after shear cessation showed a strong dependence on the Péclet (Pe) number of the system, which was probed in a range $1 \leq Pe \leq 1162$.

5.1 Scattering patterns from SAXS measurements

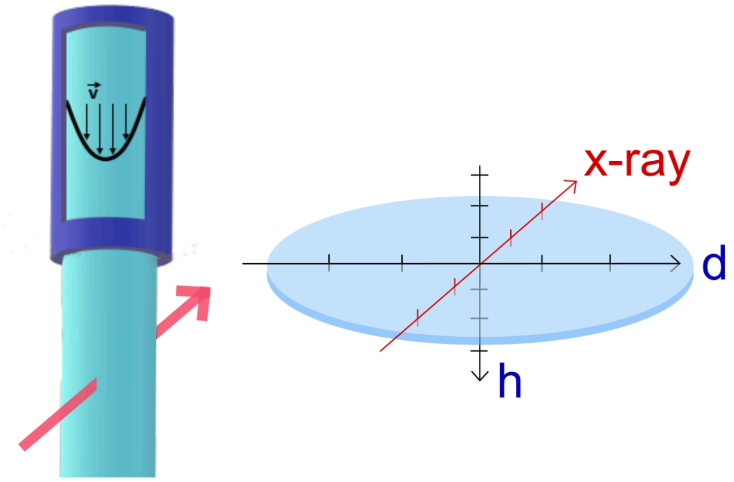

Figure 5.1: Sketch of a Rayleigh nozzle. The X-ray beam hits the jet perpendicular to the flow direction with $h = 0$ at the nozzle tip. The center of the jet is defined as $d = 0$ with $d > 0$ denoting the right-hand side of the jet with respect to the incoming X-ray beam.

The setup as described in chapter 4 was used in two measurement campaigns, providing shear rates up to $5 \cdot 10^5\,\mathrm{s}^{-1}$. Fig. 5.1 shows a sketch of a Rayleigh nozzle and a liquid jet. The h-axis is located vertically along the flow direction with $h = 0$ denoting the position of the nozzle tip.

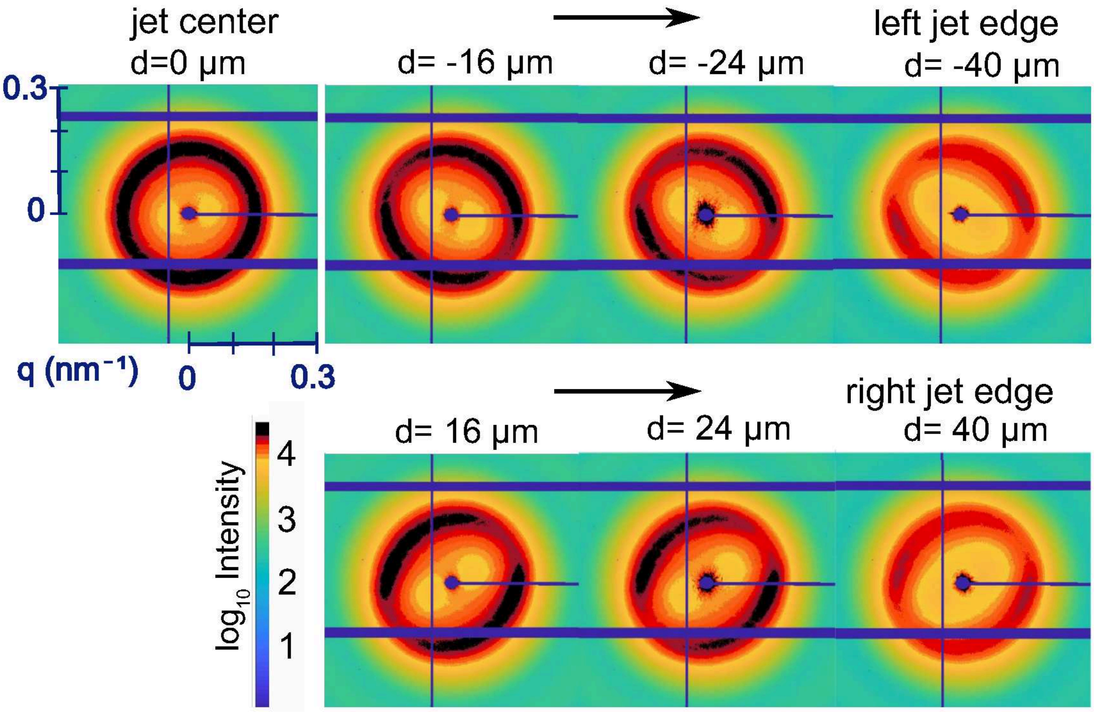

Figure 5.2: Scattering patterns at different positions in the horizontal jet profile for the Ludox sample. The patterns were taken at $h = 150\,\mu\text{m}$ for a jet of $100\,\mu\text{m}$ diameter and show an asymmetric intensity distribution for $d \neq 0$. The q-range amounts to $\pm 0.3\,\text{nm}^{-1}$.

The d-axis is perpendicular to the h-axis. It lies in the horizontal plane through the vertically flowing jet with $d = 0$ denoting the center of the jet. From the viewpoint of the incoming X-ray beam $d < 0$ defines the left-hand side of the jet, $d > 0$ the right-hand side.

Fig. 5.2 shows a selection of scattering patterns for $h = 150\,\mu\text{m}$ at different d for the Ludox sample. The data were acquired with $4\,\mu\text{m}$ beamsize at 8 keV. The patterns show the summed intensity of 10 diffraction patterns taken with 1 s exposure time each. When the beam impinges on the center of the jet ($d = 0$) the diffraction pattern is symmetric and shows an annulus of isointensity scattering at $q = 0.17\,\text{nm}^{-1}$. At $d \neq 0$ the intensity in the annulus is no longer constant but 2-fold modulated along the azimuthal direction. The ring-like pattern distorts with increasing $|d|$ towards an oval shape. The positions of the azimuthal intensity minima (and maxima) remain at the same azimuthal angles for $d \leq 0$ (and $d \geq 0$) respectively, but are mirror symmetric about the vertical axis.

For a more detailed analysis of the Ludox sample the intensity values of the first maximum at $q \cong 0.17\,\text{nm}^{-1}$ were integrated azimuthally over circular sections of $\Delta\varphi = 5°$. Fig. 5.3 a and b show a diffraction pattern and the distribution of the intensity along φ for $d = 24\,\mu\text{m}$ for the Ludox sample, respectively. The mirror case at $d = -24\,\mu\text{m}$ is shown in Fig. 5.3 c. The left- and right-hand side of the jet show a mirror-inverted behavior with two intensity maxima per period (0-180°). On the right-hand side of the jet center ($d = 24\,\mu\text{m}$) the first maximum appears

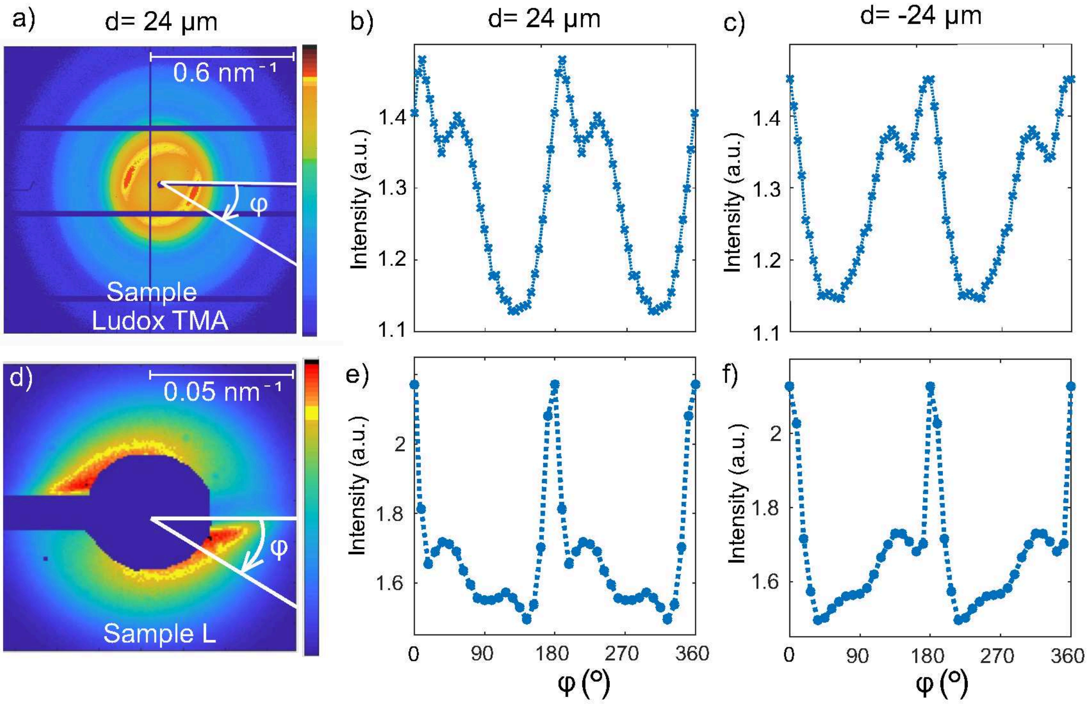

Figure 5.3: a) The diffraction pattern at $d = 24\,\mu$m from Fig. 5.2 is shown for the Ludox sample. The azimuthal angle $\varphi = 0°$ is set to the right side of the pattern and moves clock-wise with respect to the X-ray beam direction. b) Peak intensities integrated over circular sections of 5° for $d = 24\,\mu$m and c) for $d = -24\,\mu$m. d) The diffraction pattern at $d = 24\,\mu$m for the sample L. e) Peak intensities integrated over circular sections of 9° for the right-hand side of the jet ($d = 24\,\mu$m) and f) for the left-hand side of the jet ($d = -24\,\mu$m).

at $\varphi = 10° \pm 2°$ and the second less pronounced one at $55° \pm 2°$ (Fig. 5.3 b). A minimum in intensity can be observed between $\varphi = 125°$ and 145°. In Fig. 5.3 c on the left-hand side of the jet the maxima are located at $175° \pm 2°$ and $125° \pm 2°$, respectively, and the minima lies between $\varphi = 40°$ and 65°. Thus, the relation can be described as $I(d, \varphi) = I(-d, 180° - \varphi)$. The anisotropic scattering patterns relate a direction-dependent intensity to a φ-dependent particle ordering in the jet, which was further studied by XCCA (see section 5.2.1)

In order to compare between the Ludox sample and the larger particles, a diffraction pattern and the corresponding intensity dependence over φ is shown for sample L in Fig. 5.3 d-f. Here, the intensity values of the first maximum at $q \cong 0.04\,\mathrm{nm}^{-1}$ were integrated over azimuthal sectors of $\Delta\varphi = 9°$. At $d = 24\,\mu$m the first maximum appears at $\varphi = 0° \pm 4°$ and a secondary one at $36° \pm 4°$ under scattering conditions comparable to the Ludox sample, while in the mirror case ($d = -24\,\mu$m) maxima are found at $\varphi = 180°$ and $\varphi = 144°$, respectively. The resemblance of the intensity distribution over the azimuthal angle for both sample systems underlines that hydrodynamic properties of the jet have the strongest influence on the particle ordering, independent of particle size or volume fraction.

This is also true for the locations of the maxima and minima, which are comparable for both samples, while the form of the intensity distribution for the large particles is masked by the beam stop. The ring of high intensity which was observed for the Ludox sample seems to be less developed in the diffraction pattern from sample L. The pattern in 5.3 d splits into two-parts and the intensity peaks stretch out to higher q-values. Further diffraction patterns for sample L across the profile of the jet are shown in the appendix (Fig. A1).

5.2 Structure factors

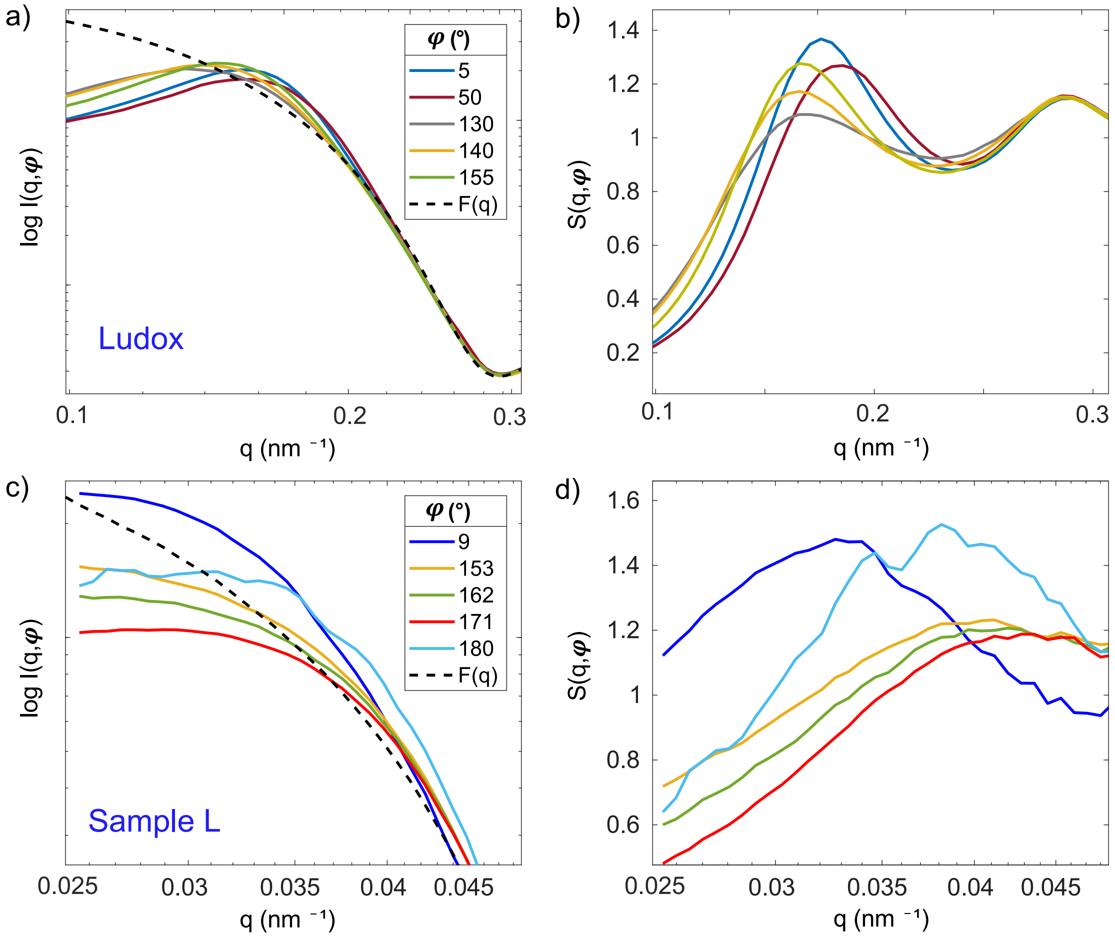

Figure 5.4: a) Intensity $I(q,\varphi)$ of the Ludox sample integrated over circular sectors of $\Delta\varphi = 5^\circ$ and b) structure factors calculated from the intensities shown in a). The measurements were performed at $d = 24\,\mu$m with the $100\,\mu$m square nozzle, flow rate $Q = 1600\,\mu$l/min at $h = 250\,$mm nozzle distance. c) Intensity $I(q,\varphi)$ of sample L integrated over circular sectors of 9° and d) structure factors calculated from the intensities shown in c). The measurements were performed at $d = 24\,\mu$m with the $75\,\mu$m round nozzle, flow rate $Q = 800\,\mu$l/min at $h = 100\,$mm nozzle distance.

The intensity distribution $I(q,\varphi)$ for a case of strong asymmetric scattering is shown in Fig. 5.4 a for Ludox and in Fig. 5.4 c for sample L, respectively. The displayed q-ranges are scaled for the differently sized particles in the Ludox sample and sample L. Variations for different values of φ become more pronounced in the structure factor $S(q,\varphi)$, where the intensity was divided by the form factor $F(q)$ (equation 3.11). In the $S(q)$ shown in Fig. 5.4 b and d the first maximum shifts in peak height as well as in the q-position, which was further analyzed in chapter 5.3.

5.3 XCCA & RMSA results

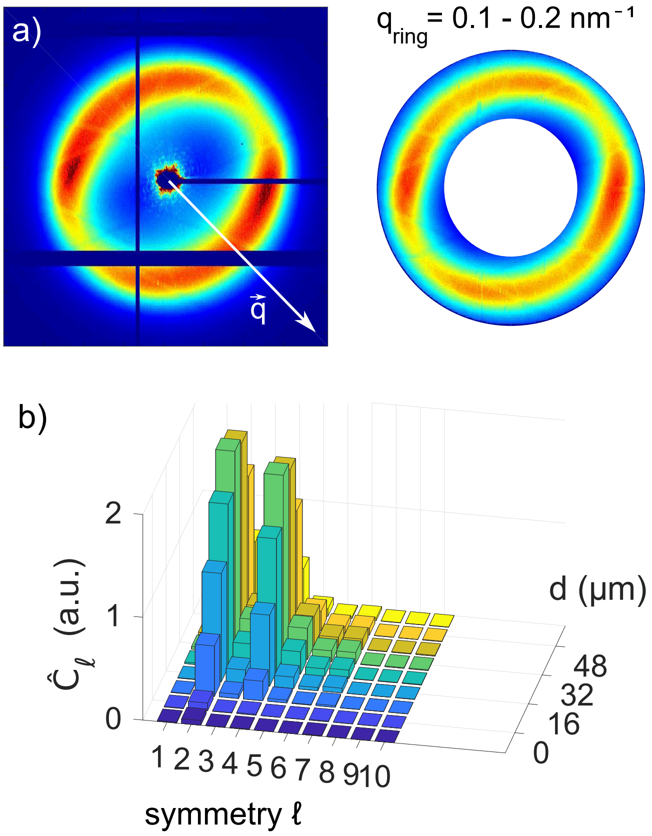

Figure 5.5: a) Diffraction patterns of the Ludox sample and Δq cut containing the first intensity maximum between $q = 0.1\text{-}0.2\,\mathrm{nm}^{-1}$. Gaps between detector panels (dark stripes) have been filled with intensities obtained from mirrored pixels. b) The Fourier coefficients $\hat{C}_\ell$ from XCCA for symmetries ℓ =1-10 are shown for $d > 0$ of the same jet described in Fig. 5.4.

The shift in intensity over φ can be quantified with X-ray cross-correlation analysis (XCCA). In order to apply the technique as described in chapter 3.3, the diffraction patterns were analyzed at q-values between $0.1\text{-}0.2\,\mathrm{nm}^{-1}$ (Ludox) and $0.02\text{-}0.04\,\mathrm{nm}^{-1}$ (sample L), the positions of the structure factor peaks. Furthermore, gaps in the scattering patterns which were due to the gaps in between detector panels have been filled with intensities obtained from mirrored pixels. An example of the calculated Fourier coefficients for symmetries ℓ =1-10 for a jet profile including symmetric as well as asymmetric patterns is shown in Fig. 5.5 for $d \geq 0$. Two-fold and four-fold symmetries dominate the jet at $d > 0$ while in the jet center at $d = 0$ the symmetric diffraction pattern yields $\hat{C}_\ell \approx 0$ for all symmetries $\ell \geq 1$.

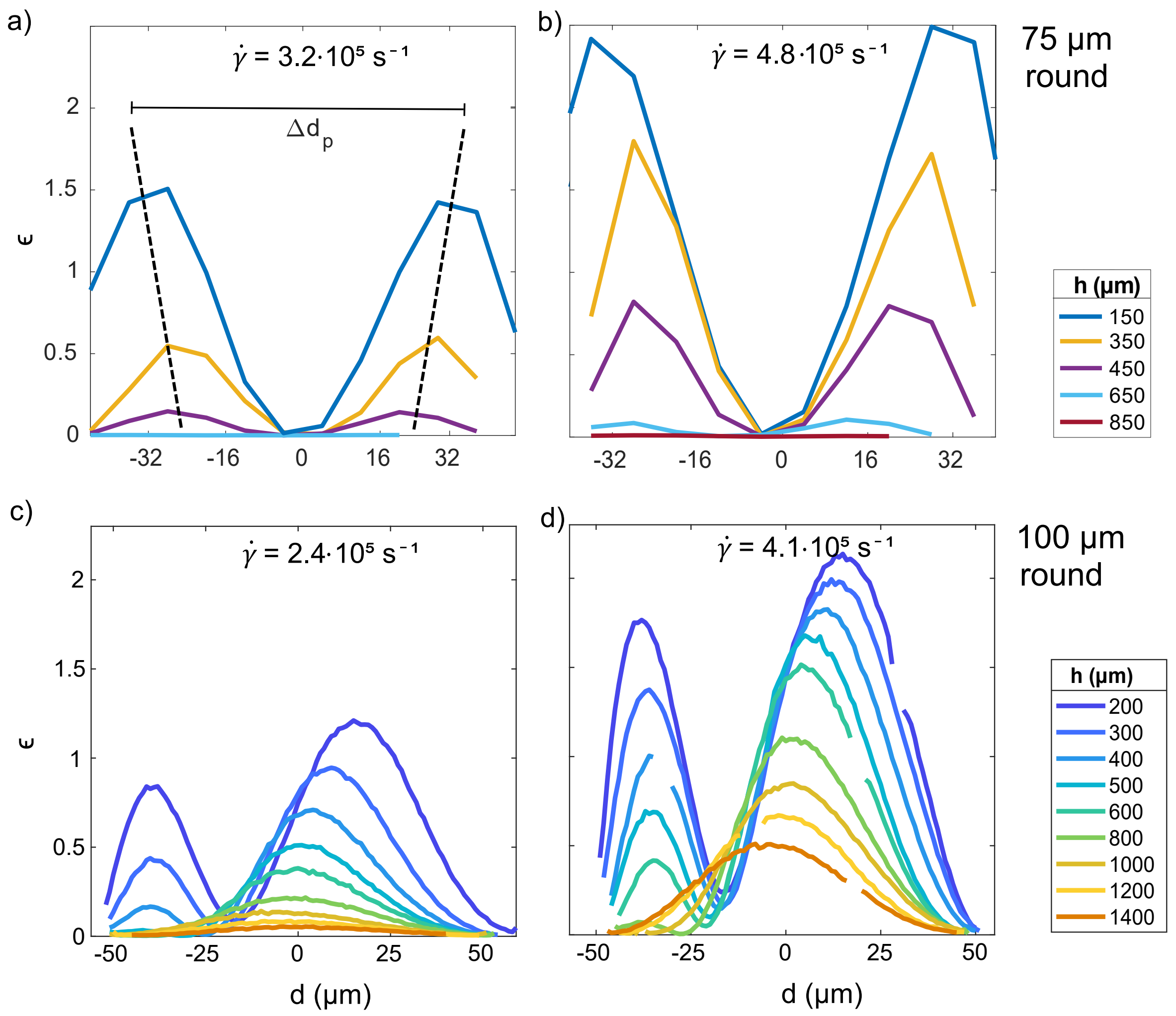

Figure 5.6: Asymmetry quantifying parameter $\varepsilon = \hat{C}_{\ell=2} + \hat{C}_{\ell=4}$ over the nozzle profile d for a) and b) 75 μm jet diamater, c) and d) 100 μm jet diameter from a round tube. Each jet size is shown at two shear rates $\dot{\gamma}$ between $2.4 \cdot 10^5\,\mathrm{s}^{-1}$ and $4.8 \cdot 10^5\,\mathrm{s}^{-1}$ for the Ludox sample.

By adding the contributions for $\ell = 2$ and $\ell = 4$ the intensity anisotropy over φ was quantified by:

$$\varepsilon = \hat{C}_{\ell=2} + \hat{C}_{\ell=4}. \tag{5.1}$$

The results for all nozzle sizes at two different shear rates are shown in Fig. 5.6 a-d and Fig. 5.7 a-d for the Ludox sample. In the jet center ε drops down to 0. On the interface between liquid jet and air the curvature of the jet caused streaks in the scattering pattern, so the data at the exact jet edge was not considered here. The shape of the ε-profile appears to be symmetric. A small difference between the $\pm d$ sides may originate from defects in the mechanical cut of the nozzle tip.

For an increasing distance from the nozzle tip the asymmetry of intensity in the scattering

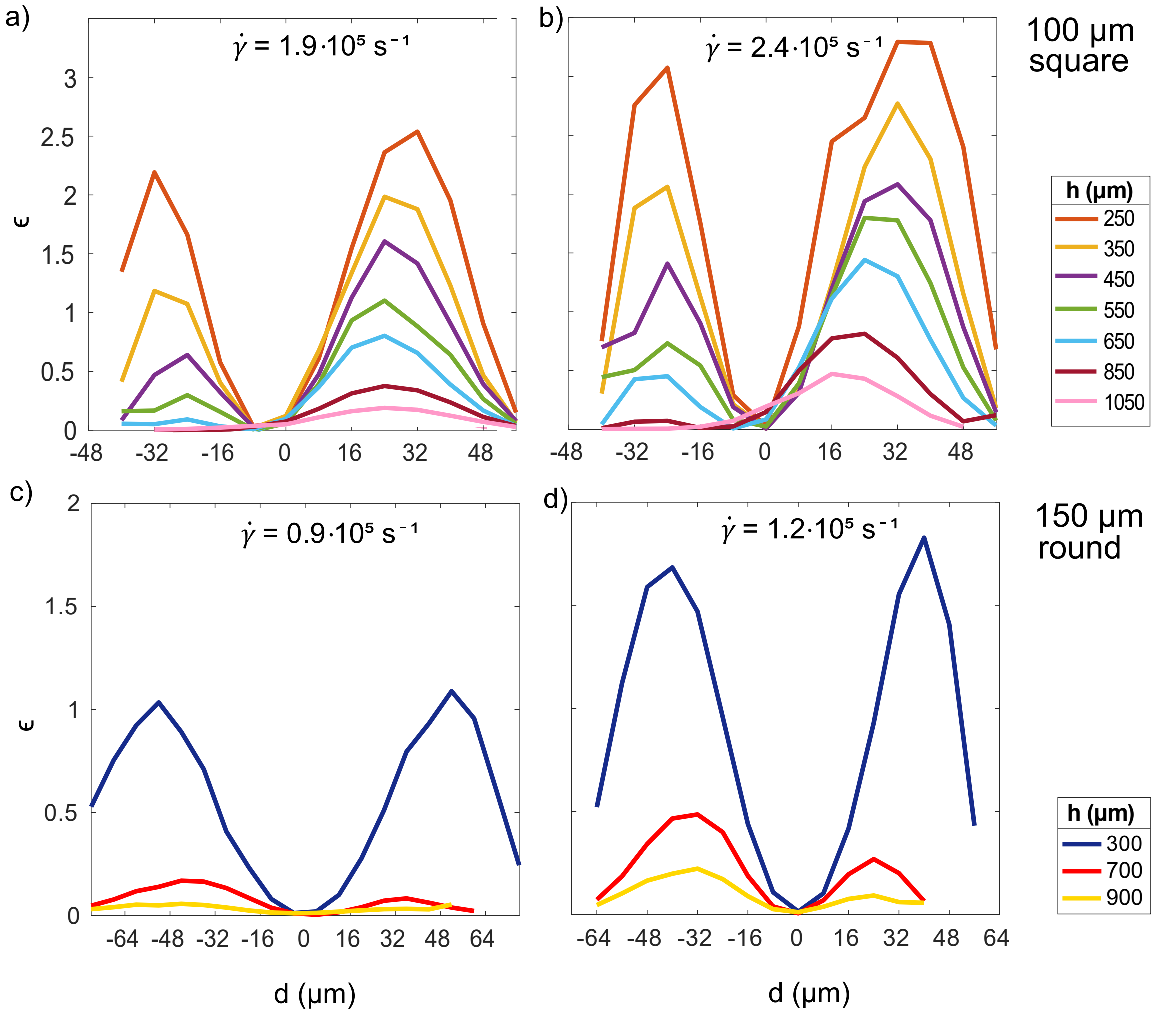

Figure 5.7: Asymmetry quantifying parameter $\varepsilon = \hat{C}_{\ell=2} + \hat{C}_{\ell=4}$ over the nozzle profile d for a) and b) a $100\,\mu$m square tube, c) and d) a $150\,\mu$m round tube. Each jet size is shown at two shear rates $\dot{\gamma}$ between $0.9 \cdot 10^5\,\mathrm{s}^{-1}$ and $2.4 \cdot 10^5\,\mathrm{s}^{-1}$ for the Ludox sample.

patterns decreases until leveling out at $\varepsilon = 0$ after $h \approx$1-2 mm (Ludox sample) and $h \geq 3$ mm (sample L). Higher shear rates $\dot{\gamma}$ lead to stronger asymmetries at comparable nozzle distances and extend to larger distances until leveling out towards $\varepsilon = 0$.

A comparison between the $100\,\mu$m square and round nozzle reveals a three times higher anisotropy ε for the square nozzle at $\dot{\gamma} = 2.4 \cdot 10^5\,\mathrm{s}^{-1}$ (Fig. 5.6 c and Fig. 5.7 b). The differences imply variances in the formation of shear-induced ordering depending on the tube geometry. The discrepancy in jet velocity for round and square jets of similar size and shear rate are about 10% and may contribute to the differences in ε as well.

The asymmetry of the scattering patterns determined by XCCA relates a direction-dependent intensity to a φ-dependent particle ordering. According to Fig. 5.6 the occurrence of strong particle ordering is limited to a shell of the jet between the center and the edges. Moreover,

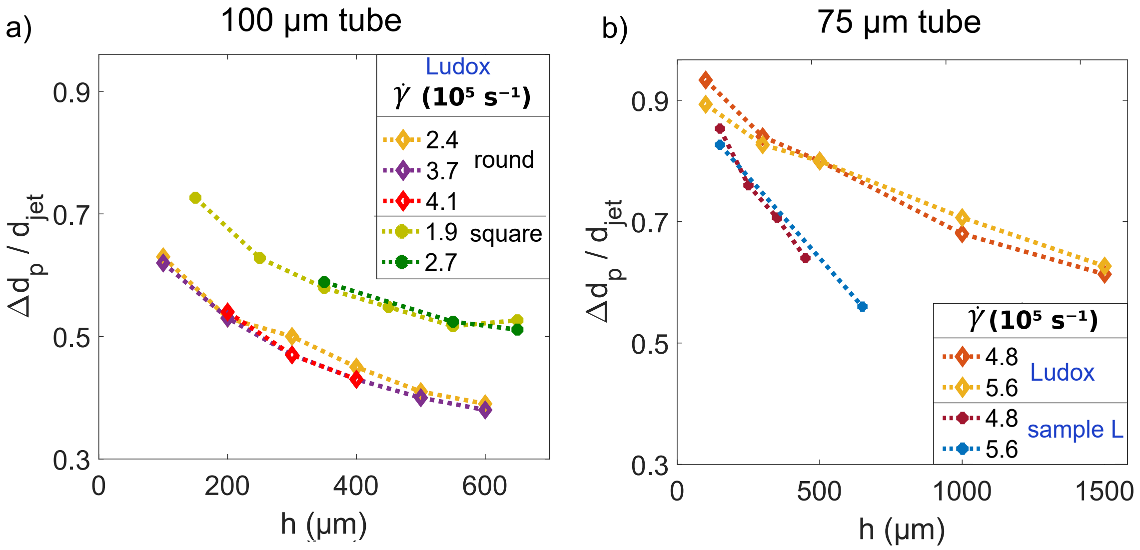

Figure 5.8: a) Distance Δd_p between maxima of $\varepsilon(d)$ normalized on the jet diameter d_{jet} as a function of h for a round and a square tube (100 μm jet). b) $\Delta d_p/d_{jet}$ over h is shown for the Ludox sample and sample L (75 μm jet).

positions of the maxima of ε are not constant over h. Fig. 5.8 shows the distance $\Delta d/d_{jet}$ between the maximum ε for $d < 0$ and $d > 0$ as a function of the distance from the nozzle tip. Both the 100 μm and the 75 μm jets in Fig. 5.8 show a decreasing Δd. For a round and a square 100 μm nozzle (Fig. 5.8 a) the position of the maximum of ε varies between $d_p/d_{jet} = \pm 0.38r$ and $d_p/d_{jet} = \pm 0.73r$ with similar decays over h, displaying the dependence of the structure formation in the jet on the geometry. Different sample sizes (Fig. 5.8 b) yield $\Delta d_p/d_{jet}$ =0.55-0.93 with varying decays. This indicates that with increasing h the jet section with ordered particles moves towards the jet center and the degree of ordering observed for samples with larger particle size persists over longer distances as compared to a smaller particle size.

Beyond asymmetries in the intensity represented by the peak height $S(q_0) = S_0 = \max(S(q))$ of the structure factor peak it is found that also the position of q_0 (see Fig. 5.9 a) shows a distinct φ-dependence. In the jet center at $d = 0$ the first intensity maximum in the diffraction pattern appears isotropic, which is characteristic for 'amorphous' particle ordering.

The dependence of the q_0-positions as a function of the azimuthal angle in the Ludox sample is shown in Fig. 5.9 b. With the rescaled mean spherical approximation (RMSA, see chapter 3.2.2) the effective sample concentration c has been analyzed over an interval of $\Delta\varphi = 5°$ for the case of maximum anisotropy at max $(\varepsilon_{\max(h)})$ with the 100 μm square tube. For the fit of the RMSA a permittivity of the solvent of ε_r=80 was assumed. The charge per particle has been fitted to 30e$^-$ for the unsheared system. For an average sample concentration of 20 vol% (see chapter 4) the shape asymmetry amounts to a $\Delta c \approx$10 vol%. Thus, a φ-dependent variation of $\pm$5 vol%

was observed. The model does not show a decrease of Δc to 0 for $d = 0$, which might be due to the resolution or the limitations of the RMSA itself. Furthermore, RMSA models the charge-stabilized silica particles effectively, however, the addition of shear forces is not considered and may explain the larger effective c here.

The q_0-dependence on φ for the case of an asymmetric diffraction pattern is shown in Fig. 5.9 c for Ludox and in Fig. 5.9 d for sample L. Regions of no apparent structure factor peak in sample L are marked in gray. Noticeable is the difference in amplitude for the oscillation between both samples, which amounted to 2.5% for Ludox and 15% for the larger sample L in relation to their respective q_0-values. In order to quantify the change in q_0 for the Ludox sample, the variance var(q_0) with respect to φ for different d is shown in Fig. 5.9 e. Towards the jet center and edge the shape asymmetry decreases and var(q_0) becomes 0. Both appearance and disappearance of the shape asymmetry in the jet profile d behave very similar to the observed intensity asymmetry ε. In Fig. 5.9 f ε is shown as a function of var(q_0) for the Ludox sample. The linear fit for the data has an offset of $b = 1$ with a slope of 1.96 ± 0.08. Although ε and var(q_0) show similar behavior as a function of d, they represent different aspects of the sample system. The intensity asymmetry signifies different direction-dependent degrees of order in the system. The shape asymmetry denotes a φ-dependence of interparticle distances. Shear forces seem to influence both local order and packing density.

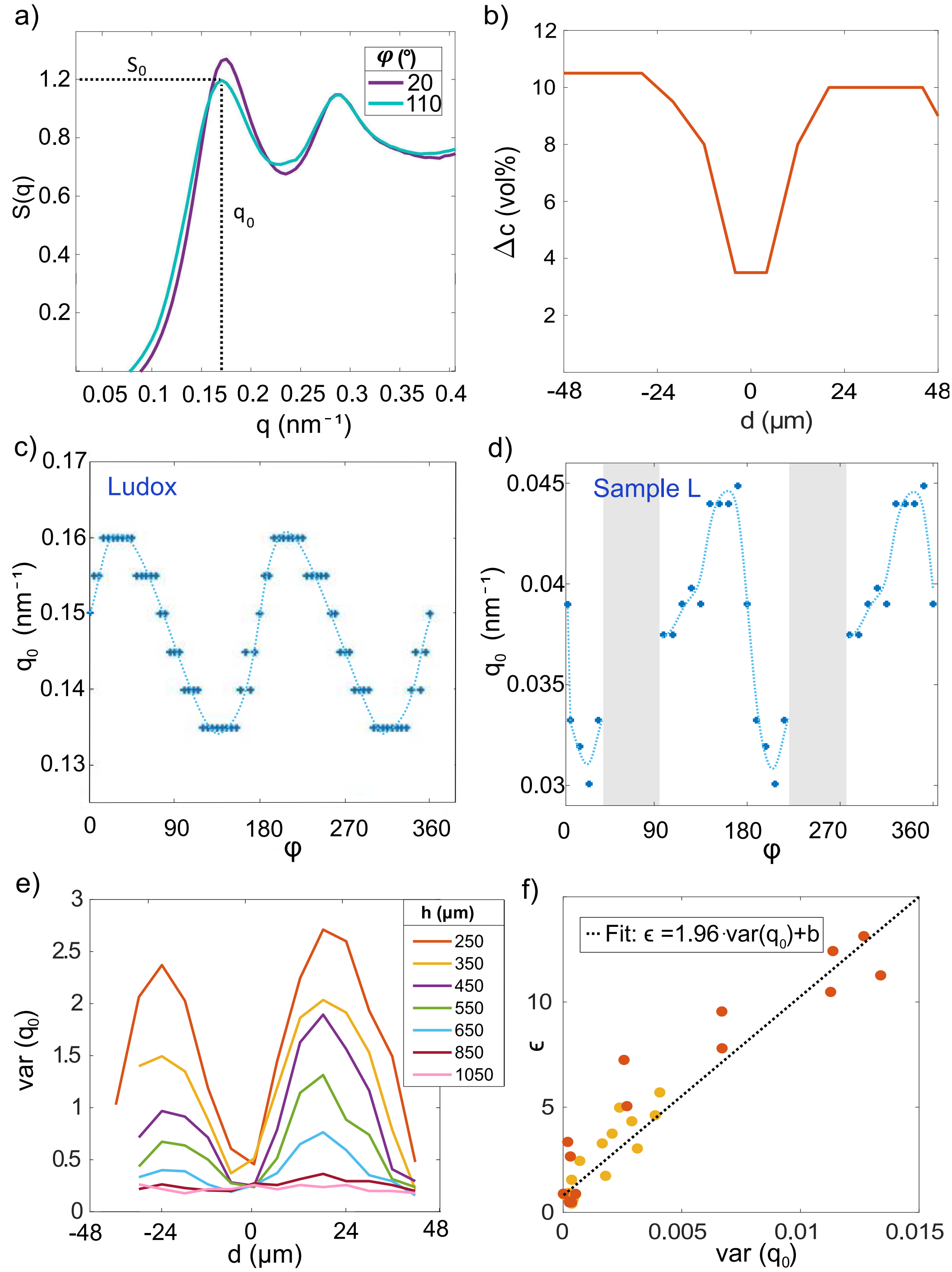

Figure 5.9: a) The q_0 position of the structure factor peak $\max(S(q)) = S_0$ varies at different azimuthal angles φ. b) The effective concentration difference Δc over d for $q = 0.1$-$0.2\,\mathrm{nm}^{-1}$ was calculated from RMSA for the Ludox sample at $d = -24\,\mu\mathrm{m}$ with the $100\,\mu\mathrm{m}$ square nozzle, $Q = 1600\mu\mathrm{l/min}$ at $h = 250\,\mathrm{mm}$ nozzle distance. c) q_0 over φ from measurements on Ludox, d) q_0 over φ from measurements from sample L. In the gray regions no structure factor peak was observed. e) The variation in q_0 over the whole q-ring for the Ludox sample is plotted over the jet profile d. f) The asymmetry quantifying parameter ε as a function of the shape asymmetry expressed by the variation in q_0 for the Ludox sample (see b), c) and e)) with a linear fit.

5.4 Decay after shear cessation

In the following section the decay of the intensity asymmetry as well as the shape asymmetry along the jet axis h are discussed. As shown in Fig. 5.6 and Fig. 5.9 e the highest ε and var(q_0) was observed at low h close to the nozzle tip. In order to quantify the degree of the decay, the parameter $\xi_\varepsilon = \max(\varepsilon(h))$ is defined.

When ξ_ε is studied over h (see Fig. 5.10 a) a fast exponential decay for low shear rates has been observed. With increasing shear rate the exponential decay slows down. By taking the jet velocities v_{jet} into account, the h-axis can be converted into a time via $t = h/v_{jet}$ and the exponential decay lines shift closer together. Here the jet velocities were calculated for round[112] and square[113] nozzles via the shear rate and jet diameter d$_{jet}$ or inner edge length W (cf. equation 2.7):

$$v_{jet,round} = \frac{\dot{\gamma} \cdot d_{jet}}{8}, \tag{5.2}$$

$$v_{jet,square} = \frac{\dot{\gamma} \cdot W}{7.1136}. \tag{5.3}$$

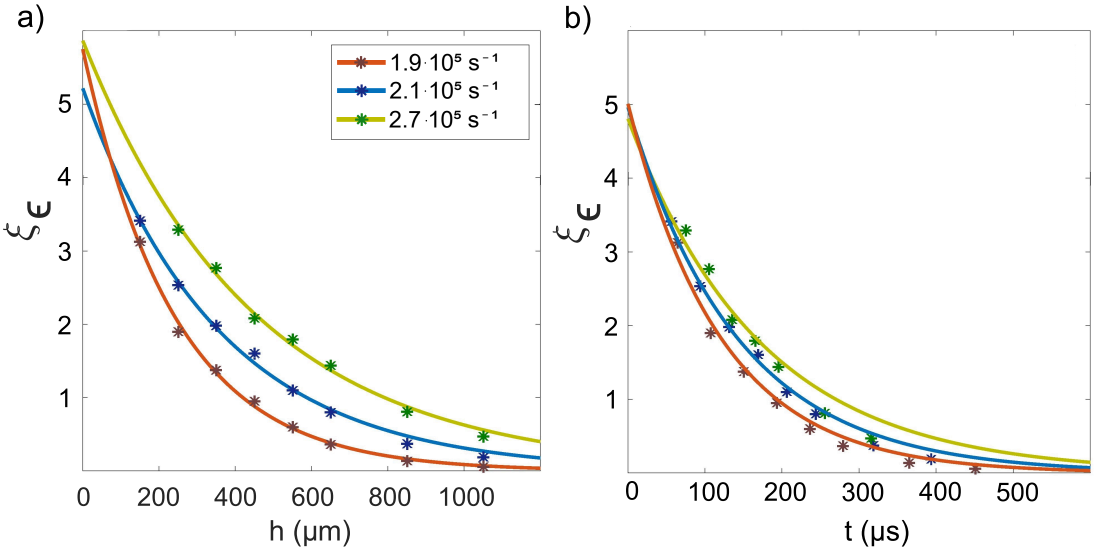

Figure 5.10: a) The maximum of the intensity asymmetry ξ_ε for Ludox as a function of the distance h from the nozzle tip. Shown are the results for three different shear rates $\dot{\gamma}$ measured with the 100 μm square jet. b) Decay ξ_ε over time t for the same three data sets as in a).

From the exponential fit $\xi_\varepsilon(t) = a \cdot \exp(-\frac{t}{\tau_\varepsilon})$ characteristic decay times τ_ε were calculated for all different nozzle sizes at various shear rates. The results are summarized in Tab. 5.1 and Tab. 5.2. In Fig. 5.11 ξ_ε over t is shown for Ludox and for sample L in a shear rate range between $1.9 \cdot 10^5$ and $5.6 \cdot 10^5\,\mathrm{s}^{-1}$.

sample	Ludox						
tube size	d=150 μm	d=75 μm			$W = d_{square}$ =100 μm		
$\dot{\gamma}(10^5\,\mathrm{s}^{-1})$	0.9	3.2	4.8	5.6	1.7	1.9	2.4
τ_ε (μs) for ξ_ε	122 ± 19	47 ± 16	34 ± 31	25 ± 7	172 ± 58	120 ± 21	142 ± 18

Ludox					
d=100 μm					
2.4	2.7	3.1	3.4	3.7	4.1
145 ± 27	153 ± 28	157 ± 27	166 ± 25	177 ± 26	187 ± 29

Table 5.1: Characteristic times of the decay τ_ε in μs for ξ_ε for the Ludox sample.

sample	S	M				L		
tube size	d=75 μm							
$\dot{\gamma}(10^5\,\mathrm{s}^{-1})$	5.6	3.2	4.0	4.8	5.6	3.2	4.8	5.6
τ_ε (μs) for ξ_ε	495 ± 130	218 ± 112	267 ± 55	338 ± 94	432 ± 142	410 ± 104	247 ± 100	215 ± 53

Table 5.2: Characteristic times of the decay τ_ε in μs for ξ_ε for sample S, M and L ($d = 75\,\mu$m round nozzle).

In Fig. 5.12 a the characteristic decay times for ξ_ε from Tab. 5.1 are additionally plotted as a function of the shear rate. Over the whole range of $\dot{\gamma}$ the characteristic decay times τ stay in the range of 30-500 μs. At the highest shear rate of $\dot{\gamma} = 5.6 \cdot 10^5\,\mathrm{s}^{-1}$ the differences in particle size for sample S, M and L lead to τ-values of 495 μs, 432 μs and 215 μs. From theoretical studies[15,114] a non-linear behavior for characteristic decay times as a function of the Péclet number Pe has been predicted for a sufficiently high impact of shear stress on colloidal suspensions (cf. equation 2.13). Generally, hard spheres show a transition between Brownian motion dominated and shear-dominated dynamics[115] at $Pe \approx 1$. In order to incorporate the particle size into the time of shear cessation, $Pe^2\tau_\varepsilon$ was plotted as a function of Pe in Fig. 5.12 b. The data points for the Ludox sample from the 75 μm round, 100 μm square and 150 μm round nozzle have been measured during the first measurement campaign. A transition from a linear to a constant behavior as discussed on the basis of the first campaign data[104] could not be confirmed during the second campaign with measurements at higher Pe numbers. The deviation of the data from the 75 μm round nozzle (blue) from the others may originate from a slip in the nozzle position during the measurement. Disregarding the 75 μm round nozzle data, the decay times $Pe^2\tau_\varepsilon$ rise according to a power law Pe^n with $n = 2.14 \pm 0.07$. Thus, τ_ε shows a rather weak, but non-constant dependence on Pe as $\tau_\varepsilon \propto Pe^{0.14}$. Therefore, the characteristic times τ are dependent on the interdependent parameters shear rate, viscosity and hydrodynamic particle radius. In general, the application of high shear rates causes a stronger asymmetry, but the decay time of that asymmetry does not rise constantly with the shear rate in fast flowing jets. The occurrence of shear-induced order in liquid jets is furthermore limited to a finite nozzle distance h for high jet velocities (and thus high Pe numbers) due to the transition into turbulent flow.

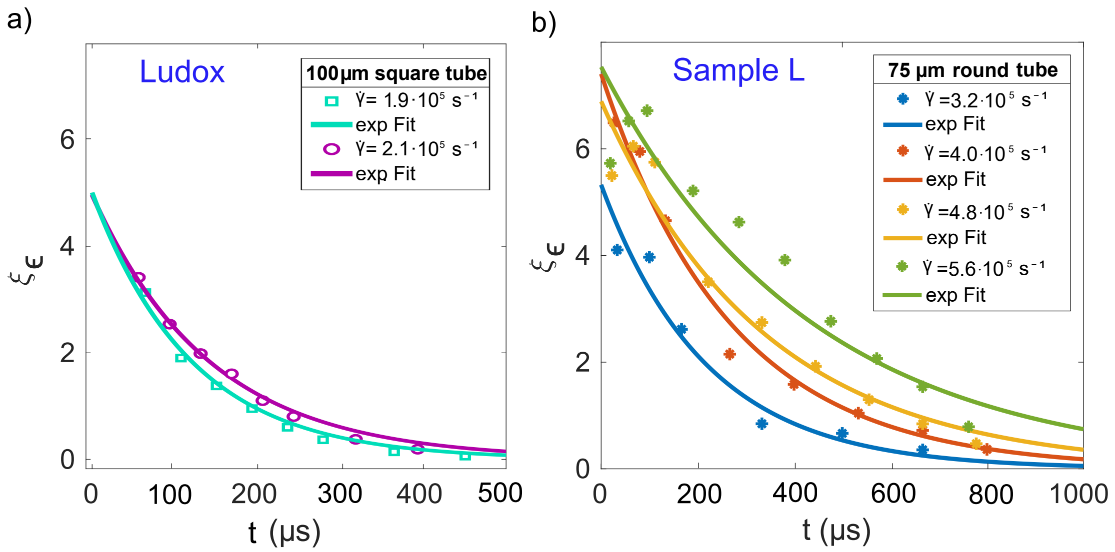

Figure 5.11: The intensity asymmetry ξ_ε as a function of the distance h a) for the Ludox sample from the 100 μm square nozzle and b) for sample L from the 75 μm round nozzle.

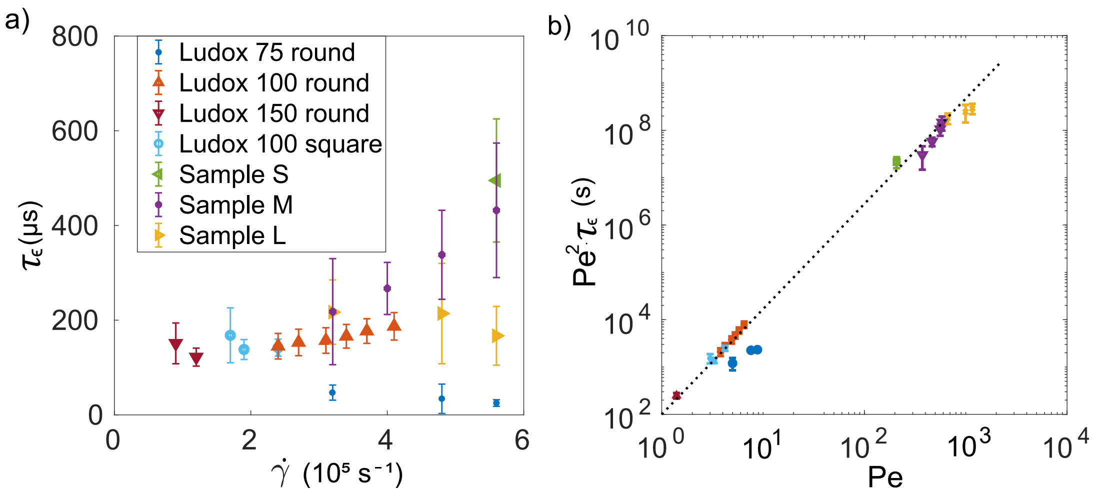

Figure 5.12: a) The characteristic decay time τ_ε from the exponential fit of ξ_ε for Ludox ($r = 15$ nm) and samples S ($r = 43$ nm), M ($r = 63$ nm) and L ($r = 77$ nm). Data for the Ludox sample was taken with 75 μm (blue), 100 μm (orange) and 150 μm (red) round tubes as well as the 100 μm square tube (light blue). b) Characteristic times τ_ε (see Tab.5.1 and Tab.5.2) were weighted with the square of the Péclet number Pe^2 and are shown as a function of Pe. The data points collapse on a straight line.

Chapter 6

Charge-stabilized silica particles under the influence of salt

In this chapter the influence of the changing electro-static potential on the shear-induced structure of particles in a liquid jet was studied by the addition of salt into a colloidal silica suspension. Experiments were performed with the monovalent KCl and the bivalent $MgCl_2$.

The RMSA analysis of the Ludox sample showed a charge of $30 \pm 10e^-$ per particle for the unsheared system. The salt screens charge-stabilized particles from each other and changes the colloidal silica into a more hard sphere like system. In order to investigate this screening effect, salt solutions of 50-750 μMol/l KCl were added to this slightly charged system and measured with shear rates between $\dot{\gamma} = 2.4 \cdot 10^5\,s^{-1}$ and $\dot{\gamma} = 4.1 \cdot 10^5\,s^{-1}$. Fig. 6.1 a-d shows the results of ε as a function of d for the highest salt concentration in comparison with the unaltered system at two different shear rates. The data was analyzed analogously to the one in chapter 5.3. The asymmetry quantifying parameter ε was evaluated at $d \geq 0$, as the higher ε-values were assumed to be less influenced by irregularities in the nozzle. A slight decrease in ε could be observed for the system with 750 μMol/l KCl.

Fig. 6.1 e shows the decay times τ_ε for all salt concentrations. At 150 μMol/l and above the decay times starts to decrease. It was reduced from $186 \pm 29\,\mu s$ for the pure solution to $126 \pm 31\,\mu s$ at 750 μMol/l.

The decrease in τ_ε causes no change in the exponent n as shown in Fig. 6.1 f. Here, $Pe^2 \tau_\varepsilon$ is plotted as a function of Pe at salt concentrations of 150-750 μMol/l together with the results from the pure sample. Further studies at different Pe-values and with higher salt concentrations are needed in order to determine an eventually salt-dependent value of the exponent n.

The findings are that shear-induced ordering is not prevented by tuning the electro-static forces in the studied regime. The observed reduction of characteristic decay times at salt concentra-

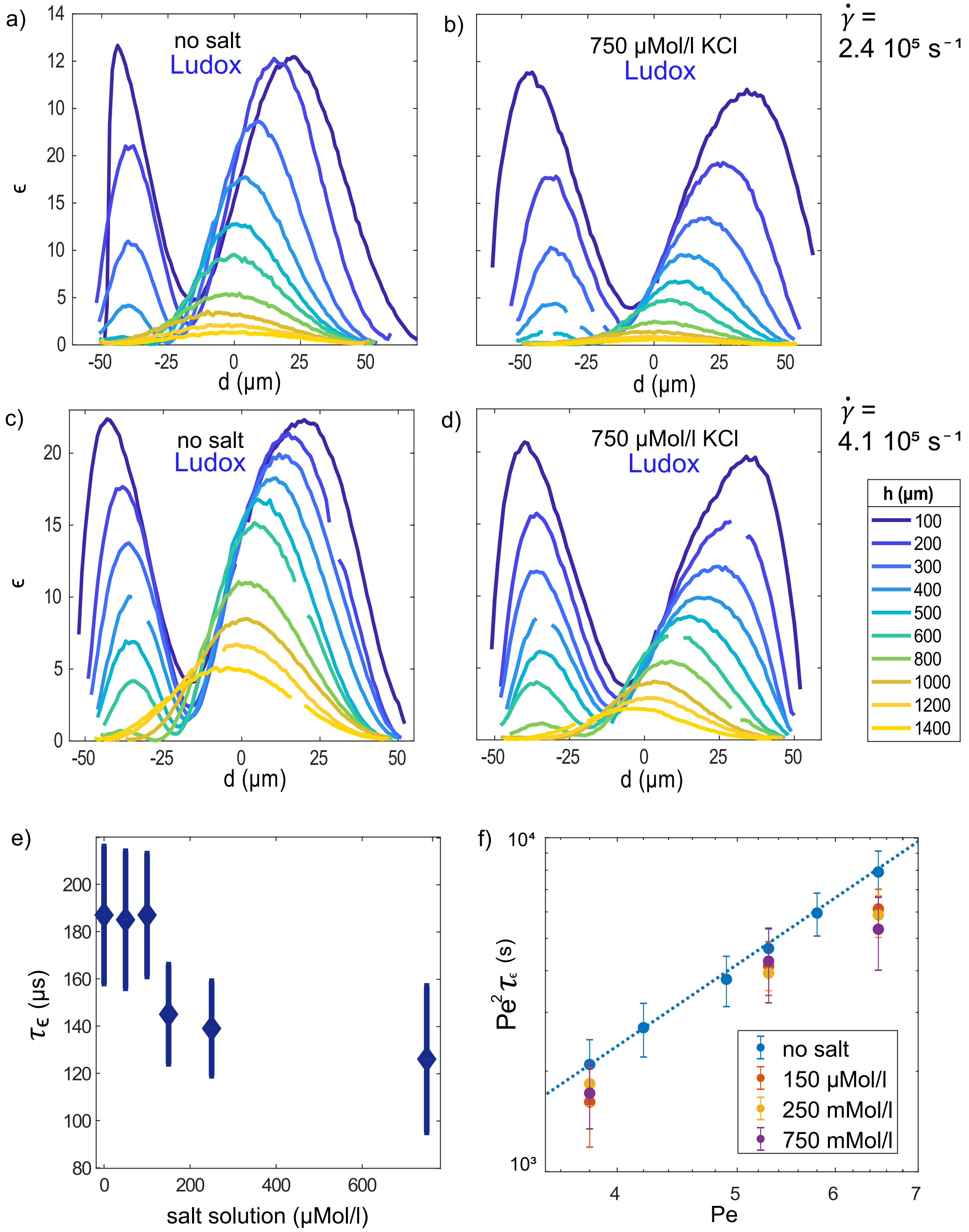

Figure 6.1: Asymmetry quantifying parameter $\varepsilon = \hat{C}_{\ell=2} + \hat{C}_{\ell=4}$ as a function of d for the Ludox sample without KCl (a) and with $750\,\mu$Mol/l KCl (b) at $\dot{\gamma} = 2.4 \cdot 10^5\,\mathrm{s}^{-1}$ and for $\dot{\gamma} = 4.1 \cdot 10^5\,\mathrm{s}^{-1}$ (c)(d). Measurements were performed with the $100\,\mu$m round nozzle. e) Decay times τ_ε for the Ludox sample at $\dot{\gamma} = 4.1 \cdot 10^5\,\mathrm{s}^{-1}$ for different concentration of KCl. f) Characteristic times $Pe^2\tau_\varepsilon$ as a function of Pe for different salt concentrations. Data from the pure solution (no salt) and the corresponding fit from Fig. 5.12 b is shown in blue.

tions $\geq 150\,\mu\mathrm{Mol/l}$ indicates a reduction of the charge stabilization in the system. It is noteworthy that the Ludox TMA sample contained a proportion of 0.0015-0.06% of $C_8H_9ClN_2O_2S_2$ stabilizing co-solvent, which may have reduced the impact of salt on the colloidal system.

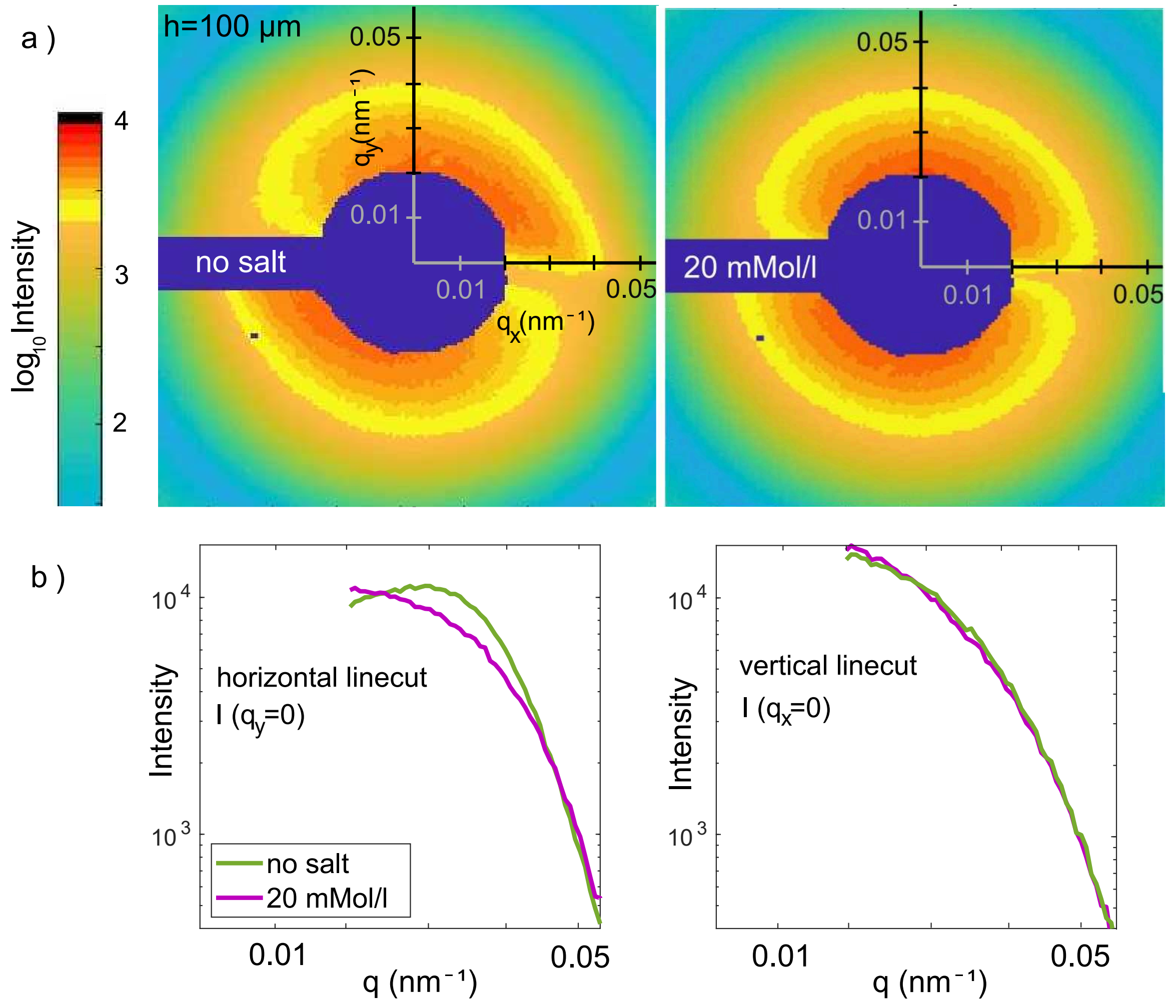

Figure 6.2: a) Diffraction patterns for sample L for $q = 0\text{-}0.057\,\mathrm{nm}^{-1}$ at $h = 100\,\mu\mathrm{m}$ with 0 and $20\,\mathrm{mMol/l}$ salt. Measurements were performed with the $75\,\mu\mathrm{m}$ round nozzle at $\dot{\gamma} = 5.6 \cdot 10^5\,\mathrm{s}^{-1}$ for $d = -35\,\mu\mathrm{m}$. b) Horizontal and vertical linecuts through the center of the diffraction patterns in a).

Samples S, M and L are stronger charge-stabilized systems compared to the Ludox sample. The charge per particle of the larger spheres is up to two times higher ($52\pm5\mathrm{e}^-$ for sample S, $81\pm5\mathrm{e}^-$ for sample L). They could be concentrated to a lesser degree due to the lack of stabilizing co-solvents.

Fig. 6.2 a shows two exemplary scattering pattern for the pure solution of sample L and at a salt concentration of $20\,\mathrm{mMol/l}$ KCl. The linecuts $I(q_x = 0)$ and $I(q_y = 0)$ in Fig. 6.2 b indicate a slight reduction of anisotropy for $I(q_y = 0)$ caused by the addition of salt. For an elaboration of this trend the ε of sample L was analyzed at different KCl concentrations (Fig. 6.3). Up to a salt concentration of $1300\,\mu\mathrm{Mol/l}$ the system does not change significantly and the order pa-

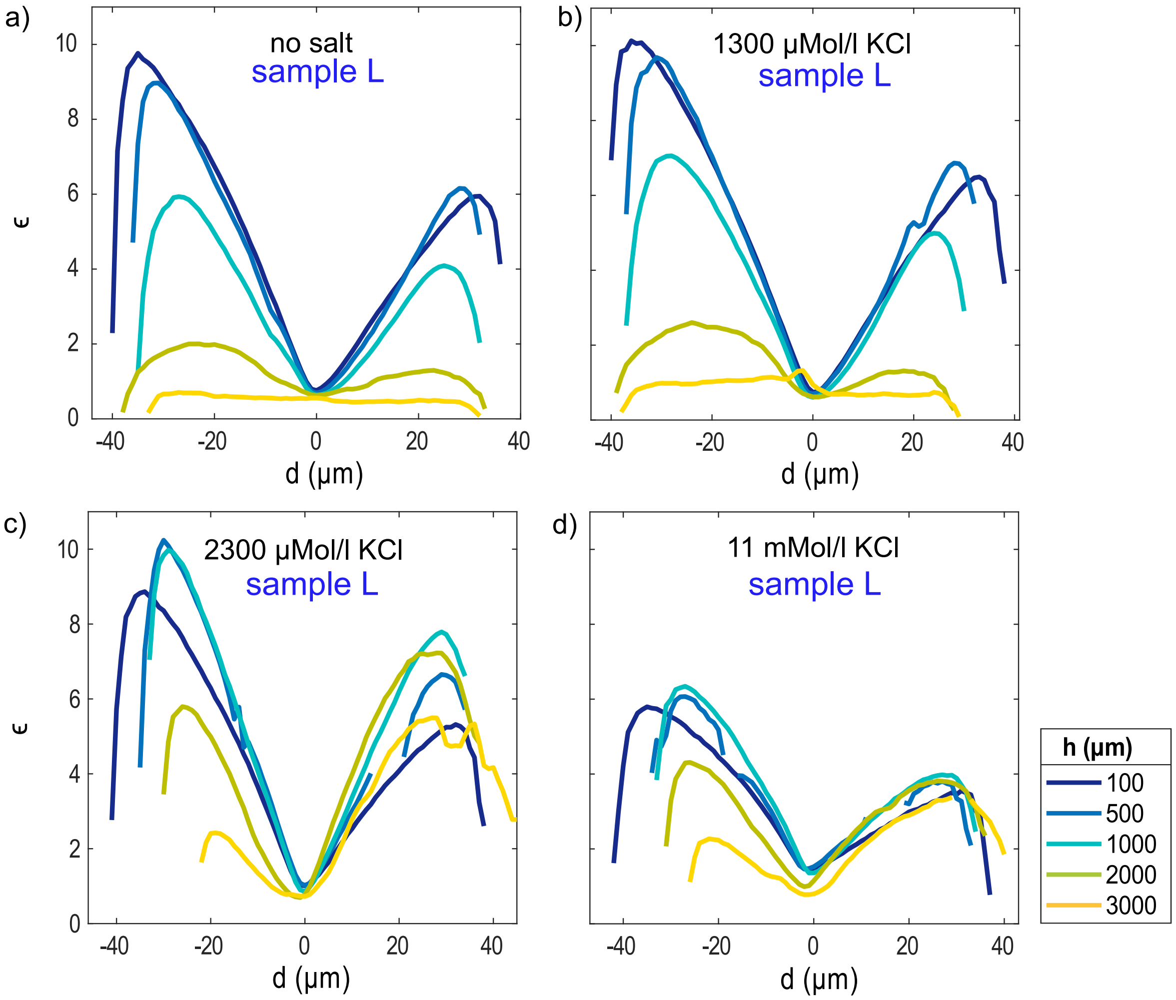

Figure 6.3: Plotted is the asymmetry quantifying parameter $\varepsilon = \hat{C}_{\ell=2} + \hat{C}_{\ell=4}$ over the nozzle profile d for sample L with a) no salt, b) $1300\,\mu\mathrm{Mol/l}$, c) $2300\,\mu\mathrm{Mol/l}$ and d) $11\,\mathrm{mMol/}$ KCl. Measurements were performed with the $75\,\mu$m round nozzle at $\dot{\gamma} = 5.6 \cdot 10^5\,\mathrm{s}^{-1}$.

rameter ε decreases to ≈ 0 for nozzle distances $h = 3000\,\mu$m. With $2300\,\mu\mathrm{Mol/l}$ (Fig. 6.3 c) the behavior of ε starts to change. At a salt concentration of $11\,\mathrm{mMol/l}$ (Fig. 6.3 d) the curve shape of ε has dropped for $h = 100\,\mu$m by $\approx 50\%$ compared to the system without salt. The ordering throughout the jet profile d appears to become more similar for all measured nozzle distances and the expected decreases in ε to ≈ 0 for large nozzle distances could not be observed.

A comparable behavior was observed for sample M when $MgCl_2$ was added (Fig. 6.4). The maximum of $\varepsilon(h)$ starts to change at $1200\,\mu\mathrm{Mol/l}$ and at $11\,\mathrm{mMol/l}$ has dropped for $h = 100\,\mu$m by $> 50\%$ compared to the system without salt. The impact of $MgCl_2$ on the colloidal system was seen at lower concentrations compared to KCl, probably because the ionic strength[116] of the bivalent salt is four times higher then for the monovalent salt at the same concentration.

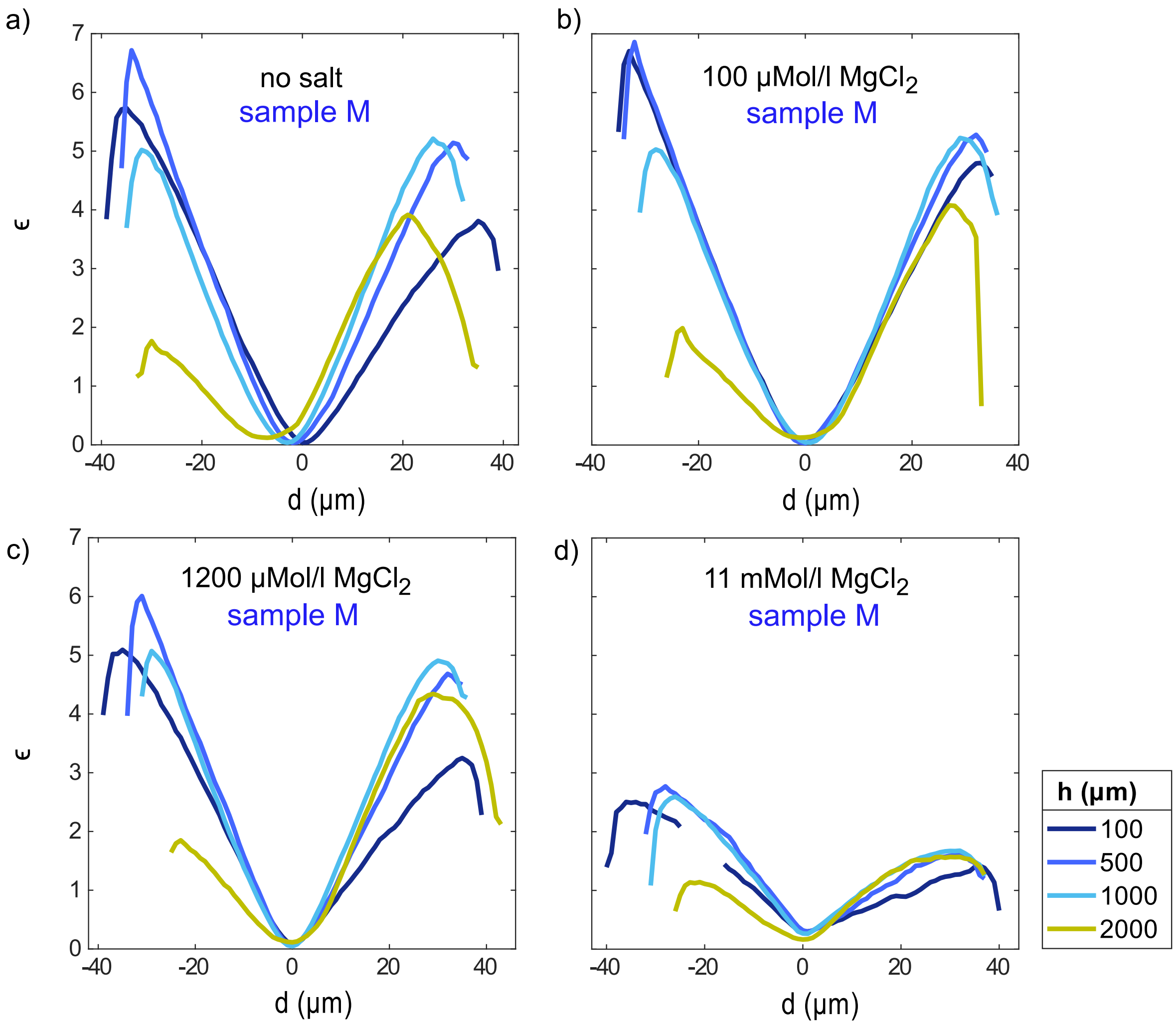

Figure 6.4: ε over the nozzle profile d for sample M with a) no salt, b) $100\,\mu$Mol/l, c) $1200\,\mu$Mol/l and d) 11 mMol/l $MgCl_2$. Measurements were performed with the $75\,\mu$m round nozzle at $\dot{\gamma} = 5.6 \cdot 10^5\,s^{-1}$.

The difference between KCl and $MgCl_2$ is further illustrated in Fig. 6.5. Here, the variation of ε at $d = 100\,\mu$m is shown for sample L and M as a function of all measured salt concentrations of KCl and $MgCl_2$, respectively. Salt concentrations below $1300\,\mu$Mol/l KCL showed no significant impact on the order of system L, while for sample M a decrease in var ε is already present at the lowest concentration of $MgCl_2$ at $100\,\mu$Mol/l. The reduction of var ε appears to be faster with KCl than $MgCl_2$, which is also observed for var ε as a function of h (Fig. 6.5 b).

In general, shear-induced ordering of charge-stabilized particles is sensitive to the change of electro-static forces. An increase in charge per particle of the colloids increases the sensitivity of the system towards co-solvents like KCl or $MgCl_2$, as the salt screens the charge-stabilized particles and creates a more hard-sphere like interaction potential. High salt concentrations result in lower degrees of ordering throughout the jet and also the ionic strength of the dispersion has a strong impact on the behavior of the system.

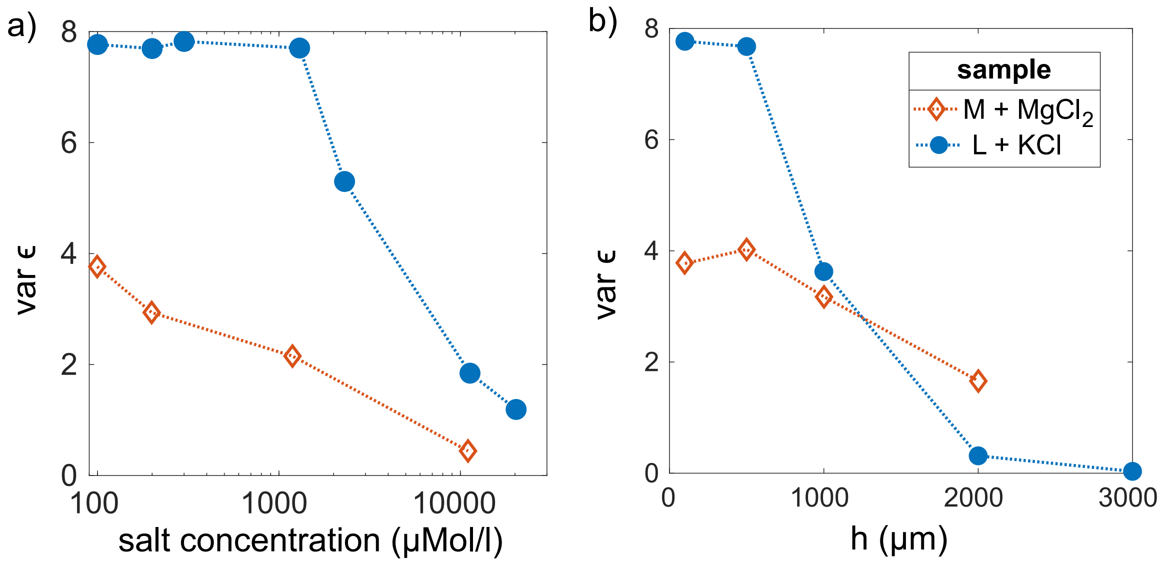

Figure 6.5: a) Variation of ε in d as a function of the salt concentration for sample L with KCl and sample M with $MgCl_2$ at $h = 100\,\mu$m. b) Variation of ε in d as a function of h for $100\,\mu$Mol/l salt concentration. Measurements were performed with the $75\,\mu$m round nozzle at $\dot{\gamma} = 5.6 \cdot 10^5\,s^{-1}$.

Chapter 7

String-like order in liquid micro-jets

The experimental data in chapters 5 and 6 showed jet regions giving rise to asymmetrical scattering. Previous studies[59,117] suggested a non-isotropic microscopic particle arrangement in sheared systems and proposed the formation of string-like order. In order to relate these results to shear in liquid jets, multiple two-dimensional configurations of hard discs in co-flowing string-like order were modeled. Their diffraction patterns were simulated to describe the measured data.

In order to describe the behavior of ε as a function of d (cf. Fig. 5.6, Fig. 5.7) three regions were modeled for a $100\,\mu$m round jet between $h = 100\,\mu$m and $h = 600\,\mu$m. Fig. 7.1 depicts isotropic order in the jet center in dark green and an anisotropic region (light blue) for the maximum ε between about $0.4r$ and $0.65r$ (cf. Fig. 5.8). At the jet edge a region with decreasing anisotropy is marked in blue.

Flow profiles within small pipes of different geometries have been well studied[118,119] and show a maximum flow velocity in the center of the pipes. When the X-rays shine through the center of a liquid jet, no asymmetric diffraction pattern is observed. Note that counteracting structures in the front and the back of the jet might prevent the observation of shear-induced order. Moving out of the jet center increases the relative contribution of the scattering volume of particles which are not ordered parallel to the beam direction. Here, asymmetric structures are observed in diffraction patterns. At the jet edge the structure is compromised by turbulences on the liquid/air interface[120] and diffusion dominates in the outer jet areas of slower flow velocity. Both turbulences and diffusion lead to less anisotropic ordering in the dark blue region in Fig. 7.1. SAXS measurements at the interface area are actually dominated by streaks due to scattering from the jet curvature.

Fig. 7.2 shows the interaction regions between a jet and a $1\,\mu$m wide X-rays beam as a function of the jet radius. Plotted are the chord lengths from a schematic jet as shown in Fig. 7.1 with a dimension of $0.5r$ for the green region and a width of $0.3r$ for the light blue region. In this

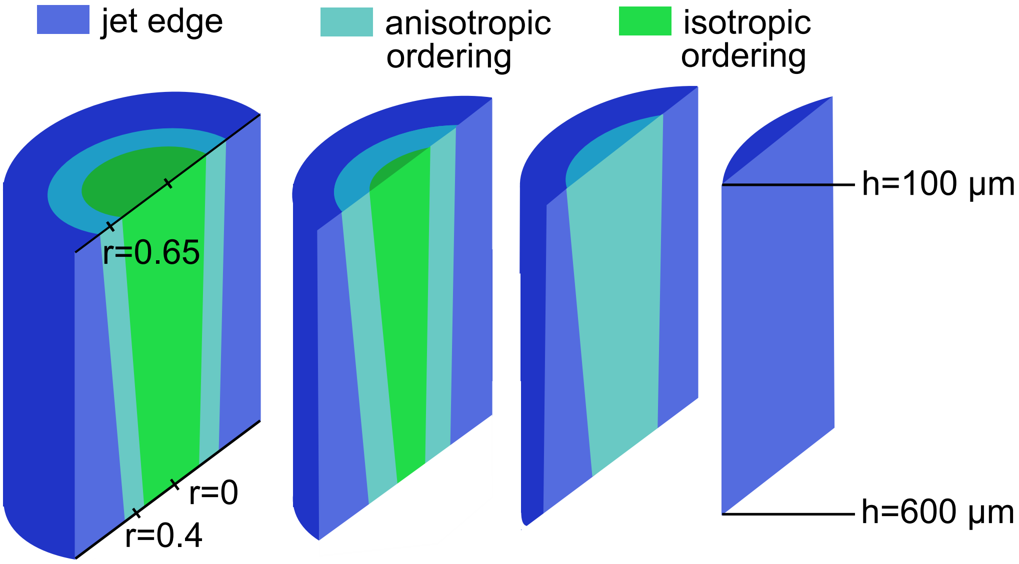

Figure 7.1: Schematics of the proposed sections of a liquid jet. Three regions of different microscopic particle ordering are shown by different colors.

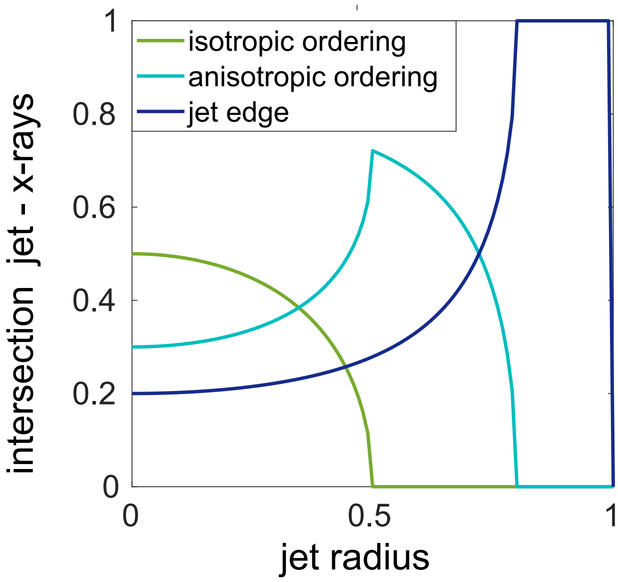

Figure 7.2: Intersection between a schematic jet as shown in Fig. 7.1 with X-rays over the radius of the jet. Assumed are a size of $0.5r$ for the green region and a width of $0.3r$ for the light blue region.

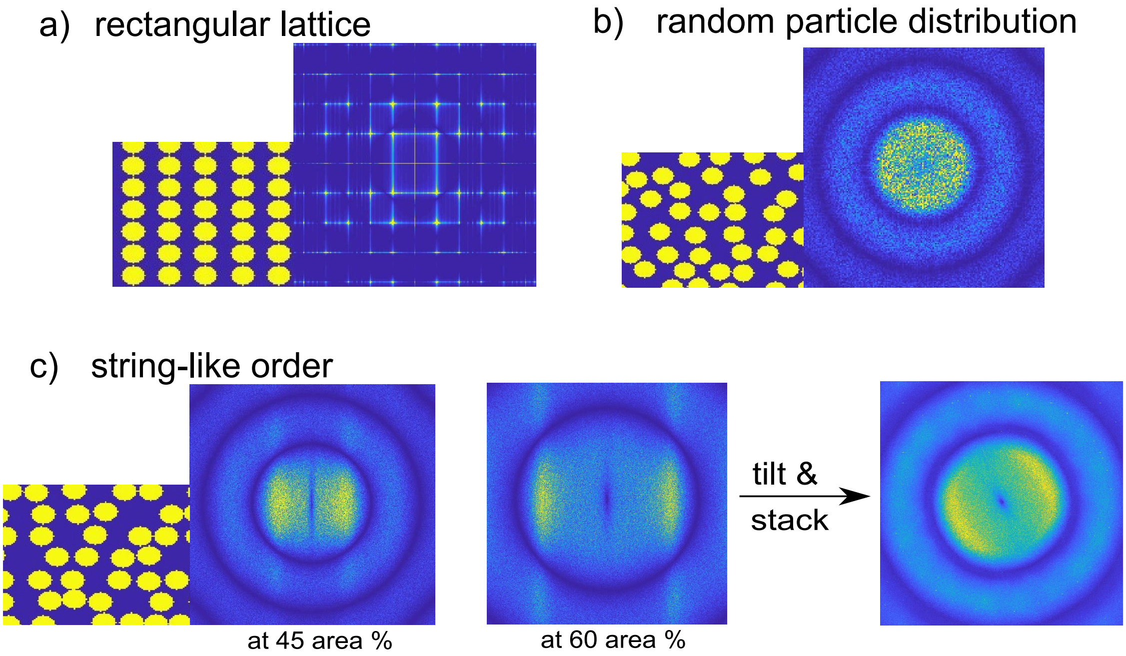

Figure 7.3: Simulated particle arrangements and diffraction patterns. Via FFT the diffraction pattern for a) particles on a rectangular lattice structure (the starting point of the simulation), b) a random distribution of particles, and c) particles distributed in string-like order for 45 area% and 60 area% concentration are shown. By turning and overlaying multiple diffraction patterns from string-like particle distributions, an asymmetric diffraction pattern as observed in the SAXS measurements is obtained.

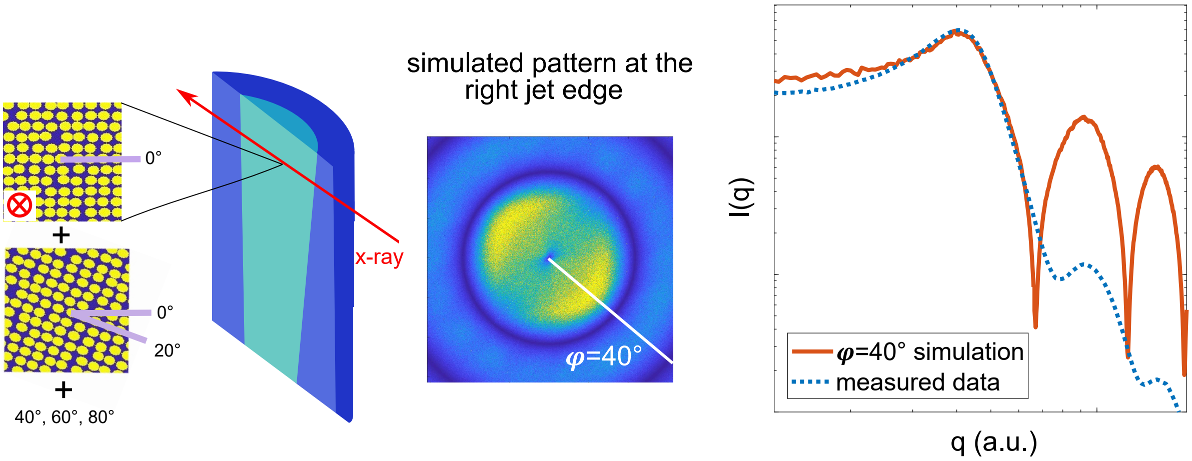

Figure 7.4: Simulated string-like particle distributions (at 50 area %). The simulated diffraction pattern from five string-like particle arrangement tilted between 0° and 80° is shown in the center. A linecut of the simulated pattern at $\varphi = 40^\circ$ is shown in comparison with measured data from the Ludox sample in a $100\,\mu$m round nozzle at $d = 35\,\mu$m and $\dot{\gamma} = 2.4 \cdot 10^5\,\mathrm{s}^{-1}$.

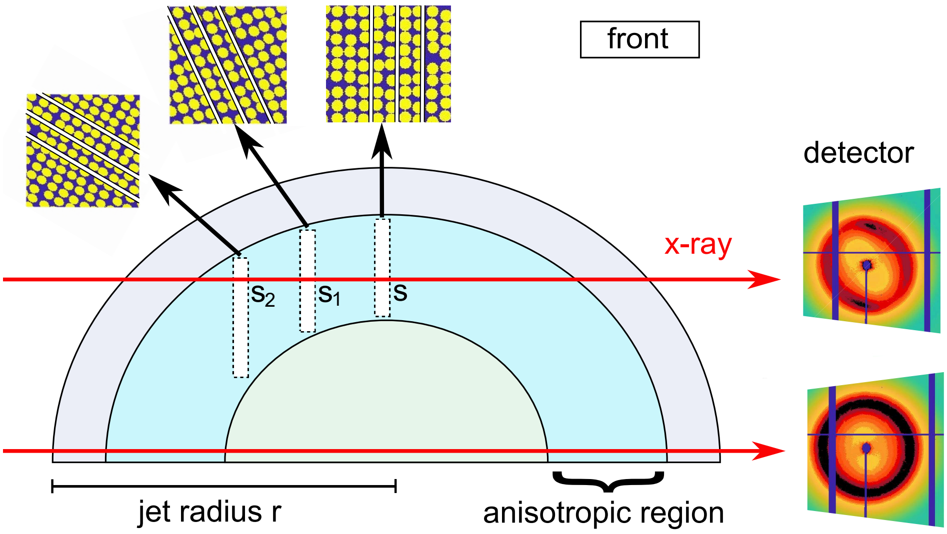

Figure 7.5: Front of the jet with a basic configuration of strings in slice S. At positions S_1 and S_2 the X-ray passes through projections of configuration s, which in the detector is shown as a superposition of scattering from differently tilted string-like structures.

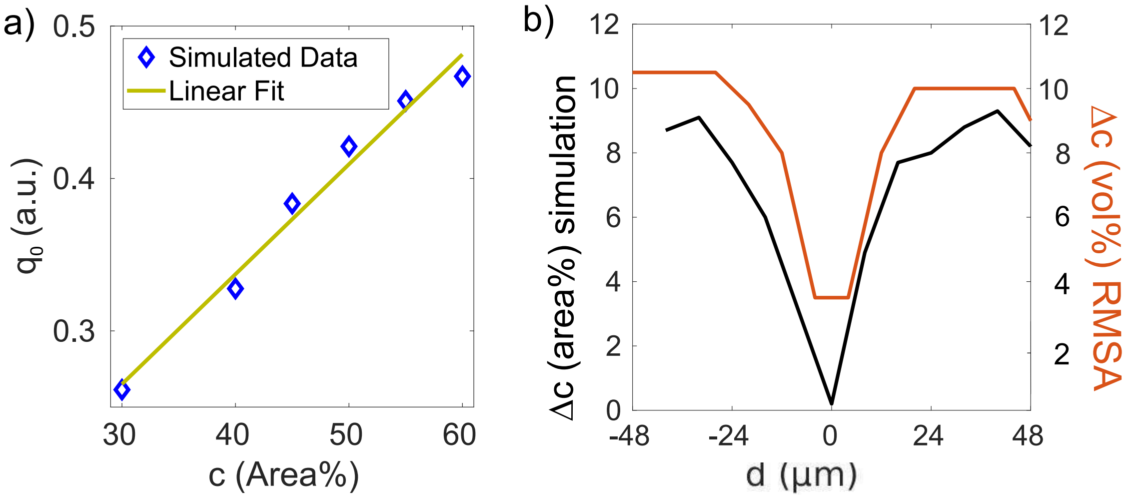

Figure 7.6: a) The position of q_0 for different area concentrations is shown for simulated 2-dimensional diffraction patterns. b) Concentration difference Δc across the jet approximated by q_0 positions. The slope of the linear fit in a) was extracted to convert measured q_0 variances in φ into concentration differences. Additionally the concentration difference calculated using the RMSA from Fig. 5.9 b is shown.

picture the prominent scattering from the anisotropic ordered region at $\approx 0.6r$ explains the appearance of a maximum ε over d as observed in the measured data.

For the simulation of microscopic particle arrangements, hard disks were first placed on rectangular lattice points as shown in Fig. 7.3 a. Afterwards, disorder was introduced using a Monte Carlo approach, moving the particles to new positions avoiding overlap with neighboring particles. The random particle distribution in Fig .7.3 b was obtained by allowing each particle to move randomly in horizontal and vertical directions. String-like arrangements (Fig. 7.3 c) were observed by limiting the degrees of freedom for movements in the vertical (or the horizontal) directions to 1/10 of the particle radius and reducing the number of steps. To obtain the diffraction patterns, a fast Fourier transformation (FFT) was applied to the aforementioned particle arrangements from boxes of 490000 particles. The resulting asymmetric diffraction patterns for string-like particle arrangements were then tilted and stacked on top of each other in order to rebuild a three-dimensional jet.

By arranging only specific angles of co-flowing strings to be used in the stacking, the angle-dependent contributions of the intensity in the diffraction patterns were modified to resemble the measured SAXS data for the Ludox sample. Examples are shown in Fig. 7.4, where a linecut from the simulated diffraction pattern is shown at $\varphi = 40^\circ$ in comparison with measured data from the Ludox sample. Differences in the overall decrease in q are due to the dimensionality difference in the simulation (discs, $I \propto q^{-2}$) and the experiment (spheres, $I \propto q^{-4}$). Moreover, the simulation did not take polydispersity or restrictions of the q-resolution into account, resulting in more pronounced intensity minima. The stacking contains five configurations of particles, orientated parallel to the d-axis and sloping down in 20° steps to being parallel with the h-axis, thus creating intensity maxima in the diffraction pattern between 0° and 90°. Experimentally the minimum in peak height of the intensity occurred in this range (cf. chapter 5.1).

Simulating a diffraction pattern that describes the measured data requires a particle formation of co-flowing strings not parallel to the h-axis (flow direction) but tilted outwards from the jet center towards the jet edge. Scattering patterns measured in the detector are superpositions of not only the basic string configuration but also projections of the string-like order due to the dimensionality of the jet (Fig. 7.5). The model used for the simulations does not rule out other possible particle arrangements, however, it is able to qualitatively describe the experimental findings for the Ludox sample at $1 \leq Pe \leq 9$.

As discussed in chapter 5.2 the anisotropic intensity distribution of the scattering patterns is accompanied by an anisotropy in q_0. The ovality of the diffraction pattern is considered to be connected to concentration differences between the stacked patterns and was further analyzed. For the Ludox sample the angular particle concentration distribution was extracted via RMSA and was shown in Fig. 5.9 b.

In the simulated diffraction patterns in Fig. 7.3 c the number of particles is a model parameter, so the two-dimensional effective volume fraction was calculated for each particle configuration before applying FFT. The positions q_0 of the structure factor peak in the calculated diffraction patterns show a linear behavior for the area concentrations depicted in Fig. 7.6 a. From the experimental results the ratio between the long and short axis of the oval-shaped diffraction patterns was extracted. With the slope from the linear fit in Fig. 7.6 a the two q_0 positions were transformed into a concentration distribution Δc over d (Fig. 7.6 b). Within an error of ± 2vol% the concentration distribution over the jet profile is comparable for both values from the RMSA analysis of the measured data (three-dimensional) to the simulation of string-like order (two-dimensional), which verifies the applicability of the simulation method for jetting systems.

Chapter 8

Summary& Outlook

Rheological studies were performed on colloidal silica particles in water. The fluid passed through 75-150 micrometer thin tubes before being dispensed as a liquid micro-jet. Particle arrangements in the jet were probed with X-ray scattering techniques across the jet profile and along the flow direction.

With these so-called Rayleigh nozzles shear rates between $0.9 \cdot 10^5\,\mathrm{s}^{-1}$ to $5.6 \cdot 10^5\,\mathrm{s}^{-1}$ were applied on the colloidal suspension. From close to the nozzle tip ($100\,\mu$m) up to a distance of 3 mm all measurements were performed in the laminar flow regime. With particle radii from 15 nm, 43 nm, 63 nm to 76.5 nm Péclet numbers of 1 to 1162 were achieved, a regime where hydrodynamic forces and shear forces dominated over Brownian motion.

Based on the diffraction patterns collected by scanning through the liquid jet, regions of isotropic and anisotropic particle arrangements were determined. X-ray cross-correlation analysis quantified the degree of anisotropy in the intensity distribution over the azimuthal angle for each recorded pattern. The distribution of the anisotropy parameter ε was comparable for the left- and right-hand side of the jet. In the center of the jet no asymmetric scattering patterns and therefore no anisotropic ordering was observed. The location of the maximum asymmetry ε is strongly dependent on the jet diameter, jet geometry and particle size, ranging from $0.4r$ to $0.9r$. Small particles and large tubes developed structured regions closer to the jet edge. With increasing distance from the nozzle tip the maximum ε moved towards the jet center, which was a slower process for larger particle sizes and thus higher *Pe* numbers.

A second parameter $\mathrm{var}(q_0)$ for describing the shape asymmetry in the diffraction patterns showed for low *Pe* a remarkable similarity with the behavior of ε. The shift of q_0 in φ led to an oval shape of the scattering pattern. Both ε and $\mathrm{var}(q_0)$ represent different aspects in the sample system. While the asymmetry of the scattering pattern relates a direction-dependent intensity to a φ-dependent particle ordering, the ovality of the diffraction pattern, quantified by the direction-dependent variance in q_0, relates to a change in next-neighbor distance. The coexistence of both phenomena is found in the studied colloidal dispersion independent of other probed parameters such as flow rate or nozzle geometry.

The evolution of ordering in the jet was investigated over time. A characteristic decay time τ_{ε} described the exponential decay of ε as a function of t and was investigated for different flow rates. Correlations were found between τ_{ε} and the Péclet number, independent on nozzle sizes or geometries. The normalized decay time τ_{ε} shows a weak power law behavior Pe^n with $n = 0.14 \pm 0.07$. Thus, characteristic times τ were found to be dependent on the parameters shear rate, viscosity and hydrodynamic particle radius.

Furthermore, the shear-induced ordering of charge-stabilized particles was found to be sensitive to the tuning of electro-static forces. The degree of maximum ordering decreased when salt was added to the colloidal silica suspension, as the salt screened the charge-stabilized particles and creates a more hard-sphere like interaction potential. An increase in the charge per particle or the ionic strength of the suspension amplified the decrease in the characteristic decay times τ_{ε} for all studied systems.

The non-isotropic microscopic particle arrangement was compared to simulations. Diffraction patterns obtained by FFT from co-flowing string-like arrangements allowed to model the experimental findings. Moreover, the angular variation of the structure factor peak revealed a preferred orientation of the co-flowing strings tilted away from the jet center. For the q-position of the structure factor peak the angular dependence was modeled with varying particle concentrations. From the ratio between the long-and short-axis of the oval-shape diffraction patterns the direction-dependent effective volume fraction in the experimental data was approximated, which was in good agreement with the localized volume fraction from the RMSA data analysis.

The results indicate that jet-based sample delivery relies on well understood flow mechanics as well as the impact of shear rate and tube size, which are accessible with this spatial and temporal approach to liquid jet-based rheology. The applicability of liquid jets as rheometers was shown, where jet systems as capillary rheometer are capable of shear rates a magnitude higher than classical rotational rheometers.

Further investigations studying rheology of jets are needed for smaller jet sizes down to a few micrometers. The sample chamber and the attached recycling system for the liquid introduced in this work are a working basis for future rheology experiments. At synchrotron radiation facilities and FELs a sample delivery via liquid micro-jet is often used for radiation sensitive macromolecules. However, such biological systems are usually only available in small quantities, while a laminar flow and MHz operation at the FEL require a minimum jet velocity. Therefore μm-sized tubes, which exert high shear rates onto the sample systems, are utilized. Rheological studies could be extended to non-spherical particles, liquid crystals and systems with different interaction potentials. Moreover, the mixing of solvents in jets could be examined in future.

Appendix

Fig. A1 shows diffraction patterns from sample L across the jet profile. In addition to the scattering patterns shown for the Ludox sample in Fig. 5.2., this figure attests to the mirror-inverted symmetry between patterns taken at $d < 0$ and $d > 0$. The development of anisotropic patterns as well as the distinct partition of the patterns could be observed for all d.

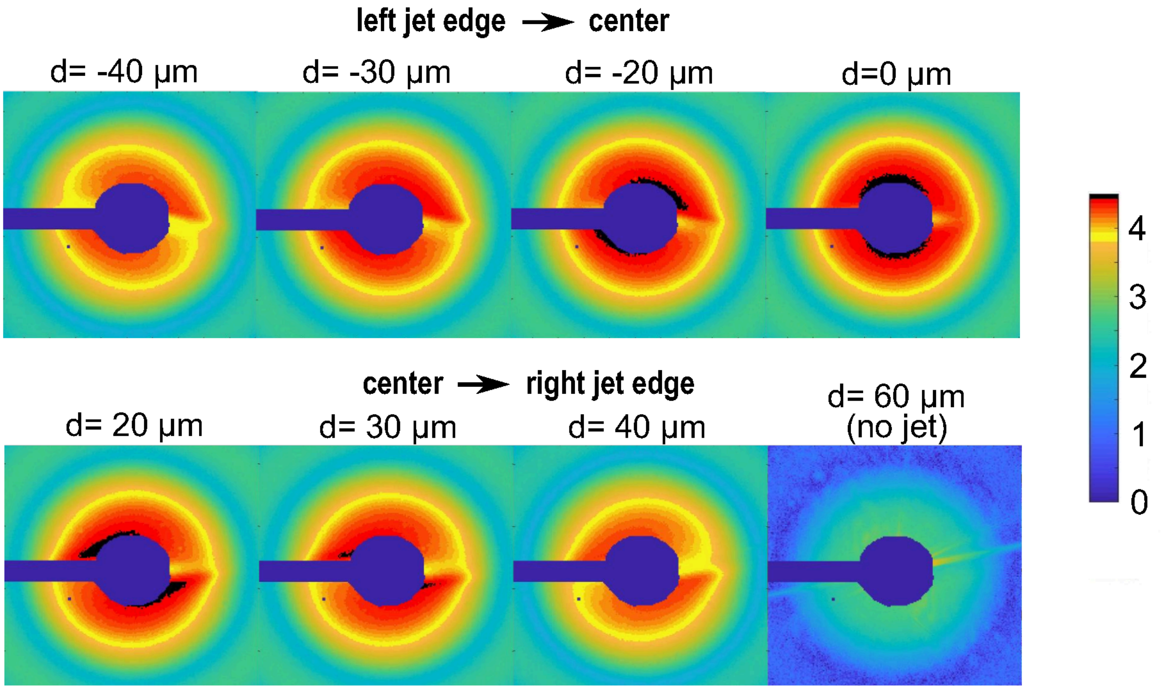

Figure A1: Scattering patterns at different positions in the horizontal jet profile for the sample L. The patterns were taken at $h = 100\,\mu$m for a jet of $75\,\mu$m diameter and show an asymmetric intensity distribution for $d < 0$ and $d > 0$.

Complementary to the SAXS curves shown in Fig. 5.4 for sample L and Ludox, Fig. A2 depicts the behavior of $I(q,\varphi)$ and $S(q,\varphi)$ for sample S and M. For the smaller sample S the ring of maximum intensity shifts to larger q. For sample S the maximum $S(q,\varphi)$ lies at $q = 0.5$-$0.7\,\mathrm{nm}^{-1}$ and for sample M at $q = 0.4$-$0.6\,\mathrm{nm}^{-1}$.

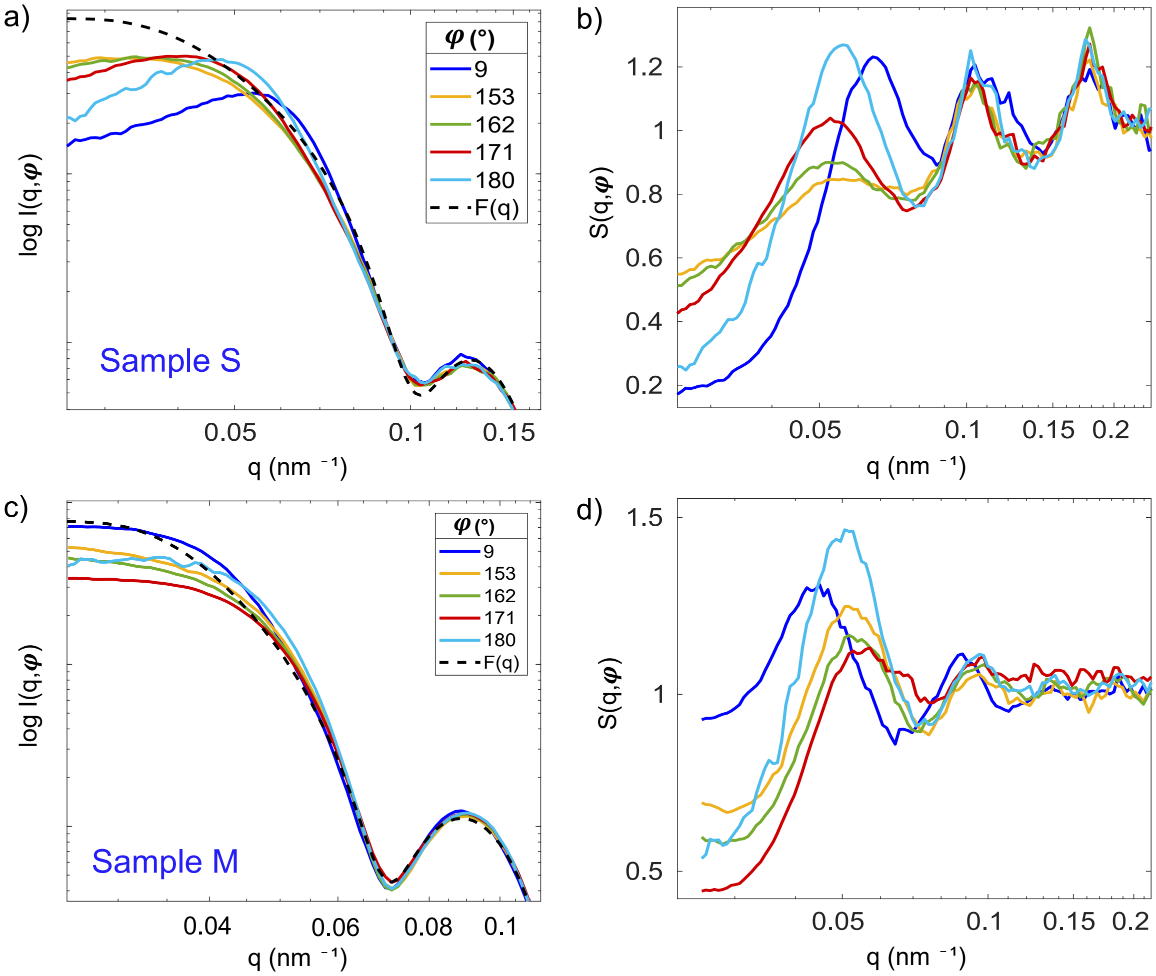

Figure A2: a) Intensity $I(q,\varphi)$ of sample S integrated over circular sectors of 9° and b) structure factors calculated from the intensities. The measurements were done at $d = 24\,\mu\text{m}$ with the $75\,\mu\text{m}$ round nozzle, flow rate $Q = 800\,\mu\text{l/min}$ at $h = 100\,\text{mm}$ nozzle distance. c) and d) show the same measurements for sample M.

For the charge-stabilized sample L under the influence of salt the asymmetry quantifying parameter ε over d was shown in Fig. 6.3 for $\dot{\gamma} = 5.6 \cdot 10^5\,\text{s}^{-1}$. In addition, Fig. A3 displays the same system at a lower shear rate of $4.8 \cdot 10^5\,\text{s}^{-1}$ with slightly smaller ε, albeit a comparable trend over d and h.

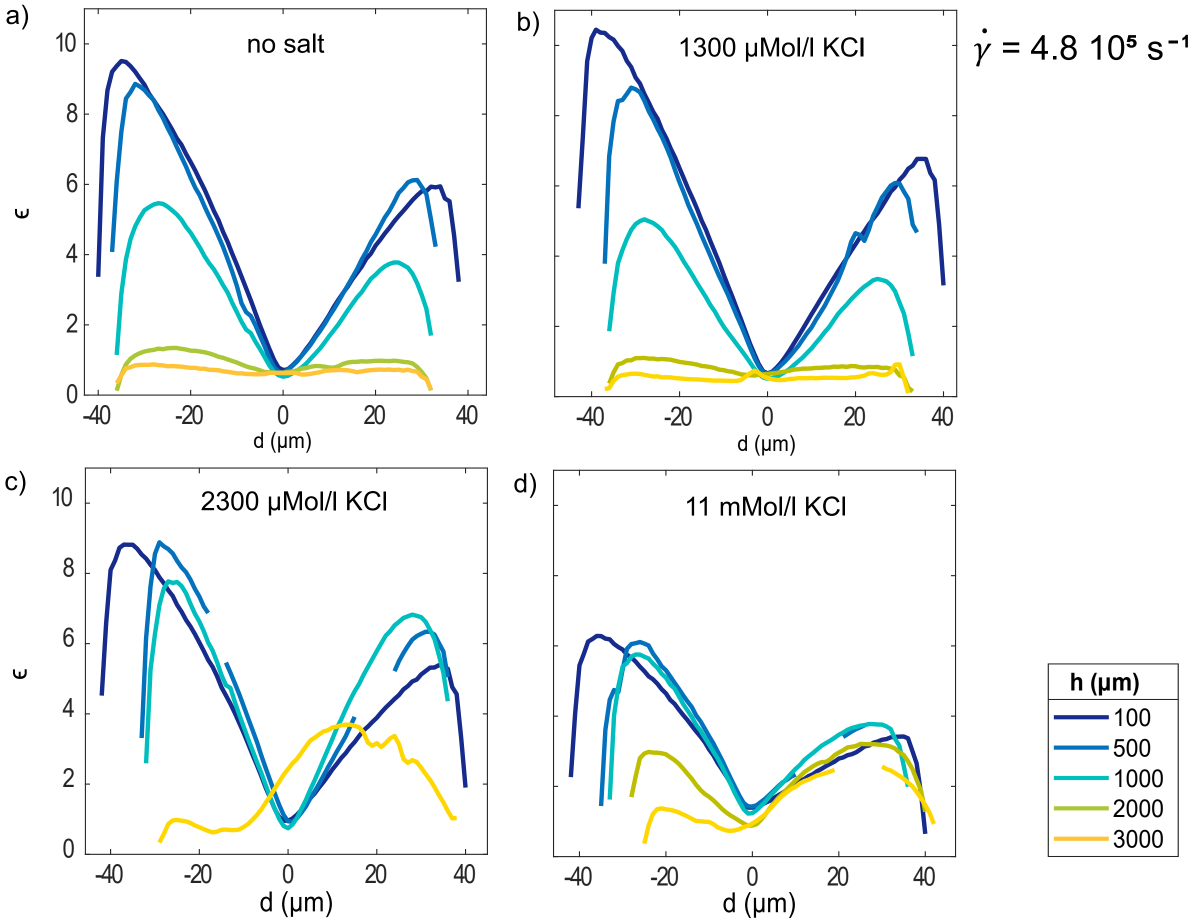

Figure A3: Plotted is the asymmetry quantifying parameter ε over the nozzle profile d for sample L with a) no salt, b) 1300 μMol/l, c) 2300 μMol/l and d) 11 mMol/ KCl. Measurements were performed with the 75 μm round nozzle at $\dot{\gamma} = 4.8 \cdot 10^5\,\mathrm{s}^{-1}$.

Bibliography

[1] Max O. Wiedorn et al. “Rapid sample delivery for megahertz serial crystallography at X-ray FELs”. In: *IUCrJ* 5 (2018), 574–584.

[2] J. Schulz et al. “A versatile liquid-jet setup for the European XFEL”. In: *J. Synchrotron Radiat.* 26 (2019), 339–345.

[3] L. Shang, C. Yao, and Z. Yuanjin. “Emerging droplet microfluidics”. In: *Chem. Rev.* 117 (2017), 7964–8040.

[4] H.N. Chapman. “Femtosecond X-ray protein nanocrystallography”. In: *Nature* 470 (2011), 73.

[5] A. Baharati, S.D. Hudson, and K.M. Weigandt. “Poiseuille and Extensional FlowSAS for Developing Structure-Rheology Relationships in Soft Matter Systems”. In: *Curr. Opin. Colloid Interface Sci.* 42 (2019), 137–146.

[6] Jonas A. Sellberg et al. “Ultrafast X-ray probing of water structure below the homogeneous ice nucleation temperature”. In: *Nature* 510 (2014), 381–384.

[7] C. Goy et al. “Shrinking of rapidly evaporating water microdroplets reveals their extreme supercooling”. In: *Phys. Rev. Lett.* 120 (2018), 015501.

[8] R.E. Grisenti et al. “Evaporating laminar microjets for studies of rapidly evolving structural transformations in supercooled liquids”. In: *Adv. Phys.-X* 3 (2018), 1418183.

[9] C. Kupitz et al. “Structural enzymology using X-ray free electron lasers”. In: *Struct. Dynam.* 4 (2017), 044003.

[10] C.A. Stan et al. “Liquid explosions induced by X-ray laser pulses”. In: *Nat. Phys.* 12 (2016), 966.

[11] L. Redecke et al. “Natively inhibited Trypanosoma brucei cathepsin B structure determined by using an X-ray laser”. In: *Science* 339 (2013), 227–230.

[12] P. Panine et al. “Structure and rheology during shear-induced crystallization of a latex suspension”. In: *Phys. Rev. E* 66 (2002), 022401.

[13] Dmitry Denisov et al. “Resolving structural modifications of colloidal glasses by combining x-ray scattering and rheology”. In: *Sci. Rep.* 3 (2013), 1631.

[14] Rizwan Zahoor, Saša Bajt, and Božidar Šarler. “Numerical investigation on influence of focusing gas type on liquid micro-jet characteristics”. In: *Int. J. Hydromechatronics* 1 (2018), 222–237.

[15] S. Marenne et al. “Unsteady shear flows of colloidal hard-sphere suspensions by dynamic simulation”. In: *J. Rheol.* 61 (2017), 477–501.

[16] B.J. Ackerson. “Shear induced order and shear processing of model hard sphere suspensions”. In: *J. Rheol.* 34 (1990), 553–590.

[17] Bernd Winter and Manfred Faubel. “Photoemission from liquid aqueous solutions”. In: *Chem. Rev.* 106 (2006), 1176–1211.

[18] Jake D. Koralek et al. “Generation and characterization of ultrathin free-flowing liquid sheets”. In: *Nat. Commun.* 9 (2018), 1–8.

[19] F.R.S. Lord Rayleigh. “On the Instability of Jets”. In: *Proc. London Math. Soc.* 1 (1878), 4–13.

[20] Alfonso M. Gañán-Calvo. “Generation of steady liquid microthreads and micron-sized monodisperse sprays in gas streams”. In: *Phys. Rev. Lett.* 80 (1998), 285.

[21] P.D. DePonte et al. “Generation of Steady Liquid Microthreads and Micron-Sized Monodisperse Sprays in Gas Streams”. In: *Phys. Rev. Lett* 80 (2008), 285–288.

[22] Norman J. Wagner and John F. Brady. “Shear thickening in colloidal dispersions”. In: *Phys. Today* 62 (2009), 27–32.

[23] Xiang Cheng et al. “Imaging the microscopic structure of shear thinning and thickening colloidal suspensions”. In: *Science* 333 (2011), 1276–1279.

[24] E. Brown and H.M. Jaeger. “Shear thickening in concentrated suspensions: phenomenology, mechanisms and relations to jamming”. In: *Rep. Prog. Phys.* 77 (2014), 046602.

[25] Robert Hooke. *Lectures de potentia restitutiva, or of spring explaining the power of springing bodies*. 6. John Martyn, 2016.

[26] I. Newton. *The Mathematical Principles of Natural Philosophy*. B. Motte, 1729.

[27] M. Reiner. “The deborah number”. In: *Phys. Today* 17 (1964), 359–367.

[28] P.S.R. Krishna Prasad et al. “Studies on rheology of ceramic inks and spread of ink droplets for direct ceramic ink jet printing”. In: *J. Mater. Process.* 176 (2006), 222–229.

[29] S.D. Hoath et al. “Links between ink rheology, drop-on-demand jet formation, and printability”. In: *J. Imaging Sci. Technol.* 53 (2009), 041208.

[30] Sathish Pandiyan, Ahmad El-Kharouf, and Robert Steinberger-Wilckens. “Formulation of Spinel based Inkjet Inks for Protective Layer Coatings in SOFC Interconnects”. In: *J. Colloid Interface Sci.* 579 (2020), 82–95.

[31] Shilpa Kantaria, Gareth D. Rees, and M. Jayne Lawrence. “Gelatin-stabilised microemulsion-based organogels: rheology and application in iontophoretic transdermal drug delivery”. In: *J. Control. Release* 60 (1999), 355–365.

[32] Atul Dhiman and Pramod K. Prabhakar. “Micronization in food processing: A comprehensive review of mechanistic approach, physicochemical, functional properties and self-stability of micronized food materials”. In: *J. Food Eng.* 292 (2020), 110248.

[33] Tetsuya Yamamoto, Yuichi Masubuchi, and Masao Doi. “Fracture strain of composite with nonuniformly distributed reinforcing fibers”. In: *J. Rheol.* 64 (2020), 933–939.

[34] Domingo R. Flores-Hernandez et al. “Tailoring the Diameters of Electro-Mechanically Spun Fibers by Controlling Their Deborah Numbers”. In: *Polymers* 12 (2020), 1358.

[35] Wei Chen et al. “Molecular and thermodynamics descriptions of flow-induced crystallization in semi-crystalline polymers”. In: *J. Appl. Phys.* 127 (2020), 241101.

[36] R.B. Bird. “Transport phenomena”. In: *Appl. Mech. Rev.* 55 (2002), R1–R4.

[37] Singiresu S. Rao. *The finite element method in engineering*. Butterworth-Heinemann, 2017.

[38] James C.Y. Guo. *Theoretical Fluid Mechanics Laminar Flow Velocity Profile*. (accessed: 17.11.2020).

[39] Zoltán Csuka and Róber Olšiak. “The profile of shear stress in the liquid at turbulent flow”. In: *AIP Conference Proceedings*. Vol. 1768. AIP Publishing LLC. 2016, 020032.

[40] F.N. Cogswell. “Rheology of polymer melts under tension”. In: *Plastics & Polymers* 36 (1968), 109.

[41] G.H. McKinley et al. “Extensional rheometry of polymeric fluids and the uniaxial elongation of viscoelastic filaments”. In: *Plenaery Paper, 15th International Polymer Processing Society, Netherlands*. 1999.

[42] J. Meissner and J. Hostettler. “A new elongational rheometer for polymer melts and other highly viscoelastic liquids”. In: *Rheol. Acta* 33 (1994), 1–21.

[43] Massachusetts Institute of Technology. *Extensional Rheology Experiment (ERE)*. URL: `http://web.mit.edu/nnf/research/ere/ere.html`. (accessed: 10.11.2020).

[44] Gareth H. McKinley and Tamarapu Sridhar. “Filament-stretching rheometry of complex fluids”. In: *Annu. Rev. Fluid Mech.* 34 (2002), 375–415.

[45] Kirk A. Logsdon. *Extensional Rheology Experiment Developed to Investigate the Rheology of Dilute Polymer Solutions in Microgravity*. URL: `https://ntrs.nasa.gov/archive/nasa/casi.ntrs.nasa.gov/20050199442.pdf`. (accessed: 09.07.2020).

[46] Michael Baumgärtel and Norbert Willenbacher. “The relaxation of concentrated polymer solutions”. In: *Rheol. Acta* 35 (1996), 168–185.

[47] Malvern Panalytical. *Viscosity flow curve. Part 2.* URL: `https://www.materials-talks.com/blog/2017/06/08/viscosity-flow-curve-part-2/`. (accessed: 17.11.2020).

[48] Ron Hugo. *Introductory Fluid Mechanics L2 p4: Non-Newtonian Fluids*. URL: `https://www.youtube.com/watch?v=5YEaXa3X3dk`. (accessed: 22.12.2020).

[49] H. Margenau. “Van der Waals forces”. In: *Rev. Mod. Phys.* 11 (1939), 1.

[50] Hugo C. Hamaker. “The London-van der Waals attraction between spherical particles”. In: *Physica* 4 (1937), 1058–1072.

[51] Gary L. Hunter and Eric R. Weeks. “The physics of the colloidal glass transition”. In: *Rep. Prog. Phys.* 75 (2012), 066501.

[52] Hideki Yukawa. “On the interaction of elementary particles. I”. In: *Proc. Phys. Math. Soc. Jpn. 3rd Series* 17 (1935), 48–57.

[53] Roland Kjellander and Rosa Ramirez. “Screened Coulomb potential and the renormalized charges of ions and molecules in electrolyte solutions”. In: *J. Phys. Condens. Matter* 17 (2005), S3409.

[54] Boris Derjaguin and Lev Landau. “Theory of the stability of strongly charged lyophobic sols and of the adhesion of strongly charged particles in solutions of electrolytes”. In: *Prog. Surf. Sci.* 43 (1993), 30–59.

[55] University Bayreuth. *Kolloidstabilität auf Grund elektrostatischer Wechselwirkungen*. URL: `http://daten.didaktikchemie.uni-bayreuth.de/umat/kolloide_stabilitaet/kolloidstabiliaet.htm`. (accessed: 10.11.2020).

[56] Richard L. Hoffman. “Explanations for the cause of shear thickening in concentrated colloidal suspensions”. In: *J. Rheol.* 42 (1998), 111–123.

[57] William Bailey Russel et al. *Colloidal dispersions*. Cambridge university press, 1991.

[58] Roger Temam. *Navier-Stokes equations: theory and numerical analysis*. American Mathematical Soc., 2001.

[59] Felix Lehmkühler et al. “Microsecond Structural Rheology”. In: *J. Phys. Chem. Lett.* 8 (2017), 3581–3585.

[60] John R. Melrose and Robin C. Ball. “Contact networks in continuously shear thickening colloids”. In: *J. Rheol.* 48 (2004), 961–978.

[61] Ammar Yahia. “Shear-thickening behavior of high-performance cement grouts-Influencing mix-design parameters”. In: *Cement Concrete Res.* 41 (2011), 230–235.

[62] R.G. Egres Jr. et al. “Liquid armor: protective fabrics utilising shear thickening fluids”. In: *Proceedings of the 4th International Conference of Safety and Protective Fabrics*. Vol. 26. 2004.

[63] Selim Gürgen, Melih Cemal Kuşhan, and Weihua Li. “Shear thickening fluids in protective applications: A review”. In: *Prog. Polym. Sci.* 75 (2017), 48–72.

[64] University of Salerno. *Capillary Rheometer*. URL: `http://www.polymertechnology.it/bacheca/fluid/Esercitazione081105b.pdf`. (accessed: 17.11.2020).

[65] Eugene Cook Bingham. *An investigation of the laws of plastic flow*. US Government Printing Office, 1917.

[66] E. Buckingham. “On plastic flow through capillary tubes”. In: *Proc. Am. Soc. Testing Materials*. 1921, 1154–1156.

[67] Boyun Guo and Gefei Liu. *Applied drilling circulation systems: hydraulics, calculations and models*. Gulf Professional Publishing, 2011.

[68] Norbert Willenbacher. “Unusual thixotropic properties of aqueous dispersions of Laponite RD”. In: *J. Colloid Interface Sci.* 182 (1996), 501–510.

[69] H. Ito and N. Kumagai. “A creep experiment on a large granite beam started in 1980”. In: *Int. J. Rock Mech. Min. Sci. Geomech. Abstr.* 31 (1994), 359–367.

[70] Sung-Piau Lin. *Breakup of liquid sheets and jets*. Cambridge University Press, 2003.

[71] F.R.S. Lord Rayleigh. “Some Applications of Photography 1”. In: *Nature* 44 (1891), 249–254.

[72] Marie Luise Grünbein, Robert L. Shoeman, and R. Bruce Doak. “Velocimetry of fast microscopic liquid jets by nanosecond dual-pulse laser illumination for megahertz X-ray free-electron lasers”. In: *Opt. Express* 26.6 (2018), 7190–7203.

[73] Sébastien Boutet et al. “High-resolution protein structure determination by serial femtosecond crystallography”. In: *Science* 337 (2012), 362–364.

[74] Austin Echelmeier, Mukul Sonker, and Alexandra Ros. “Microfluidic sample delivery for serial crystallography using XFELs”. In: *Anal. Bioanal. Chem.* 411 (2019), 6535–6547.

[75] Uwe Weierstall, J.C.H. Spence, and R.B. Doak. “Injector for scattering measurements on fully solvated biospecies”. In: *Rev. Sci. Instrum.* 83 (2012), 035108.

[76] Claudiu A. Stan et al. “Liquid explosions induced by X-ray laser pulses”. In: *Nat. Phys.* 12 (2016), 966–971.

[77] Jens Eggers and Emmanuel Villermaux. “Physics of liquid jets”. In: *Rep. Prog. Phys.* 71 (2008), 036601.

[78] Rupert Stevenson Bradley. “LXXIX. The cohesive force between solid surfaces and the surface energy of solids”. In: *Lond. Edinb. Dubl. Phil. Mag.* 13 (1932), 853–862.

[79] Lei Xu, Loreto Barcos, and Sidney R. Nagel. “Splashing of liquids: Interplay of surface roughness with surrounding gas”. In: *Phys. Rev. E* 76 (2007), 066311.

[80] Wilhelm Conrad Röntgen. “On a new kind of rays”. In: *Science* 3 (1896), 227–231.

[81] M. Altarelli. “The European X-ray free-electron laser facility in Hamburg”. In: *Nuclear Instruments and Methods in Physics Research Section B: Beam Interactions with Materials and Atoms* 269 (2011), 2845–2849.

[82] Andrew T. Young. “Rayleigh scattering”. In: *Appl. Opt.* 20 (1981), 533–535.

[83] J. Als-Nielson and D. McMorrow. *Elements of Modern X-ray Analysis (Hoboken, NJ.* Wiley, 2001.

[84] B. Tieke. *Macromolekulare Chemie; 2 Auflage ed.* Wiley-VCH: Weinheim, 2005.

[85] A.P. Philipse and A. Vrij. “Determination of static and dynamic interactions between monodisperse, charged silica spheres in an optically matching, organic solvent”. In: *J. Chem. Phys.* 88 (1988), 6459–6470.

[86] R.J. Baxter. “Ornstein-Zernike relation for a disordered fluid”. In: *Aust. J. Phys.* 21 (1968), 563–570.

[87] Neil W. Ashcroft and Ji Lekner. “Structure and resistivity of liquid metals”. In: *Phys. Rev.* 145 (1966), 83.

[88] John B. Hayter and Jeff Penfold. “An analytic structure factor for macroion solutions”. In: *Mol. Phys.* 42 (1981), 109–118.

[89] Jean-Pierre Hansen and John B. Hayter. “A rescaled MSA structure factor for dilute charged colloidal dispersions”. In: *Mol. Phys.* 46 (1982), 651–656.

[90] Fabian Westermeier. “Structure and Dynamics of highly charged colloidal suspensions”. PhD thesis. Staats-und Universitätsbibliothek Hamburg Carl von Ossietzky, 2010.

[91] Peter Wochner et al. “X-ray cross correlation analysis uncovers hidden local symmetries in disordered matter”. In: *P. Natl. Acad. Sci. USA* 106 (2009), 11511–11514.

[92] Irina Lokteva et al. “Coexistence of hcp and bct Phases during In Situ Superlattice Assembly from Faceted Colloidal Nanocrystals”. In: *J. Phys. Chem. Lett.* 10 (2019), 6331–6338.

[93] Irina Lokteva et al. “Monitoring Nanocrystal Self-Assembly in Real Time Using In Situ Small-Angle X-Ray Scattering”. In: *Small* 15 (2019), 1900438.

[94] Felix Lehmkühler, Gerhard Grübel, and Christian Gutt. “Detecting orientational order in model systems by X-ray cross-correlation methods”. In: *J. Appl. Cryst.* 47 (2014), 1315–1323.

[95] C.G. De Kruif et al. “Small-angle neutron scattering of sheared concentrated dispersions: Microstructure along principal flow axes”. In: *Phys. Fluids A - Fluid* 2 (1990), 1545–1556.

[96] Bruce J. Ackerson. “Shear induced order in equilibrium colloidal liquids”. In: *Physica A* 174 (1991), 15–30.

[97] A.T.J.M. Woutersen, R.P. May, and C.G. De Kruif. “The shear-distorted microstructure of adhesive hard sphere dispersions: A small-angle neutron scattering study”. In: *J. Rheol.* 37 (1993), 71–88.

[98] Aaron P.R. Eberle et al. “Shear viscosity and structural scalings in model adhesive hard-sphere gels”. In: *Phys. Rev. E* 89 (2014), 050302.

[99] François Boulogne et al. “Structural anisotropy of directionally dried colloids”. In: *Europhys. Lett.* 105 (2014), 38005.

[100] Photon Science DESY. *Rheology setup*. URL: `https://photon-science.desy.de/facilities/petra_iii/beamlines/p10_coherence_applications/infrastructure/eh1_soft_matter_cdi_xpcs_6_circle_diffractometer_rheometer_setup/rheology_setup/index_eng.html`. (accessed: 24.11.2020).

[101] Theyencheri Narayanan et al. “A microvolume shear cell for combined rheology and x-ray scattering experiments”. In: *Rev. Sci. Instrum.* 91 (2020), 085102.

[102] Annemarie Nack et al. “Hindered nematic alignment of hematite spindles in poly (N-isopropylacrylamide) hydrogels: a small-angle X-ray scattering and rheology study”. In: *J. Appl. Crystallogr.* 51 (2018), 87–96.

[103] Robert L. Leheny et al. “Rheo-XPCS”. In: *Curr. Opin. Colloid In.* 20 (2015), 261–271.

[104] V. Markmann et al. “Shear-induced ordering in liquid microjets seen by x-ray cross correlation analysis”. In: *Structural Dynamics* 7 (2020), 054901.

[105] Enrico F. Semeraro, Johannes Möller, and Theyencheri Narayanan. “Multiple-scattering effects in SAXS and XPCS measurements in the ultra-small-angle region”. In: *J. Appl. Crystallogr.* 51 (2018), 706–713.

[106] Werner Stöber, Arthur Fink, and Ernst Bohn. “Controlled growth of monodisperse silica spheres in the micron size range”. In: *J. Colloid Interface Sci.* 26 (1968), 62–69.

[107] Photon Science DESY. *P10 Coherence Applications Beamline*. URL: `https://photon-science.desy.de/facilities/petra_iii/beamlines/p10_coherence_applications/index_eng.html`. (accessed: 16.11.2020).

[108] A.V. Zozulya et al. “Microfocusing transfocator for 1D and 2D compound refractive lenses”. In: *Opt. Express* 20 (2012), 18967–18976.

[109] DECTRIS detecting the future. *EIGER2 X 4M*. URL: `https://www.dectris.com/products/eiger2/eiger2-x-xe-for-synchrotron/eiger2-x-4m/`. (accessed: 16.11.2020).

[110] Ingo Steinke et al. “A liquid jet setup for x-ray scattering experiments on complex liquids at free-electron laser sources”. In: *Rev. Sci. Instrum.* 87 (2016), 063905.

[111] cetoni GmbH. *QmixElements*. URL: `https://www.cetoni.de/produkte/qmixelements/`. (accessed: 17.11.2020).

[112] Ronald Darby, Ron Darby, and Raj P. Chhabra. *Chemical engineering fluid mechanics, revised and expanded*. CRC Press, 2017.

[113] Y. Son. “Determination of shear viscosity an shear rate from pressure drop and flow rate relationship in a rectangular channel”. In: *Polymer* 48 (2006), 632–637.

[114] John F. Brady and Jeffrey F. Morris. “Microstructure of strongly sheared suspensions and its impact on rheology and diffusion”. In: *J. Fluid Mech.* 348 (1997), 103–139.

[115] C.G. de Kruif et al. “Hard sphere colloidal dispersions: Viscosity as a function of shear rate and volume fraction”. In: *J. Chem. Phys.* 83 (1985), 4717–4725.

[116] Manuel E Sastre de Vicente. “The concept of ionic strength eighty years after its introduction in chemistry”. In: *J. Chem. Educ.* 81 (2004), 750.

[117] Sandeep D. Kulkarni and Jeffrey F. Morris. “Ordering transition and structural evolution under shear in Brownian suspensions”. In: *J. Rheol.* 53 (2009), 417–439.

[118] J.R. Goldstein. “Measurement of Laminar Flow Development in a Square Duct Using a Laser-Doppler Flowmeter”. In: *J. Appl. Mech.* 34 (1967), 813–818.

[119] E.M. Sparrow, S.H. Lin, and Lundgren T.S. “Flow development in the hydrodynamic entrance region of tubes and ducts”. In: *Phys. Fluids* 7 (1964), 338–347.

[120] A.M. Gañán-Calvo et al. “A novel pneumatic technique to generate steady capillary microjets”. In: *J. Aerosol Sci.* 30 (1999), 117–125.

Own publications

Publications directly relating to this thesis

1. V. Markmann, M. Dartsch, J. Valerio, L. Frenzel, I. Lokteva, M. Walther, F. Westermeier, G. Grübel, F. Lehmkühler, ”Shear-induced ordering in liquid microjets seen by x-ray cross correlation analysis”, *Struct. Dynam.* (2020) 7, 054901.

Miscellaneous

1. W. Jo, F. Westermeier, R. Rysov, O. Leupold, F. Schulz, S. Tober, V. Markmann, M. Sprung, A. Ricci, T. Laurus, A. Aschkan, A. Klyuev, U. Trunk, H. Graasfma, G. Grübel, W. Roseker, “Nanosecond X-ray Photon Correlation Spectroscopy using pulse time structure of a storage ring source”, *IUCrJ* (2021) 8, 124-130.

2. F. Lehmkühler, F. Dallari, A. Jain, M. Sikorski, J. Möller, L. Frenzel, I. Lokteva, G. Mills, M. Walther, H. Sinn, F. Schulz, M. Dartsch, V. Markmann, R. Bean, Y. Kim, P. Vagovic, A. Madsen, A.P. Mancuso, G. Grübel ”Emergence of anomalous dynamics in soft matter probed at the European XFEL” *PNAS* (2020) 117, 24110-24116.

3. F. Schulz, F. Westermeier, F. Dallari, V. Markmann, H. Lange, G. Grübel, F. Lehmkühler, ”Plasmonic Supercrystals with a layered structure studied by a combined TEM-SAXS-XCCA approach” *Adv. Mater. Interfaces* (2020) 7, 2000919.

4. M.A. Schroer, F. Lehmkühler, V. Markmann, L. Frenzel, J. Möller, H. Lange, G. Grübel, F. Schulz, ”Supercrystal Formation of Gold Nanorods by High Pressure Stimulation” *J. Phys. Chem. C* (2019) 123, 29994-30000.

5. F. Lehmkühler, M.A. Schroer, V. Markmann, L. Frenzel, J. Möller, H. Lange, G. Grübel, F. Schulz, ”Kinetics of pressure-induced nanocrystal superlattice formation”, *Phys. Chem. Chem. Phys.* (2019) 21, 21349-21354.

Acknowledgements

I am very happy and thankful to Prof. Dr. Gerhard Grübel for the opportunity to study soft matter physics and to write my PhD thesis here at DESY with the FS-CXS group. I have been welcomed with open arms during my master thesis and was lucky to further benefit from the enormous accumulated knowledge and the groups freely given teachings as a PhD student. All of this has been made possible by the financial support of DESY. I want to thank everyone who supported me for the last 3 years in learning about scientific work procedures, but also for providing a great interpersonal environment. The whole coherence X-ray scattering group and especially my office mates has been very helpful and open to all my questions.

Special thanks go to my supervisor Felix Lehmkühler, who has always made time for questions and advises, had new ideas or a spare hand at experiments. Likewise I am thankful to Michael Dartsch, who provided me with advice about simulation work and always knew how to solve a coding problem. I would also like to express my gratitude to Michael Walther, who constructed and designed the sample environment, as well as Irina Lokteva for introducing chemical methods to me and providing samples for experiments.

For the experimental support at beamline P10 of PETRA III I would like to thank Dr. Michael Sprung, Dr. Fabian Westermeier and everyone who offered up their days and nights to keep the operation running. Furthermore I like to say thanks to my family, who supported me all this time. Who helped me to revise by listened to me talking about physics for hours. Who trusted me with calculations on their journeyman's piece and taught me to pick up the screwdriver and use my own two hands if I want something done. Thank you all!

Hiermit erkläre ich an Eides statt, dass ich die vorliegende Dissertationsschrift selbst verfasst und keine anderen als die angegebenen Quellen und Hilfsmittel benutzt habe.

Die eingereichte schriftliche Fassung entspricht der auf dem elektronischen Speichermedium. Die Dissertation wurde in der vorgelegten oder einer ähnlichen Form nicht schon einmal in einem früheren Promotionsverfahren angenommen oder als ungenügend beurteilt.

Ort, Datum

Unterschrift